Detection of Lithium-ion Battery Failure and Thermal Runaway

by

Ting Cai

A dissertation submitted in partial fulfillment
of the requirements for the degree of
Doctor of Philosophy
(Mechanical Engineering)
in The University of Michigan
2021

Doctoral Committee:

Associate Research Scientist Jason Siegel, Co-Chair
Professor Anna Stefanopoulou, Co-Chair
Professor Ian Hiskens
Professor Donald Siegel

Ting Cai

tingcai@umich.edu

ORCID iD: 0000-0001-8343-9032

ACKNOWLEDGEMENTS

I would like to start by expressing my gratitude towards my Ph.D. advisors, Professor Anna Stefanopoulou, and Dr. Jason Siegel. I started this journey with the battery control class, ME 565, where I met my future Ph.D. advisors and started to grow my passion for batteries and electric vehicles. I'm lucky to be a member of the Battery Control Group and work on various projects of battery safety research. I want to thank Professor Anna Stefanopoulou and Dr. Jason Siegel for giving me the wonderful opportunity to work on a Ph.D. program on state-of-the-art battery research. Their dedicated support and guidance during these years have helped me to make research progress and achieve self-growth.

Thanks to the committee members, Prof. Donald Siegel, and Prof. Ian Hiskens, for taking the time and interest in evaluating my work and providing comments and feedback.

Thanks to all the members of the Battery Control Group and Powertrain Control Laboratory. Their support helped me a lot in setting up and running the experiments, as well as developing algorithms and preparing manuscripts. I also want to thank Greg Less and Arthur Sinclair from the Battery Lab for assistance with the battery abuse experiments.

My thanks also go to the funding sources that contributed to this work, including National Science Foundation under Grant No. 1762247, Battery Solutions Inc and the State of Michigan through the Small Company Innovation Program (SCIP), Automotive Research Center (ARC) under the Cooperative Agreement W56HZV-14-2-0001 U.S. Army Tank Automotive Research, Development and Engineering Center (TARDEC) Warren, MI.

I'd like to thank all my friends in Ann Arbor for their help and support to make these years happy and unforgettable. Finally, I want to thank my parents Daofa Cai and Huijie Zhang, my girlfriend Can Cui, for their love and support.

TABLE OF CONTENTS

LIST OF FIGURES

Figure

LIST OF TABLES

Table

ABSTRACT

Li-ion battery failure and thermal runaway are serious safety concerns for electric vehicles and energy storage devices. For electric vehicle accidents in recent years, battery thermal runaway events have occurred under unpredictable circumstances, including when vehicles are at rest, not actively being charged or driven. The immediate detection of battery failure within seconds is highly important since the hazard conditions from a single cell thermal runaway can propagate to neighboring cells and the whole system. From a regulation perspective, the proposed global technical regulation No. 20 from the United Nations on Electric Vehicle Safety requires a five-minute advanced warning prior to hazardous conditions caused by a thermal runaway event.

To achieve this detection goal for thermal runaway, a robust and sensitive detection methodology is required. The existing methods for fault detection and diagnosis in the battery pack utilize temperature, voltage, and current measurements. For an automotive battery pack with cells connected in parallel, the current measurements for individual cells are not available, so detection methods relying on individual cell current will not work. Due to the parallel connection of cells, the methods using voltage cannot effectively detect a single cell failure due to a low signal-to-noise ratio. Temperature-based detection methods, due to the sparse temperature measurements in a large pack, are slow in fault detection, with detection speeds usually on the scale of minutes or hours depending on sensor and fault locations. Fast and high confidence fault detection methods are needed to enable a more effective battery management system that can quickly alert and guide emergency response.

Most thermal runaway events are associated with battery internal short circuit (ISC), so ISC will be the focus of this dissertation's study to better understand the cause and the evolution of battery failure. A model of the battery ISC event that predicts temperature, gas generation, and the resulting cell swelling in the early stage of ISC evolution is developed. By monitoring the battery expansion force and adopting an adaptive threshold, an ISC event can be identified before cell venting. Furthermore, by reviewing literature about the composition of the gas expelled from the battery during a venting event in different battery chemistries and states-of-charge, we identify CO_2 as the ideal target gas species for gas detection. Based

on the cell swelling and gas release in battery failure, the dissertation presents fault detection methods using expansion force measurements to capture the abnormal force increase due to battery swelling and Non-Dispersive Infrared (NDIR) CO_2 sensor to detect venting events from battery failure.

By adopting the proposed fault detection method using expansion force and gas sensing, fault detection for a parallel-connected battery module achieves a high signal-to-noise ratio. At the same time, high confidence detection of ISC events can be achieved in seconds, and the methodology can be extended to large battery packs in electric vehicles and stationary energy storage systems.

CHAPTER I

Introduction

1.1 Electric Vehicle Industry and Li-ion Batteries

The global electric vehicle (EV) industry continues to expand rapidly. EV sales grew to more than two million units globally in 2018: an increase of 63 percent on a year-on-year basis.

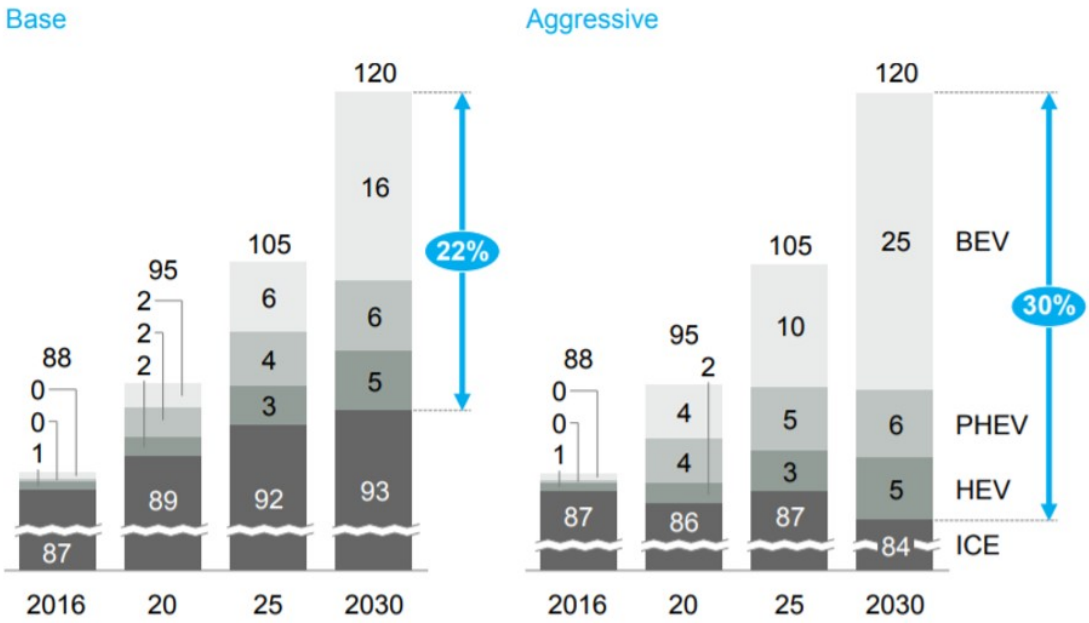

Figure 1.1: Prediction for EV production from 2016 to 2030 for hybrid and pure electric vehicles. The figure shows the global light vehicle production in million per year. Figure from [1].

Within the two million units EV globally, China leads in the market with 1.1 million units, or 51 percent of global EV sales in 2018 [8]. Norway leads electric-vehicle adoption on the EV market side, with EV taking over 40% of the market

share [8]. The global market for electric vehicles has grown at about 60 percent per year, and the EV penetration rate reached 2.2 percent in 2018. It is anticipated that in 2030, hybrid and electric vehicles will account for 22% to 30% of the light vehicle production [1].

Battery safety is one of the main concerns of the EV industry, when comparing heat release during thermal failure, Li-ion batteries have twice as much energy compared to internal combustion engines powered by gasoline fuels per mile range [9]. With the increasing number of EVs on the road, the number of battery safety incidents surged in recent years. A summary of the EV accidents in recent years in the United States is shown in Table. 1.1.

Table 1.1: EV accidents in the United States (until Feb 2020)

Number	Date	Location	Vechile Model	Condition and Cause of Fires
1	Oct 2013	Kent, WA	Tesla Model S	Collision
2	Nov 2013	Murfreesboro, TN	Tesla Model S	Collision
3	Nov 2013	Irvine, CA	Tesla Model S	Charging
4	Oct 2013	Flower Mound, TX	Nissan Leaf	Unknown
5	Aug 2017	Lake Forest, CA	Tesla Model X	Collision
6	Mar 2018	Mountain View, CA	Tesla Model X	Collision
7	Mar 2018	Florida	Tesla Model S	Collision
8	Jun 2018	Los Angeles, CA	Tesla Model S	Spontaneous combustion during operation
9	Feb 2019	Pittsburgh, PA	Tesla Model S	Parked
10	Feb 2019	Davie, FL	Tesla Model S	Collision
11	Feb 2019	Lake Champlain	Tesla Model S	Spontaneous combustion during operation
12	May 2019	San Francisco, CA	Tesla Model S	Parked
13	May 2019	Nevada	Tesla	Caught fire on truck trailer
14	Jan 2020	Arlington Heights, CA	Tesla	Parked
15	Feb 2020	Florida	Porsche Taycan	Parked

Apart from the EV accidents in the United States summarized in the table, EV

accidents happen all over the world. In 2020, after several accidents for Hyundai Kona Electric, Hyundai issued a worldwide recall of 77,000 Kona EVs. In November 2020, General Motors also announced a recall of over 68,000 vehicles for Chevrolet Bolt EVs.

As seen in the summary of EV accidents in the United States, 5 accidents happened while the vehicle was parked, which corresponds to 33% of the total accidents. These accidents happened without explicit abuse conditions and battery internal short circuit (ISC) is considered a major cause for these accidents.

1.2 Background of Battery Failure and Thermal Runaway

1.2.1 Battery Safety with Cell Chemistry

Battery cell safety also varies with different cell chemistry. Currently, there are five Li-ion batteries for battery makers [1], each using a different cathode material. The five Li-ion batteries are:

1. **Lithium Cobalt Oxide (LCO)**. Used extensively in portable electronics. This chemistry has good performance. However, due to the high Cobalt usage, it is relatively expensive and not used in EV applications.

2. **Lithium Nickle Manganese Cobalt (NMC)**. This chemistry takes several forms, such as NMC 111 (the simplest, based on an equal amount of the three elements' atoms), NMC 532/622 (with a higher energy density and lower price than NMC 111 due to a lower cobalt content), and the most recent NMC 811 (with the highest theoretical performance). NMC chemistries were mainly developed for the EV industry but with their high performance and relatively low cost, they may well end up being used in other battery applications.

3. **Lithium nickel cobalt aluminum (NCA)**. This chemistry was the first commercial attempt to substitute some of the expensive cobalt in the LCO cathode for increased nickel content. It has a good energy density and an affordable price, making it ideal for EVs and portable electronics.

4. **Lithium iron phosphate (LFP)**. Intrinsically safer than other cathode chemistries, LFP is not protected by many intellectual property restrictions. Its high power density makes it an ideal candidate for electric tools and e-buses and a good option for EVs.

5. **Lithium manganese oxide (LMO)**. Used in the first EVs, such as the Nissan Leaf, because of its high reliability and relatively low cost. LMO's downside is low

Figure 1.2: Advantages and Disadvantages for Different Cell Chemistries. Figure is remade from [1].

cell durability compared to other competing technologies.

As a result of the recent price spikes for lithium and cobalt, and to achieve a higher range for electric vehicles, NMC chemistries have become automotive OEM's preferred technology in recent years. Tesla, which used the NCA technology for its Model S, now deploys a higher-performing version for the Model 3 with NMC cells [1].

Due to the high cost of the cobalt and the increasing concern regarding its raw material availability, the industry now focuses on low cobalt batteries and, as a result, the high-performing, low-cobalt, high-nickel NMC 811, and perhaps even the newly proposed NMC 9.5.5 battery (with 9 parts of nickel, and 0.5 of cobalt and manganese) [1]. Fig. 1.3 shows the prediction of battery capacity demand by chemistry. High-nickel and low-cobalt NMC cells (NMC 622, NMC 811, NMC 9.5.5) will become the

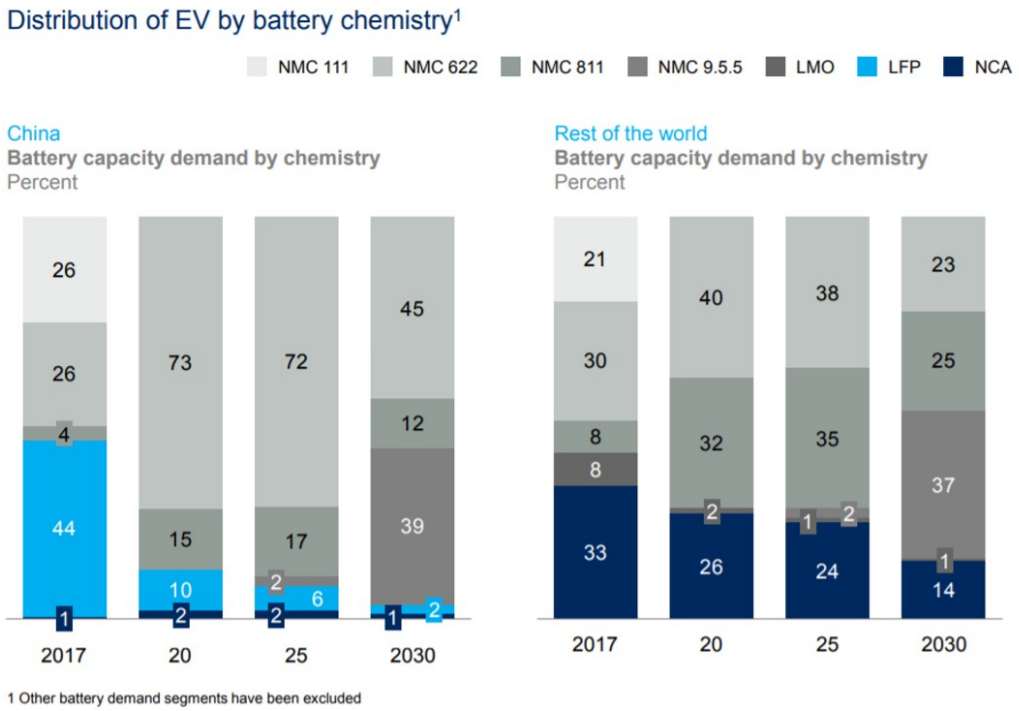

Figure 1.3: Prediction for battery capacity demand by chemistry to 2030. High-nickle and low-cobalt NMC cell will become the most popular cell chemistry for EVs. Figure from [1].

most popular cell chemistry for EVs in the near future.

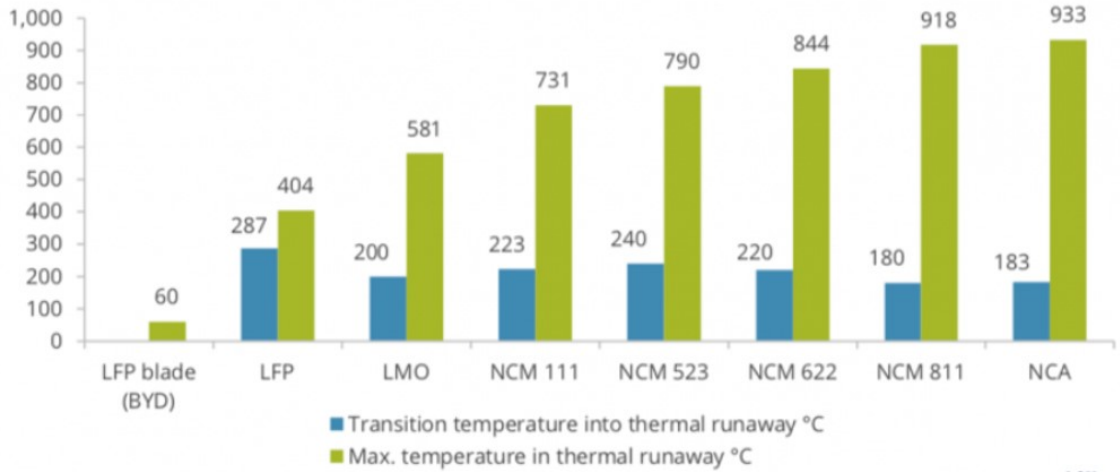

Figure 1.4: Transition temperatures into thermal runaway and maximum temperatures reached by the cell (°C). Figure from [2].

The high-nickel and low cobalt NMC cell has advantages of higher energy density and lower cost per kWh [1] and will be the popular choice of EV in the near future, but at the same time, the cell has worse thermal stability and battery safety comes

into question.

The high-nickel and low cobalt NMC cells (NMC 622, NMC 811) have lower thermal runaway onset temperature, and can reach higher temperature in a battery thermal runaway event, compared to LFP cells or NMC 111 cells, as shown in Fig. 1.4. Specifically, the thermal runaway onset temperature for NMC 622 cells is 220 °C, and 180 °C for NMC 811 cells. The maximum temperature of thermal runaway is 844 °C for NMC 622 cells, and 918 °C for NMC 811 cells.

1.2.2 Abuse Conditions Lead to Battery Failure

There are mainly four abuse conditions for Li-ion batteries that can lead to cell failure and thermal runaway: electrical abuse, mechanical abuse, thermal abuse and internal short circuit (ISC) [6].

1. **Electrical Abuse:** The electrical abuse conditions generally include external short circuit, overcharge, and over-discharge conditions.

The external short circuit forms when the electrodes with voltage differences are connected by conductors. The external short circuit is more like a fast discharging process, with the highest current limited by the mass transfer speed of lithium-ion [6]. Current batteries with positive thermal coefficient (PTC) devices or fuses can reduce the hazards caused by an external short circuit.

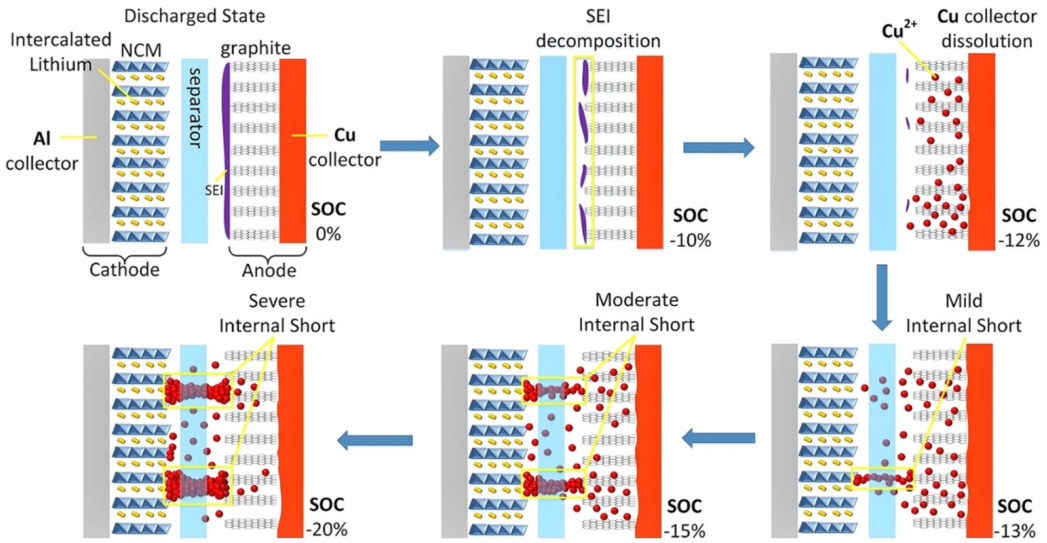

Figure 1.5: Copper dissolution and deposition during overdischarge and the formation of internal short circuit (ISC). Figure from [3].

With the normal operating voltage for Li-ion battery to be 3 to 4.2 V, overcharging

to cell to over 5 V can lead to battery failure [10]. The overcharge can lead to battery thermal runaway that is more energetic than other abuse conditions, because of the additional electrical energy in the battery. Heat and gas generation are the two common characteristics during overcharge. The heat generation comes from ohmic heat and side reactions [6].

Over-discharge of a cell can also lead to cell failure. At a higher degree of over-discharge, the copper collector will start to dissolve [3]. Then the inner migration and deposition of the copper can cause severe ISC of the cell. Studies from Maleki et al. [11] also indicated that if the cell is cycled after an over-discharge process, ISC and thermal runaway can occur.

2. **Mechanical Abuse:** This includes collision and crush of the battery, as well as penetration of the cells. The nail penetration test is the most common study for battery mechanical abuse conditions, as fierce ISC can be instantaneously triggered when the penetration starts. The nail penetration is also regulated in some compulsory test standards of the lithium-ion battery, i.e., GB/T 31485-2015, SAE J2464-2009 [6].

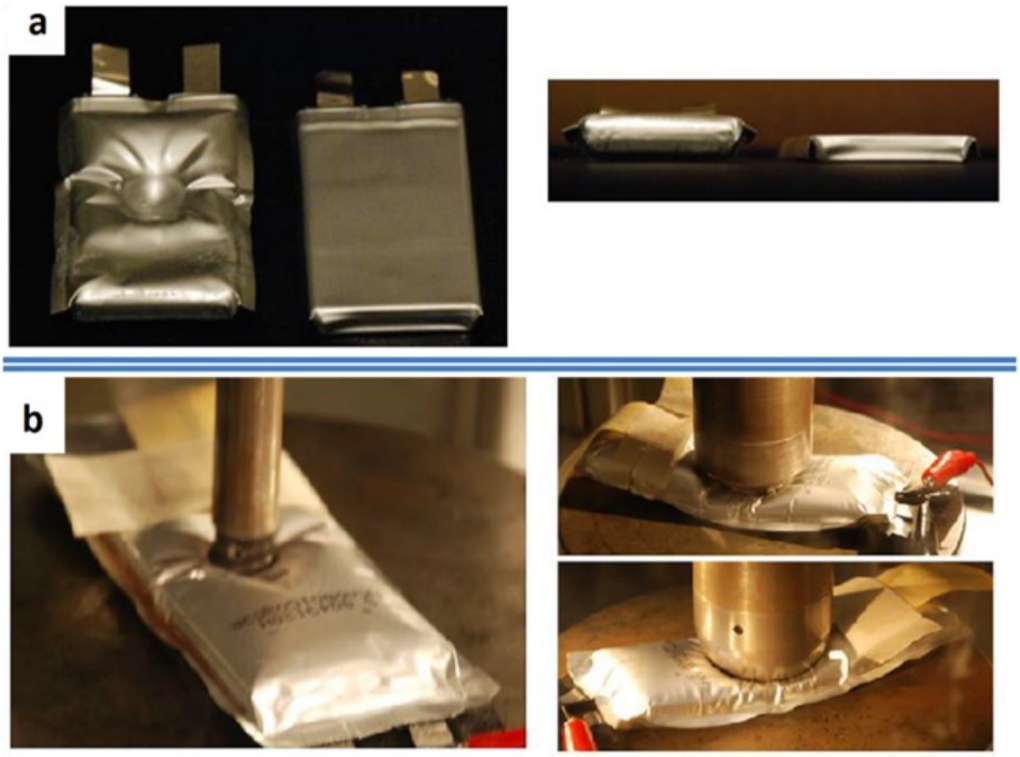

Figure 1.6: Mechanical abuse test for pouch cells. Figure from [4].

3. **Thermal Abuse:** The thermal abuse is the direct cause of the battery thermal runaway. When the battery is overheated, a series of side reactions will occur,

including solid electrolyte interface (SEI) decomposition, anode decomposition, and cathode decomposition. The reaction heat from the side reactions can elevate the cell temperature, and in turn accelerate these side reactions and activate other exothermic reactions. This chain reaction process finally leads to thermal runaway. More details of the side reactions during thermal runaway will be discussed in later chapters.

Most of the prior studies focused on battery thermal abuse tests (or called oven heating tests), because the thermal abuse tests generally deliver repeatable results and can be used to assess the thermal runaway onset temperature. Overheating for battery individual component, i.e., cathode and anode were performed to model and evaluate the side reactions of each battery component [12].

4. **Internal Short Circuit (ISC):** The ISC occurs when the cathode and anode contact with each other due to the failure of the battery separator [6]. Once the ISC is triggered, the electrochemical energy stored in the materials will release spontaneously and can lead to cell failure and thermal runaway events.

The ISC can be a result of explicit abuse conditions such as electrical, mechanical, and thermal abuse. Additionally, there is self-induced ISC triggered without these explicit abuse conditions. The self-induced ISC is believed to originate from contamination or defects during manufacturing [6]. Additionally, at low temperatures charging or during fast charging, lithium plating can happen, which may lead to an ISC resulting in fire or even an explosion [13]. Many EV accidents listed in Table. 1.1 happened while the vehicles were parked. The ISC might play an important role in these accidents which happened without explicit abuse conditions.

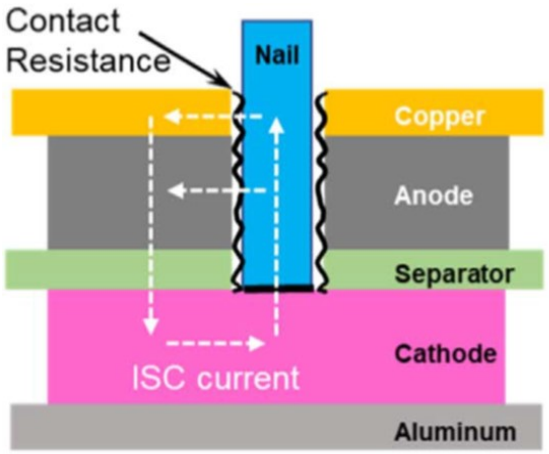

Figure 1.7: Illustration of an ISC event during a nail penetration test. Figure from [5].

Battery ISC events can be categorized into two types: slow self-discharge faults

(battery soft internal short), and fast and severe faults (battery hard internal short). These two types of battery faults can happen due to different abuse conditions. For example, in nail penetration tests, a cell being fully penetrated usually will have a hard internal short and will evolve to thermal runaway quickly [5]. On the other hand, soft internal short circuits are usually associated with dendrite formation caused by lithium plating [13] and can develop over time and use. Due to the high electrical resistance of the soft internal shorts and the resulting slow self-discharge process, battery soft internal short circuits take hours or even days to completely drain the battery charge [14], and usually will not lead to severe hazards including cell venting or thermal runaway. This dissertation focuses on the fast and severe battery faults, which usually feature hard ISC processes and end with thermal runaway events.

The ISC event, as well as other mentioned abuse conditions, can easily lead to thermal runaway. These faults should be identified immediately to take emergency responses. Since the ISC can occur without explicit abuse conditions, while other abuse conditions are all associated with explicit abuse conditions, the ISC event is more difficult to detect. Because of the difficulty and importance in detecting an ISC event, battery ISC will be the focus of this dissertation's study, which will primarily discuss the evolution of battery failure caused by ISC, and the detection methods for ISC, battery failure and thermal runaway.

1.2.3 Evolution of Battery Failure

For fast and severe battery faults, after the start of battery abuse, the battery self-heating process will initiate with a fast temperature increase [6]. Then battery exothermic reactions will be active at high temperatures. Next, cell swelling and gas venting will occur due to the large amounts of gas generated by battery side reactions. At even higher temperatures, these side reactions quickly produce additional heat and can lead to battery thermal runaway, where battery fires and explosions can be observed.

The battery exothermic side reactions at high temperatures mainly include SEI decomposition, anode decomposition, and cathode decomposition. Side reaction models are well established for major exothermic reactions during a thermal runaway event. Previous studies already provide robust reaction kinetic parameters measured from Accelerated Rate Calorimetry (ARC) experiments during thermal runaway [12, 15]. Hatchard [12] developed these side reaction models for major exothermic side reactions including SEI decomposition, anode decomposition, and cathode decomposition. Kim [16] extended the model to include electrolyte decomposition, and these mod-

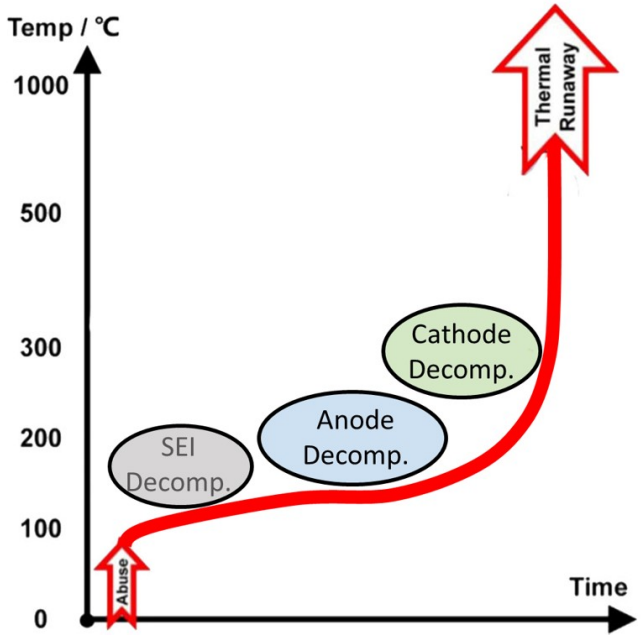

Figure 1.8: Evolution of battery failure from abuse condition to thermal runaway. Figure is remade from [6].

els have been used by many researchers over the years. Ren [17] developed a set of thermal runaway side reaction chemical kinetics based on DSC testing that includes six exothermic reactions in the model, SEI decomposition, anode-binder reaction, anode-electrolyte reaction, cathode-electrolyte reaction, cathode-binder reaction, and cathode decomposition.

Looking at the early stage of battery failure, SEI decomposition is the main active reaction and can directly produce gas [6], leading to cell swelling and expansion force increase. After the cell rupture, the produced gas will be released to the outside. The SEI decomposition plays an important role in the cell expansion force increase and gas release, and its reaction mechanism is as following:

$$(CH_2OCO_2Li)_2 \rightarrow Li_2CO_3 + C_2H_4 + CO_2 + 0.5O_2$$

The modeling work in this dissertation will place emphasis on correlating the gas evolution from SEI decomposition with cell expansion force increase and gas release after cell rupture.

1.3 Challenges of Battery Safety in Electric Vehicle Industry

The EV industry has a wide set of battery safety testing standards to improve battery safety. However, battery failure still occurs in real life even though these cells have passed the safety testing standards. In this section, we first review the testing standards and their limitations, and then discuss the challenges of battery safety in electric vehicles.

1.3.1 Limitations of Battery Failure Testing Standards

The testing standards for battery safety in EV industry are mostly pass/fail battery abuse testing. Examples include SAE International (SAE) Standard J2929 "Electric and Hybrid Vehicle Propulsion Battery System Safety Standard - Lithium-based Rechargeable Cells", and UL 2580 "Batteries for Use in Electric Vehicles".

The SAE J2929 and UL 2580 standards involve battery testing of thermal shock, vibration, mechanical shock, external short circuit, overcharge, over-discharge, crush, open flame test, high rate discharge without cooling, drop test, immersion, and fault analysis of the system design [18]. The testing standards are to ensure passive battery safety of fresh cells. On the other hand, due to the complexity of real-world conditions and battery conditions change from cell aging, EV accidents caused by battery failure still happen in real life and these accidents can even happen without explicit abuse conditions.

To this end, active safety measures are needed in EVs to leverage the hazards of battery safety events. The active battery safety measures include early warning and detection of battery failure, deactivate or de-energize the battery pack, and fire suppression if a battery fire exists. Immediate detection of battery failure is the key to active safety measures and will be the focus of this dissertation.

1.3.2 Challenges of Fault Detection in Battery Packs

Fault detection is the key to achieve functional safety in battery packs. The detection should be made within seconds or minutes after the battery failure occurs. From the regulation perspective, the proposed global technical regulation No. 20 by the United Nations on Electric Vehicle Safety (EVS) requires that in the event of thermal runaway, the vehicle should provide a warning indication to allow egress five minutes prior to the development of hazardous conditions inside the passenger compartment [19].

Existing methods of detecting battery faults are usually based on voltage, current, or surface temperature measurements, but these methods are intended for identifying soft internal short circuit events. These methods use current, voltage, and temperature signals to compare with other cells [20] or battery models [21]. Detection can be made once the faulty cell deviates from other cells or the battery models and can take up to hours to identify the soft short circuit [20, 22]. However, for the detection of fast and severe battery faults, including battery hard internal short and thermal runaway in battery packs, these methods will have different drawbacks.

Looking at the voltage signal, a significant voltage drop can be detected when the ISC occurs before thermal runaway [23] or when the current interrupt device (CID) opens at cell venting [24]. Voltage-based methods work well for a single cell and also have a fast detection speed, as the voltage drop is sharp and instantaneous after an ISC event [25] or in a thermal runaway event [26]. In electric vehicle battery packs, the cells are often also connected in parallel and series. For a pack with p cells in parallel and s cells in series, the voltage measurement from the battery management system will deliver s number of voltage signals for each parallel cell group. As an example, the Tesla Model S battery packs have modules in series that contain strings of 74 cells in parallel. For large-format cells, similarly, they have multiple parallel stacked layers [27]. Because of the parallel connection, the voltage is rather stable when an individual cell voltage evolves under an internal fault [7], making the fault detection with voltage difficult.

Detecting cell internal resistance change can also be a good indication of battery faults, especially for diagnosing soft ISC that can potentially lead to thermal runaway [14, 22]. After the occurrence of an ISC, the cell polarization resistance (R_2) can increase by 355% [22], and the standard deviation of cell internal resistance during cycling will also increase significantly [20]. However, for parallel circuits, the measured internal resistance is the average of the internal resistance of all cells in parallel [28]. Ultimately, because the fault detection methods using cell internal resistance rely on the voltage response for the given current, a large number of parallel cells can lead to a poor signal-to-noise ratio for internal resistance measurement.

Other fault detection methods use surface temperature and current measurements. Surface temperature-based methods detect sharp increases in temperature but require significantly more temperature sensors in a pack to increase the observability [29]. Monitoring abnormal single cell current based on multiple current measurements [30] is also effective for detecting a short circuit in individual cells; however, the method requires additional current sensors to monitor the current of individual cells. Both

surface temperature and current-based methods are cost-prohibitive for a large-scale battery pack.

Detection of cell venting based on pressure is usually in seconds, but pressure detection only works for well-sealed packs. The pressure signal generally has a poor signal-to-noise ratio and the short duration of the increased pressure can be easily missed by the sensor [27]. During a nail penetration test, the pressure sensor showed a short spike only a few seconds long with around a 20% increase in pressure [27].

Table 1.2: Summary of battery fault detection methods

Measurement	Principle	Signal-to-Noise Ratio	Detection Speed	Practicality
Voltage	Monitor cell voltages for sudden voltage drops or estimate cell internal resistance	< 3 for parallel circuits	Instantaneous	Good, no additional cost
Temperature	Monitor the temperature at various locations within the pack	> 100	Minutes or hours, depending on sensor location	Good, no additional cost
Current	Monitor individual cell currents in parallel circuits	> 1000	Instantaneous	High cost for large packs
Pressure	Monitor pressure in modules for sudden pressure increase	< 15	Seconds	Only works for well-sealed packs
Force	Monitor the expansion of cell stacks in battery packs	> 80	Seconds	Might suffers irreversible drift of force over time
Gas	Monitor certain gas composition within the pack	> 100	Seconds	Might suffers gas sensor drift and failure over time

As mentioned early, in a battery ISC event, the expansion force will increase due to cell swelling, and the generated gas will be released after cell rupture. This leads to the potential of using expansion force and gas to detect battery faults in large packs.

Due to the drawbacks of the existing methods in battery pack fault detection, this dissertation mainly focuses on developing fault detection methods using expansion force and gas measurements. The commonly used approaches for battery fault detection are summarized in Table 1.2.

1.4 Dissertation Organization

This dissertation will primarily address the modeling and detecting battery internal short circuit (ISC) and thermal runaway events. While most of the previous work on battery fault detection focused on the single-cell case, detection of battery failure in a large battery pack, especially for parallel-connected cells, is more challenging but

few works have explored it. In this dissertation, we developed the fault detection methodology for a parallel-connected battery module that can be extended to a battery pack. The specific contribution from this dissertation and relevant publications are:

1. Modeling battery internal short circuit (ISC)

In Chapter II, to help understand battery failure and evolution during thermal runaway, the battery ISC is carefully studied and modeled. The battery ISC model involves a three-section temperature model, that discretizes the battery into three temperature regions to better address the large temperature gradients that occur at the localized area around the fault region. This model requires proper tuning to match the ISC experiment data, but it shows great potential to explain the complicated behavior of the ISC evolution. Specifically, the three-section model explains why the expansion force rises in the early stage of battery ISC events, and demonstrates the potential of using expansion force and gas evolution process for early indication of battery faults. Related publications:

- Cai, Ting, Anna G. Stefanopoulou, and Jason B. Siegel. "Modeling Li-ion battery thermal runaway using a three section thermal model." Dynamic Systems and Control Conference. Vol. 51906. American Society of Mechanical Engineers, 2018.

- Cai, Ting, Anna G. Stefanopoulou, and Jason B. Siegel. "Modeling Li-Ion Battery Temperature and Expansion Force during the Early Stages of Thermal Runaway Triggered by Internal Shorts." Journal of The Electrochemical Society 166.12 (2019): A2431.

2. Internal short circuit detection using force measurement

In Chapter III, internal short circuit detection using force measurement is discussed. High confidence level fault detection for battery internal short circuits is needed. However, existing methods using temperature measurements suffer poor observability. To address this issue, based on the large expansion force rise in the internal short circuit events, a fault detection scheme is proposed to capture the abnormal force increase by using expansion force measurements. To achieve high confidence level detection, voltage measurements are used to detect abnormal voltage behaviors. Related publication:

- Cai, Ting, Sravan Pannala, Anna G. Stefanopoulou, and Jason B. Siegel. "Battery Internal Short Detection Methodology Using Cell Swelling Measurements." 2020 American Control Conference (ACC). IEEE, 2020.

3. Gas detection for early warning of battery failure

In Chapter IV, the gas detection method is explored due to its fast response and easy implementation in a pack. By summarizing the past literature on the vent-gas compositions under different testing conditions, we propose CO_2 as the target gas species due to the high concentrations in all vent-gas, presence in first venting event, ability to detect cell leakage, and good sensor feasibility for Non-Dispersive Infrared (NDIR) CO_2 sensor. The CO_2 sensing will work for different battery chemistries and different States of Charge. The gas detection response in a battery pack is then analyzed and the volume-averaged CO_2 concentration is estimated to help determine the gas detection threshold. Related publication:

- Cai, Ting, Puneet Valecha, Vivian Tran, Anna G. Stefanopoulou, and Jason B. Siegel. "Detection of Li-ion Battery Failure and Venting with Carbon Dioxide Sensors." eTransportation 7 (2021): 100100.

4. Simulating Cell venting and gas detection

In Chapter V, a cell venting model and a CO_2 gas generation model will be introduced that enables the estimation of CO_2 released in a battery failure event. Based on the models, a simulation for battery failure in a battery storage drum is shown to demonstrate the fast response of gas detection over the temperature monitoring method. Related publication:

- Cai, Ting, Vivian Tran, Anna G. Stefanopoulou, and Jason B. Siegel. "Modeling Li-ion Battery First Venting Events Before Thermal Runaway." (submitted for 2021 Modeling, Estimation and Control Conference)

- Cai, Ting, Anna G. Stefanopoulou, and Jason B. Siegel. "Early Detection for Li-Ion Batteries Thermal Runaway Based on Gas Sensing." ECS Transactions 89.1 (2019): 85.

5. Battery fault detection in parallel connected module

In Chapter VI, battery fault detection in parallel connected cells or battery modules is discussed. For fault detection in parallel-connected battery modules, the

voltage-based method suffers a low signal-to-noise ratio. Temperature and current-based detection methods are not feasible in battery modules. To address this issue, we develop a fast and high confidence level detection method of hard internal short circuit events for a battery module. In this chapter, we will combine the methodologies discussed in previous chapters, and measure cell expansion force, and monitoring CO_2 concentrations in a battery module. Related publication:

- Cai, Ting, Peyman Mohtat, Anna G. Stefanopoulou, and Jason B. Siegel. "Li-ion Battery Fault Detection in Large Packs Using Force and Gas Sensors." In IFAC World Congress 2020. 2020.

Finally, in Chapter VII, overall conclusions and outlook are presented.

CHAPTER II

Modeling Battery Internal Short Circuit

2.1 Introduction

Most of the existing models focus on thermal runaways initiated by overheating. Examples include the model by Feng [31], which described the battery thermal runaway electrochemical-thermal behavior when overheating the cell. These models work well for battery overheating tests, where the temperature gradient within the cell is small. However, for battery failure triggered by an internal short circuit, where the temperature gradient within the cell is large, few publications have addressed it. An internal short circuit (ISC) model is needed with four sub-models: an electrical model for the internal short circuit process, a side reaction model for exothermic reactions of active materials, a thermal model for battery temperature, and a gas evolution model to predict early gas generation.

For battery thermal models in a thermal runaway event, Hatchard [12] used a spatially discretized thermal model, with N concentric rings, to account for the radial temperature distribution of a battery during thermal runaway. Since the entire cell is at an elevated temperature when the exothermic process begins, the reaction progresses more uniformly along the radius of the cell. Coman [32] used lumped thermal models to describe battery temperature during thermal runaway. The lumped thermal model assumes a uniform temperature distribution and one temperature state to represent the whole cell. This assumption is valid for an 18650 cell, which has a small Biot number ($B_i = 0.051$) [32]. In the case of a local internal short circuit, however, the ohmic heat generation will be concentrated in a small localized area, causing a large spatial temperature gradient in a focused space. To address this inhomogeneity, others have used a finite element approach, but with high computation cost and difficulty in tuning [33, 34]. A reasonable trade-off is needed between computational complexity and accuracy in the model. In this chapter, the proposed battery ISC

model divides the battery into three sections: core, middle layer, and surface layer [35], and identifies the heat released in each section.

In modeling the internal short, the resistance of the ISC is a critical parameter for determining the severity and time to onset of the thermal runaway event [22]. However, few papers address calculation of the short resistance depends on the area of the separator failure. Guo [3] explained the ISC caused by over-discharge, and used experimental data to fit a curve of ISC resistance with over-discharge capacity. Coman [32] developed a model for energy released due to the ISC with an efficiency factor that was fitted to their experiment data. The fitting approach worked well with the specific cells in the experiment, but is difficult to be applied to varying Li-ion battery chemistries. This study presents an electrical model that describes ISC, and proposes a finite element method for solving ISC resistance of the battery for small geometric areas.

During the early stage of thermal runaway, a significant amount of gas and electrolyte is vented to the outer regions of the battery. Coman [36] studied and modeled the electrolyte and ejecta venting during thermal runaway. Previous experimental studies for commercial 18650 Li-ion batteries from Lammer et al. [37] on the composition of vented gas showed that most of the gas is CO_2 during the first gas venting event. Based on these results, our study assumes that gas from SEI decomposition is the most significant contributor to battery swelling and force signal rise during the first few seconds following an ISC event. This study is the first attempt to make a connection between side reactions and force of battery swelling for modeling purposes.

To tune and validate the model, two experiments were conducted with 4.5 Ah pouch cells for which an ISC was triggered at 57 °C with different initial State of Charge (SOC). Here we used a wax-based melt device in the separator to trigger the internal short [38]. In our experiments, we demonstrated two modes for the ISC event. The cell with 50% SOC didn't trigger thermal runaway, while the cell with 100% SOC went into a quick thermal runaway. With proper tuning using the measured surface temperature, the model fits force signal on both experiments, by predicting the gas volume change inside the cell compared with force measurement. Although this ISC model requires proper tuning and cannot predict the two modes of ISC events, this model shows great potential and can explain some complicated behavior of the ISC events, including the early rise of force signal. The model and experiments with early rise of force signal show the potential of using the mechanical behavior as an early indicator for ISC induced thermal runaway.

2.2 Thermal Runaway Model

The battery's internal temperature states are divided according to three sections, and the mass of each section is scaled proportionally to its volume fraction. This uneven coarse discretization better captures the relatively small area adjacent to the internal short circuit which heats more rapidly than the surrounding volume. The remainder of the cell mass, which lags in heating, contains the bulk of the cell material. As Fig. 2.1 illustrates, the overall thermal runaway model includes a three-state thermal model, a side reaction model which tracks the consumption of active materials, and an electrical equivalent circuit model. The model has three temperature states, four side reaction states in each section, and one state for cell state of charge according to an electrical equivalent circuit model. In total, the three-section model consists of 16 states.

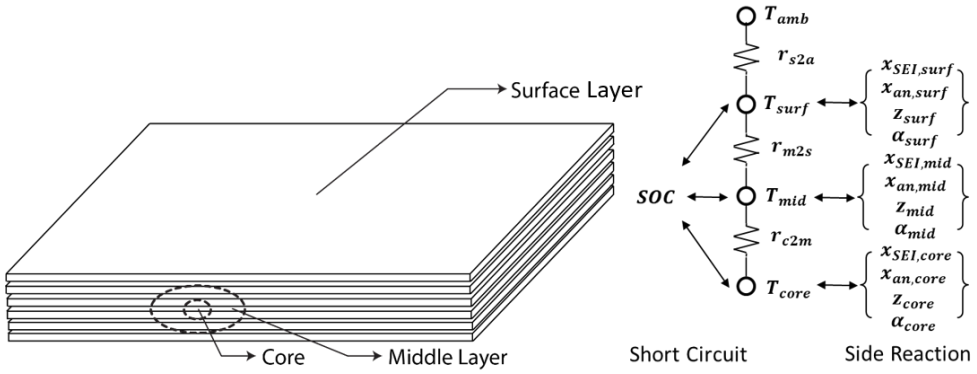

Figure 2.1: Three section model with battery discretized into core, middle layer and surface layer

2.2.1 Three-State Thermal Model

For thermal runaway triggered by ISC, the ISC area has a significant volumetric heat rate and will have a relatively fast temperature rise compared to the surface of the cell. To address this inhomogeneity of temperature within the battery, we need to discretize the battery into several sections. We found that three sections for temperature discretization achieved good accuracy while at the same time maintained reasonable computational complexity.

A three-state thermal model describes battery core temperature (T_c), middle layer temperature (T_m), and surface layer temperature (T_s). The battery core represents the area in which the ISC first occurs. In Figure 2.1, this location is schematically

shown at the center of the cell. However, it need not necessarily be located at the geometric center. The proposed model also applies to cases where the ISC is located near the surface, as shown later in the experimental results. It is the relative volumes rather than the specific ISC location, that is critical for capturing the temperature rise during thermal runaway. Specifically, the dynamic evolution of the core temperature state is

$$C_p m_{core} \frac{dT_{core}}{dt} = (\dot{Q}_{exo,core} + \dot{Q}_{ohmic,core}) + \frac{T_{mid} - T_{core}}{r_{c2m}} \tag{2.1}$$

where T_{core} and T_{mid} represent the core and middle layer temperatures respectively and r_{c2m} is the thermal resistance between the core and middle layer. Similarly the middle and surface layer temperatures are given by

$$C_p m_{mid} \frac{dT_{mid}}{dt} = (\dot{Q}_{exo,mid} + \dot{Q}_{ohmic,mid}) - \frac{T_{mid} - T_{core}}{r_{c2m}} + \frac{T_{surf} - T_{mid}}{r_{m2s}} \tag{2.2}$$

$$C_p m_{surf} \frac{dT_{surf}}{dt} = (\dot{Q}_{exo,surf} + \dot{Q}_{ohmic,surf}) + \frac{T_{amb} - T_{surf}}{r_{s2a}} - \frac{T_{surf} - T_{mid}}{r_{m2s}} \tag{2.3}$$

The r_{c2m}, r_{m2s}, r_{s2a} terms are equivalent thermal conduction resistance.

The battery core section refers to the battery area affected by initial ISC, and the m_{core} parameter can be derived if the ISC area is known. Theoretically, the mass ratio of each layer equals to the volume ratio of the each layer when assuming uniform density ($m_{core} = m_{cell}\frac{V_{core}}{V cell}$, $m_{mid} = m_{cell}\frac{V_{mid}}{V cell}$), where m_{cell} is the battery cell mass, and V_{core} and V_{mid} are the volumes of core and middle layer). In this study, for a cell with a wax-based separator, the core mass ideally can be calculated by the area of wax part separator and the electrode sheet thickness. The volume of a cylindrical ISC area can be expressed as

$$V_{core} = \pi r_{short}^2 H \tag{2.4}$$

where r_{short} is the radius of short circuit region, and H is the height of cylindrical short area, which is the sum of two electrode sheets thickness and the separator thickness. However, the initial ISC also heats up regions outside of ISC area during the internal short circuit process, so the relative size of the volumes for three sections are tuned in this study. The correlation between the three section sizes and the ISC device volume will be explored in a subsequent work with more available data.

The total heat generation by the side reactions is given by

$$\dot{Q}_{exo,*} = \dot{Q}_{an,*} + \dot{Q}_{ca,*} + \dot{Q}_{SEI,*} \tag{2.5}$$

where $*$ corresponds to the core, middle and surface layers. The total heat rate from all side reactions depends on the three exothermic decomposition reactions in each layer. These reactions drive the temperature rise, and the temperature rise will accelerate these reactions, leading to thermal runaway.

2.2.2 Electrical Model

During a thermal runaway event, besides exothermic side reactions that generate heat, the battery short circuit will also generate ohmic heat. The thermal and decomposition evolution depends on the rate of this ohmic heat generation and its dissipation rate to the surrounding material. This study focuses on the internal short circuit that occurs in a small region of a battery and presents a model for its local heating. The battery terminal voltage can be represented by an equivalent circuit model

$$V_T = U(SOC) - I \cdot R_{cell} \tag{2.6}$$

where I is the discharge current, which is equal to the short current I_{short} when there is no load, as shown in Fig. 2.2a. The nominal cell internal resistance is R_{cell} and $U(SOC)$ is the battery open circuit voltage (OCV). The OCV is a function of SOC, as shown in Fig. 2.2b.

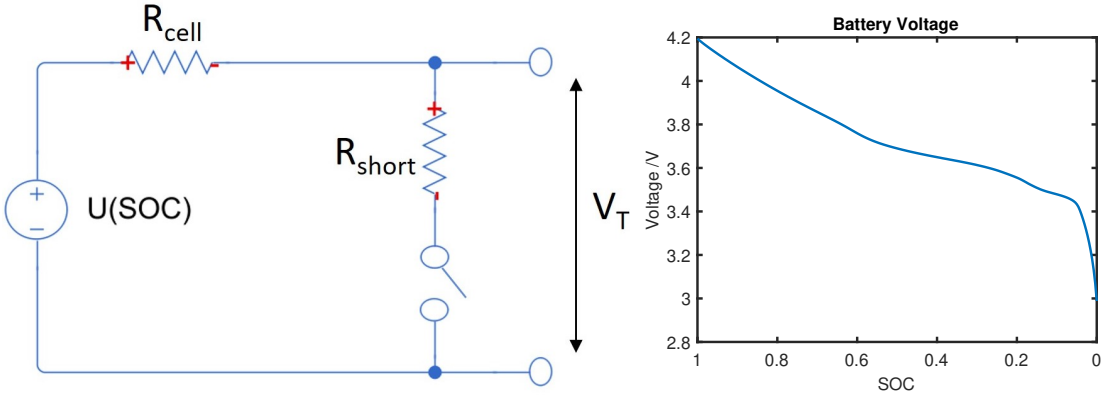

(a) (b)

Figure 2.2: Electrical model (a) Equivalent circuit model for ISC. (b) Battery open circuit voltage $U(SOC)$.

Rheinfeld [39] used the 1 kHz impedance as cell resistance to evaluate the theoretical maximum short circuit at the first few seconds of the internal short process. Here, 1 kHz impedance of the cell from EIS testing ($R_{1kHz} = 4.76m\Omega$) will be used to represent cell resistance for an modeling internal short circuit.

2.2.2.1 Equivalent Circuit Model for ISC

From the ISC resistance, an equivalent circuit model can be developed to describe the internal short circuit process. Previous studies on ISC mechanisms have also used an equivalent circuit model with area dependent resistance [3]. In this study for a self-induced thermal runaway case, we assume no external wires connecting the positive and negative electrodes of the cell. The corresponding equivalent circuit model is shown in Fig. 2.2a. Therefore short circuit current can be found using Kirchoff's laws directly for the simple circuit.

$$I_{short} = \frac{U(SOC)}{R_{cell} + R_{short}} \tag{2.7}$$

The total heat release due to self discharge is given by,

$$\dot{Q}_{ohmic} = I_{short}^2(R_{cell} + R_{short}) \tag{2.8}$$

To be noted, the ohmic heat I^2R_{short} is distributed only in the short circuit area, and the overall heat rate I^2R_{cell} is distributed among all cell. Specifically, when the ISC starts in the battery core, the ohmic heat will be distributed as following:

$$\dot{Q}_{ohmic,core} = I_{short}^2 R_{short} + \frac{m_{core}}{m_{cell}} I_{short}^2 R_{cell} \tag{2.9}$$

$$\dot{Q}_{ohmic,mid} = \frac{m_{mid}}{m_{cell}} I_{short}^2 R_{cell} \tag{2.10}$$

$$\dot{Q}_{ohmic,surf} = \frac{m_{surf}}{m_{cell}} I_{short}^2 R_{cell} \tag{2.11}$$

where the subscript core, mid, surf corresponds to the core, middle and surface layers of the battery respectively. Adjusting the resistance values can increase the heat rate in the short circuit area to be much higher than the rest of cell so that the short area will experience significant temperature rise before the rest of the cell.

2.2.2.2 ISC Resistance

Four major types of internal short circuits have been discussed in previous studies [25], with Cathode to Anode ISC being the most common type of ISC. Typically the ISC area is small in comparison with the total cell area. In cathode to anode ISC, if the ISC area is caused by a penetrated separator and the cathode and anode is connected through high conductivity materials, such as iron, then the resistivity of the electrode's active material dominates the resistance of the short. A zero-th order approximation of true electric resistance can be derived using geometric resistance:

$$R_{geo} = \rho \frac{L}{S} \tag{2.12}$$

where ρ is electric resistivity, L is the length and S is the cross-sectional area for uniform resistive property material.

For small areas, however, the distribution of the potential field near the edge cannot be ignored. Thus, a Comsol simulation was developed for a unit current flowing through the ISC area. The simulation solves Ohm's law in 3D at a fixed applied current to compute the electric field:

$$\mathbf{E} = \rho \mathbf{J} \tag{2.13}$$

with $\mathbf{J}$ being the current density. Then R_{3D} is calculated numerically by:

$$R_{3D} = \frac{-\int \mathbf{E} \cdot d\mathbf{x}}{I} \tag{2.14}$$

where $d\mathbf{x}$ is the element of path along electric field, and I is the total applied current, which equals to the integration of current density over the cross-sectional area ($I = \int \mathbf{J} dxdy$).

Figure 2.3a shows a 2-D slice of the electrical potential distribution of ISC current path at the short circuit area with a unit applied current. The ISC resistance is obtained numerically from this simulation for a range of areas. The ISC resistance is nearly inversely proportional to the ISC area, where a smaller ISC area will have larger short resistance. As Fig 2.3b indicates, geometric resistance estimates the ISC resistance well for large ISC areas. However, for small areas, the geometric resistance overestimates the ISC resistance where the edge effects are significant. Detailed results for the comparison of equivalent ISC resistance (R_{3D}) and geometric resistance (R_{geo}) are shown in Fig. 2.3b. Based on this result, R_{geo} is a good estimation of R_{3D} when the ISC resistance is lower than 5Ω. For ISC resistance greater than 5Ω the area

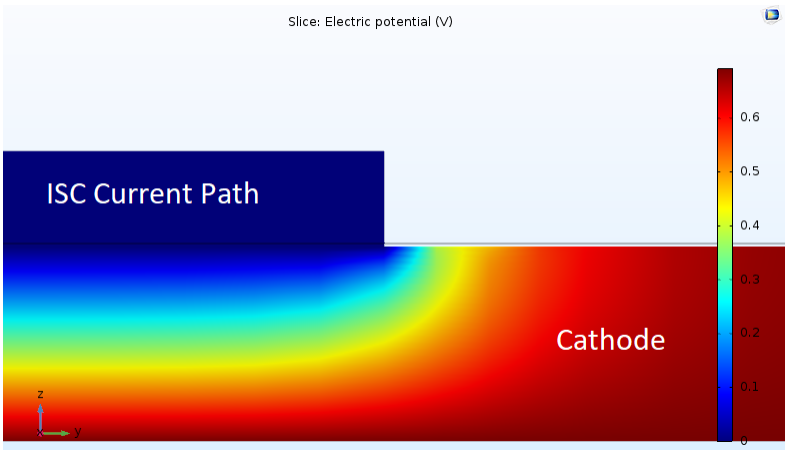

(a)

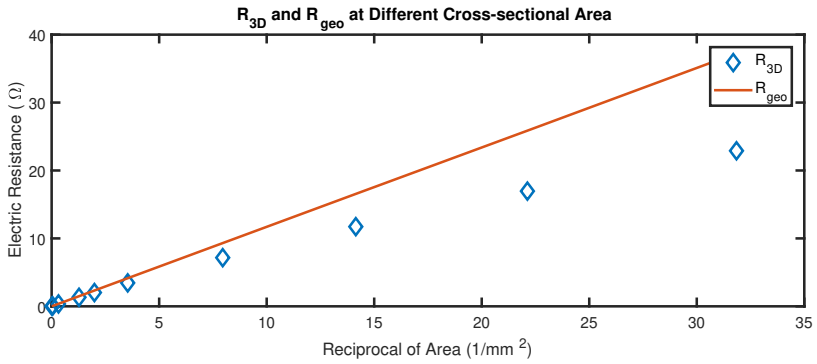

(b)

Figure 2.3: ISC resistance computation. (a) Electric potential at short circuit Area. (b) Comparison between R_{3D} and R_{geo}.

dependence is non-linear, and the full 3D potential field should be evaluated as shown in Figure 2.3a, if the short area is known. In the following study, R_{3D} will be adopted for ISC resistance R_{short} greater than 5Ω based on the error shown in Figure 2.3b.

2.2.2.3 Temperature Dependency for Cell Resistance

As the cell temperature increase significantly during the thermal runaway process, the temperature dependency for electrical resistance needs to be taken into consideration. The diffusivity of ion transport increase exponentially with temperature[40]. The cell resistance is then assumed to decrease exponentially with battery core temperature rise, while the short circuit resistance is assumed constant with temperature change. Under this assumption, an exponential temperature dependency relation is selected from Lin[41] to represent the cell resistance:

$$R_{cell} = R_{e,ref} \ \exp\left(T_{ref}/T\right) \tag{2.15}$$

where $R_{e,ref}$ is the reference resistance value at a reference temperature T_{ref}. The exponential relationship is directly adopted from Lin[41], while the reference resistance value is selected to reflect the measured 1 kHz impedance at 20 °C. In this study, $R_{e,ref}$ is taken as $0.0246m\Omega$, and T_{ref} is taken as $1543K$[41].

However, since the cell temperature is discretized in this model, so the cell resistance should be expressed as a function of three sections temperature. The cell resistance can be represented by the three sections, where the temperature dependency comes from the temperature of each section:

$$R_{cell} = \frac{1}{1/R_{cell,core} + 1/R_{cell,mid} + 1/R_{cell,surf}} \tag{2.16}$$

where $R_{cell,core}$, $R_{cell,mid}$, $R_{cell,surf}$ is the cell electrical resistance based on core, middle layer and surface layer. The temperature dependency for each of the electrical resistances can be expressed as:

$$R_{cell,*} = R_{*,ref} \ \exp\left(T_{ref}/T_{*}\right) \tag{2.17}$$

where $*$ corresponds to core, middle layer and surface layer. $R_{*,ref}$ is the reference resistance value for layer $*$, and is a function of mass ratio of layer $*$.

$$R_{*,ref} = \frac{R_{e,ref}}{m_{*}/m_{cell}} \tag{2.18}$$

where m_{*} is the mass or layer $*$, and $R_{e,ref}$ is the reference resistance value for the whole cell ($0.0246m\Omega$).

2.2.2.4 Additional Assumptions for Short Circuit

We assume that the core part structure collapses at the melting temperature of the current collector and will interrupt the short. We then assume that the internal short circuit at that high-temperature area will stop. Further, due to heat propagation, the neighboring area will trigger internal short circuit once the separator in neighboring areas melt. For simplicity, we assume that the short circuit happens only at one place at a time, and that the neighboring area starts its internal short after the previous section collapses.

2.2.3 Side Reaction Model

To simplify the study, the side reaction model includes only three major side reactions, SEI decomposition, anode decomposition, and cathode decomposition [12]. The side reaction model used in this work will be based on the work of Coman [32], where the Arrhenius equations for the temperature dependent reaction rates of thermal runaway side reactions are included. To match the NMC cathode material used in our experiment, all side reaction parameters are adopted from Dong[42]. Most of the reaction parameters are the same as Coman[32], although some parameters are different, including the heat release, activation energy, pre-exponential term of NMC cathode decomposition, and the pre-exponential term of SEI. Detailed values and sources for side reaction parameters are listed in Table 2.1.

2.2.3.1 Solid Electrolyte Interface (SEI) Decomposition

The SEI starts to decompose first at temperatures above 130 °C [43].

$$\frac{dx_{SEI,*}}{dt} = -A_{SEI} \cdot x_{SEI,*} \cdot \exp\left(-\frac{E_{SEI}}{k_b T_*}\right) \tag{2.19}$$

where $x_{SEI,*}$ is the fraction of Li in the SEI in layer * ($* = core, mid, surf$), A_{SEI} is the frequency factor for SEI decomposition and E_{SEI} is the activation energy for SEI decomposition, k_b is Boltzmann's constant, and T_* is the temperature in layer *. The heat released by SEI decomposition in each layer * is given by:

$$\dot{Q}_{SEI,*} = -m_{an,*} \cdot h_{SEI} \cdot \frac{dx_{SEI,*}}{dt} \tag{2.20}$$

where h_{SEI} is the reaction enthalpy of SEI decomposition. The mass fraction of anode material in each layer is given by the total anode mass multiplied by the mass fraction of the layer to the cell total $m_{an,*} = m_{an} \cdot m_*/m_{cell}$.

2.2.3.2 Anode Decomposition

Intercalated lithium in graphite starts to react with the electrolyte at high temperature. This side reaction starts at around 180 °C [44].

$$\frac{dx_{an,*}}{dt} = -A_{an} \cdot x_{an,*} \cdot \exp\left(-\frac{E_{an}}{k_b T_*}\right) \cdot \exp\left(-\frac{z_*}{z_0}\right) \tag{2.21}$$

where $x_{an,*}$ is the fraction of Li in the anode in layer *, A_{an} is the frequency factor for anode decomposition and E_{an} is the activation energy for anode decomposition. In addition, the relative SEI thickness (z) is also considered in anode decomposition (tunneling effect [15]).

$$\frac{dz_*}{dt} = A_{an} \cdot x_{an,*} \cdot \exp\left(-\frac{E_{an}}{k_b T_*}\right) \cdot \exp\left(-\frac{z_*}{z_0}\right) \tag{2.22}$$

where z_* is a dimensionless number representing relative SEI thickness in layer *. The heat released by decomposition of the anode in each layer * is given by:

$$\dot{Q}_{an,*} = -m_{an,*} \cdot h_{an} \cdot \frac{dx_{an,*}}{dt} \tag{2.23}$$

where h_{an} is the reaction enthalpy of anode decomposition.

2.2.3.3 Cathode Decomposition

Finally at the highest temperature, the cathode material starts to decompose releasing oxygen and heat. For the NMC battery chemistry, this side reaction usually starts at 240 °C [26]. The rate of conversion, of the cathode active material is given by:

$$\frac{d\alpha_*}{dt} = \alpha_*(1-\alpha_*) \cdot A_{ca} \cdot \exp\left(-\frac{E_{ca}}{k_b T_*}\right) \tag{2.24}$$

where α_* is the degree of conversion of cathode decomposition in layer *. The reaction stops when $\alpha_* = 1$ and all of the cathode material in that layer has been consumed. A_{ca} is the frequency factor for cathode decomposition and E_{ca} is the activation energy for cathode decomposition. The heat generation in each layer is proportional to the rate of conversion given by:

$$\dot{Q}_{ca,*} = m_{ca,*} \cdot h_{ca} \cdot \frac{d\alpha_*}{dt}. \tag{2.25}$$

where h_{ca} is the reaction enthalpy of cathode decomposition. Similarly to the anode, the mass fraction of cathode material in each layer is given by the total anode mass multiplied by the mass fraction of the layer to the cell total $m_{ca,*} = m_{ca} \cdot m_*/m_{cell}$.

Equations 2.19-2.25 describe the thermal runaway side reactions. The temperature in Eq. 2.19-2.25 should be the local temperature (core, middle, surface layer). At different regions of the battery, we will see different reaction rates for the side reactions.

2.2.4 Charge Depletion with Internal Short Circuit (ISC) and Side Reactions

The anode decomposition and charge depletion due to ISC are coupled in this work, as they both consume Li in the anode. As shown in Figure 2.4, both processes cause SOC to decrease. The SOC is an important parameter in the side reaction model and the electrical model which impacts the total heat release. Higher initial SOC increases the chance of thermal runaway since the heat released during the ISC is larger. After coupling, SOC can be expressed as the weighted average fraction of Li of the anode in all layers ($x_{an,*}$).

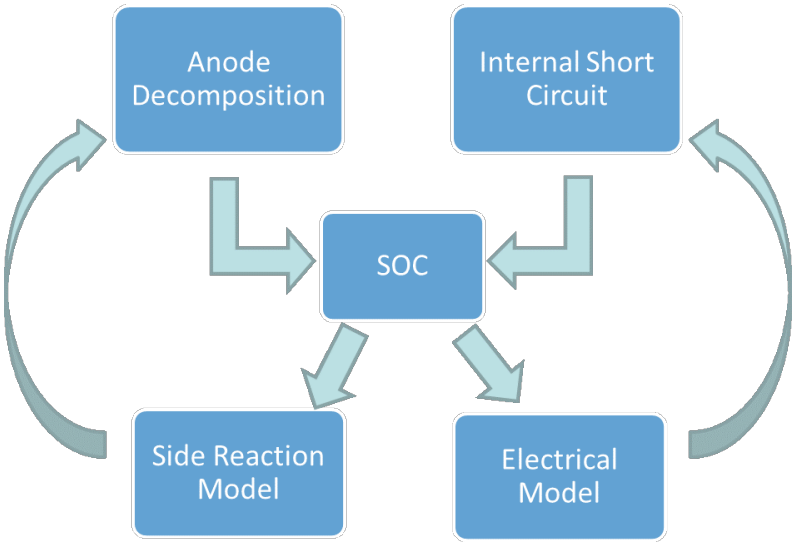

Figure 2.4: Charge depletion through ISC and anode decomposition

$$SOC = \sum_{*} \frac{m_*}{m_{cell}} \frac{x_{an,*}}{x_{an,0}} \tag{2.26}$$

where $x_{an,0}$ is the initial Li fraction in an anode for fully charged cells. Then anode decomposition and SOC change of a cell with capacity C can be re-written as:

$$\begin{aligned} \frac{dSOC}{dt} = -\frac{I_{short}}{C} - \frac{1}{x_{an,0}} \sum_{*} \frac{m_*}{m_{cell}} A_{an} \cdot x_{an,*} \\ \cdot \exp\left(-\frac{E_{an}}{k_b T_*}\right) \cdot \exp\left(-\frac{z_*}{z_0}\right) \end{aligned} \tag{2.27}$$

where * here represents core, middle layer or surface layer, and $x_{an,*}$ represent local x_{an} in core, middle layer or surface layer. Assuming that I_{short} depletes lithium

in all sections proportionally, then the fraction of lithium in each section is computed by:

$$\frac{dx_{an,*}}{dt} = -A_{an} \cdot x_{an,*} \cdot \exp\left(-\frac{E_{an}}{k_b T_*}\right) \cdot \exp\left(-\frac{z_*}{z_0}\right) - x_{an,0}\frac{I_{short}}{C} \tag{2.28}$$

instead of solving Eq. 2.21, where T_* is the local temperature for core, middle and surface layer.

2.2.5 Gas Evolution Model

Previous studies have assumed the main component of SEI is $(CH_2OCO_2Li)_2$ [6]. They showed the SEI decomposition reaction mechanism, which will release CO_2 [6, 45].

$$(CH_2OCO_2Li)_2 \rightarrow Li_2CO_3 + C_2H_4 + CO_2 + 0.5O_2$$

Experiments on commercial 18650 Li-ion batteries from Lammer et al. [37] showed that during the first venting, most of the gas is CO_2. Based on these results, we assume that CO_2 is the main component of vented gas and it causes the gas pressure build-up process inside the cell before venting. Our study only models the initial gas generation of CO_2 coming from SEI decomposition which is important for early indication of a potential thermal runaway. The quantity of SEI consumed in mol can be expressed as:

$$n_{(CH_2OCO_2Li)_2} = \frac{\sum_* m_{an,*}(x_{SEI,0} - x_{SEI,*})}{2M_{C_6}} \tag{2.29}$$

where M_{C_6} is the mass per mol (g/mol) for C_6, the main component of anode when completed delithiated, and $n_{(CH_2OCO_2Li)_2}$ is the quantity of lithium-containing metastable species in SEI consumed in the reaction in mol. Since the SEI decomposition reaction mechanism shows the proportional constant for generated CO_2 and the consumed SEI quantity is 1, then the quantity of gas generated in mol can be expressed as:

$$n_{CO_2} = n_{(CH_2OCO_2Li)_2} = \frac{\sum_* m_{an,*}(x_{SEI,0} - x_{SEI,*})}{2M_{C_6}} \tag{2.30}$$

Hence the thermal model can be used to predict the gas pressure using the ideal

gas law. As n_{CO_2} is a small number, for convenience, n_{CO_2} will be shown in mmol units in following discussions.

The gas evolution model can be used to predict battery force changes during the early stage of a thermal runaway if volume is known. During the early stages of thermal runaway, the cell's mechanical behavior is mainly due to the increased internal gas pressure within the cell. The force and gas pressure have different units, but the gas pressure can be used to predict the overall trend of cell mechanical behavior.

2.3 Internal Short Circuit Experimental Setup

The batteries used in this experiment were manufactured at the University of Michigan Battery Lab. The pouch cell size is 133 $mm \times 89$ $mm \times 4$ mm. As shown in Figure 2.5a, a thermal runaway experiment using a 4.5 Ah Nickel Manganese Cobalt Oxide (NMC) pouch cell was set up to validate the model. The pouch cell was assembled with a hole in the separator covered by wax in one of the outer layers of the cell, the hole size being around 10 mm radius. The 1 kHz impedance of cell, from EIS testing, was 4.76 $m\Omega$ at 20°C. The experiment was performed for two pouch cells, one with 50% SOC and the other cell was fully charged (100% SOC). The battery specifications are provided in Appendix in Table. A.1.

The instrumented cell fixture was slowly heated in an Accelerating Rate Calorimeter (ARC) until the wax melted at around 57 °C, and triggering an internal short circuit. The ambient temperature was measured with a T-type thermocouple. The thermocouple was placed between the current collecting tabs, and the reading was 63 °C before the thermal runaway event. The whole ARC chamber was continuously heated at around 0.7 °C/min and reached 63 °C before the onset of the internal short circuit event. When the core part in the pouch cell reached its melting point (around 57 °C) it triggered the ISC. A sketch of the sectional view of pouch cell tested is shown in Fig. 2.5b, to better illustrate the location and size of initial ISC area.

The experiment measures battery surface temperature using an array with six thin film platinum RTD sensors [46], as shown in Fig. 2.5a and Fig. 2.5b. At the same time, force is measured on the fixture using four load washers attached to the four corners of the fixture. The force signal is used to measure the expansion of the battery against the fixture. The peak force measured exceeds 1800 N and is the result of gas pressure that built up inside the pouch during thermal runaway before cell venting. The ISC location and sensor locations are shown in Figure 2.5a and Figure 2.5b. Further details of the experiment are in Pannala's work [47] and more

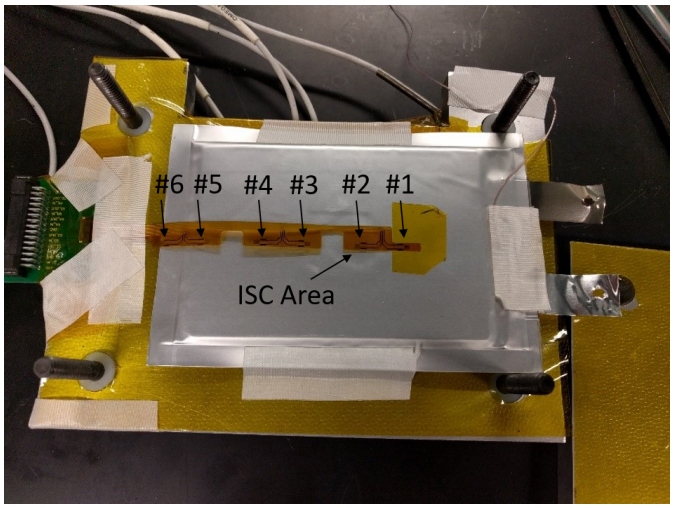

(a)

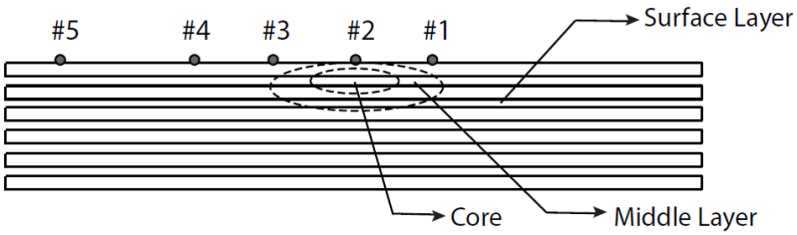

(b)

(c)

Figure 2.5: Experiment setup (a) Cell before internal short test. (b) Sensor locations from sectional view. (c) Cell after thermal runaway.

details of the pouchcell can be found in Appendix.

2.4 Result and Analysis

Table 2.1: Model parameters

Parameter	Value	Unit	Source	Physical Meaning
A_{an}	2.5×10^{13}	s^{-1}	[32, 42]	Frequency factor for anode decomposition
A_{ca}	2.55×10^{14}	s^{-1}	[42]	Frequency factor for cathode decomposition
A_{SEI}	2.25×10^{15}	s^{-1}	[42]	Frequency factor for SEI decomposition
A_{c2m}	628	mm^2	Approximated	Contact area for core to middle layer
A_{m2s}	1711	mm^2	Approximated	Contact area for middle layer to surface
C	4.5	Ah	Measured	Capacity of the Battery
C_p	1100	$J\ kg^{-1}\ K^{-1}$	[22]	Specific heat capacity of battery core
$C_{p,Al}$	897	$J\ kg^{-1}\ K^{-1}$	Approximated	Specific heat capacity of aluminum fixture
Δd_{c2m}	1	mm	Approximated	Core to middle layer mass center vertical distance
Δd_{m2s}	1.38	mm	Approximated	Middle layer to surface mass center vertical distance
E_{an}	2.24×10^{-19}	J	[32, 42]	Activation energy for anode decomposition
E_{ca}	2.64×10^{-19}	J	[42]	Activation energy for cathode decomposition
E_{SEI}	2.24×10^{-19}	J	[32, 42]	Activation energy for SEI decomposition
h_{an}	1714	$J\ g^{-1}$	[32, 42]	Enthalpy of anode decomposition
h_{ca}	790	$J\ g^{-1}$	[42]	Enthalpy of cathode decomposition
h_{SEI}	257	$J\ g^{-1}$	[32, 42]	Enthalpy of SEI decomposition
m_{an}	19.107	g	Measured	Mass of anode
m_{ca}	36.56	g	Measured	Mass of cathode
m_{cell}	103.75	g	Measured	Total mass of cell
m_{core}	1.038	g	Fitted	Mass of battery core
m_{fix}	1100	g	Measured	Mass of Aluminum fixture
m_{mid}	4.67	g	Fitted	Mass of battery middle layer
m_{surf}	98.04	g	Estimated∗	Mass of battery surface layer
r_{c2m}	3.18	$K \cdot W^{-1}$	Estimated∗	Thermal resistance between core and middle layer
r_{m2s}	1.61	$K \cdot W^{-1}$	Estimated∗	Thermal resistance between middle layer and surface
r_{s2a}	1.00	$K \cdot W^{-1}$	Estimated	Thermal resistance between surface layer and fixture
r_{fix}	1.73	$K \cdot W^{-1}$	Estimated	Thermal resistance between fixture and ambient air
R_{1kHz}	4.76	$m\Omega$	Measured	1 kHz cell impedance at 20°C
$R_{e,ref}$	0.0246	$m\Omega$	Approximated	Reference electrical resistance
R_{short}	3.68	$m\Omega$	Estimated∗	Short circuit resistance
SOC_0	1	-	Approximated	Initial State of Charge
T_{amb}	63	°C	Measured	Ambient temperature
T_{ref}	1543	K	[41]	Reference temperature
$x_{an,0}$	0.75	-	[32, 42]	Initial fraction of Li in anode for fully charged cells
$x_{SEI,0}$	0.15	-	[32, 42]	Initial fraction of Li in SEI
z_0	0.033	-	[32, 42]	Initial dimensionless SEI thickness
α_0	0.04	-	[32, 42]	Initial degree of conversion of cathode decomposition

∗Thermal resistance r_{c2m}, r_{m2s} are estimated by Eq. 2.31.

∗R_{short} is estimated by Eq. 2.12.

∗m_{surf} is estimated by conservation of mass ($m_{core} + m_{mid} + m_{surf} = m_{cell}$).

The model is compared with the two internal short circuit test results — Test One for the 100% SOC cell, Test Two for the 50% SOC cell. The cell with 50% SOC didn't go to thermal runaway, and instead experienced a slow self-discharge. The fully charged cell experienced a quick thermal runaway, as shown in Fig. 2.5c.

Before further discussing the experiment and comparing our model and the experimental results, a few assumptions have been made for the model. First, the relative volumes of the core and middle layer are tuned to match the experimental data. The

core mass used for our simulation is chosen to be 1% of total mass to match the duration of internal short circuit for 50% SOC cell. The middle layer is 4.5% of total battery mass based on a minimum least square error of the model and experimental surface temperature measured by sensor #5 in Fig. 2.5a .

The hole in the separator is around 10 mm in radius, and from previous discussion of ISC resistance, Eq. 2.12 can be used to estimate the short circuit resistance. The estimated R_{short} for this pouch cell is $3.68m\Omega$.

The equivalent thermal resistance can be calculated using cell heat conductivity ($\lambda_x = 21\ W/(m \cdot K), \lambda_y = 21\ W/(m \cdot K), \lambda_z = 0.5\ W/(m \cdot K)$ [22]) and geometry of the three regions. As the shape of the pouch cell is long and flat, we can roughly approximate the thermal resistance by the following equation:

$$r_i = \frac{\Delta d_i}{\lambda_z A_i}\ (i = c2m, m2s) \tag{2.31}$$

where r_i is the thermal resistance for core to middle, or middle to surface, Δd_i is the vertical distance between the mass center of the core to middle layer, or the middle layer to surface layer, and A_i is the contact area in the x and y plane for core to middle, or middle to surface layer. In calculating thermal resistance, we assume the core and middle layer to be cylinders. For the core, we roughly assume it as a cylinder with 10 mm radius (the ISC radius) and 1.51 mm height, which will correspond to 1% core volume ratio. For the middle layer, which will correspond to 4.5% middle layer volume ratio, we assume its radius and height is proportional to the core, so it is a cylinder with 16.5 mm radius and 2.5 mm height. Based on these assumptions, Δd_i and A_i will be calculated and provided in Table 2.1 that are used to calculate r_{c2m} and r_{m2s}.

The melting point of Aluminum is 660 °C, and around 1000 °C for Copper, so the current collector will melt and at that point the battery structure collapses. We can then assume that the internal short circuit will stop at sections with temperatures above 660 °C. As the heat propagates to neighboring areas, an internal short starts in the neighbouring areas after that collapse.

In addition, the experiment setup contains a compliant rubber foam pad and an aluminum fixture, which should be considered in the model to accurately represent the heat transfer to the ambient environment. The equivalent thermal resistance r_{s2a} now represents the thermal resistance between the battery surface and the aluminum fixture, so that the T_{amb} term in Eq. 2.3 will now be T_{fix}. The aluminum fixture is not an ideal heat sink, in this case, the temperature rise of the fixture can be expressed

as:

$$C_{p,Al} \cdot m_{fix} \frac{dT_{fix}}{dt} = \frac{T_{surf} - T_{fix}}{r_{s2a}} + \frac{T_{amb} - T_{fix}}{r_{fix}} \tag{2.32}$$

where thermal resistance terms r_{s2a} and r_{fix} are correlated with the rubber foam properties and heat transfer process from air to fixture. For convenience, these two thermal resistance terms will be given in Table 2.1 directly. Other model parameters for the fully charged cell are also presented in Table 2.1. The parameters come from existing literature, direct measurement, fitting, approximation, or estimation based on the equations in this study. The comparison between experiment result and model prediction for both tests will be shown in the following.

2.4.1 Test One: Fully Charged Cell

The first experiment was performed with a cell at 100% SOC, and it resulted in a thermal runaway. The behavior of fast voltage drop without recovering is also described in previous studies[48], except in this case a quick thermal runaway event was triggered. As described by Feng [6], the shrinkage and collapse of the separator following the shutdown caused a massive ISC, triggering a quick thermal runaway in the tested battery cell. The model assumes that for the fully charged cell, the propagation of ohmic heat leads to additional short-circuit regions after the initial short circuit area burns out [48].

A function ϵ_{ISC_t1} is implemented here to control the state of ISC of Test One. $\epsilon_{ISC\_t1} = 0$ represents no massive ISC, while $\epsilon_{ISC\_t1} = 1$ represents an ongoing ISC in the cell.ϵ_{ISC_t1} is a function of maximum core temperature recorded in the model before time t_0, defined as $T_{max} = max\{T_{core}|_{t \leq t_0}\}$, and can be expressed as:

$$\epsilon_{ISC\_t1} = \begin{cases} 1, & \text{if } T_{max} > 57\ ^{\circ}C. \\ 0, & \text{otherwise.} \end{cases} \tag{2.33}$$

The Test One result is shown in Fig. 2.6. The solid line shows the experimental result, and the dashed line is the model prediction. The side reaction parameters and SOC predicted by the model are shown in Fig. 2.7.

2.4.1.1 Voltage Analysis

The voltage drop at t=2.1s in Fig. 2.6 represents the start of the internal short circuit event. When voltage drops to zero, the ohmic heat generation stops. The

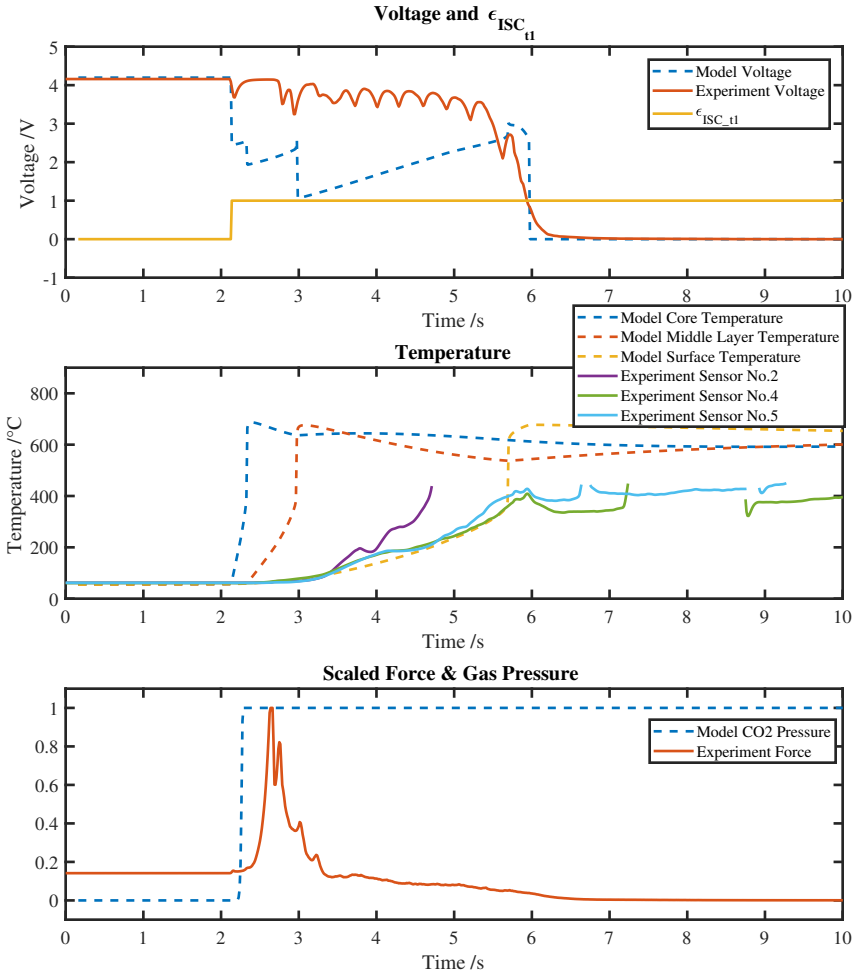

Figure 2.6: Test one result (catastrophic thermal runaway). (a) The timings of the voltage drop and temperature rise with battery internal pressure build-up are well captured by the model.

oscillation in the measured voltage is the result of the intermittent connection of the ISC due to structural changes at high temperature, and this voltage behavior is not captured by the model. The model predicts a stepwise voltage drop because we assume the ISC area will expand to the neighboring area, and as discussed above, the larger ISC area will decrease the R_{short}, and decrease the terminal voltage. The model voltage increases at 3 to 5 seconds, and this is due to R_{cell} decrease with temperature rise, while the R_{short} stays constant with temperature change.

To be noticed, voltage is also a function of SOC. However, the SOC-voltage curve is relatively flat, as seen in 2.2b. The influence of the SOC change in voltage is

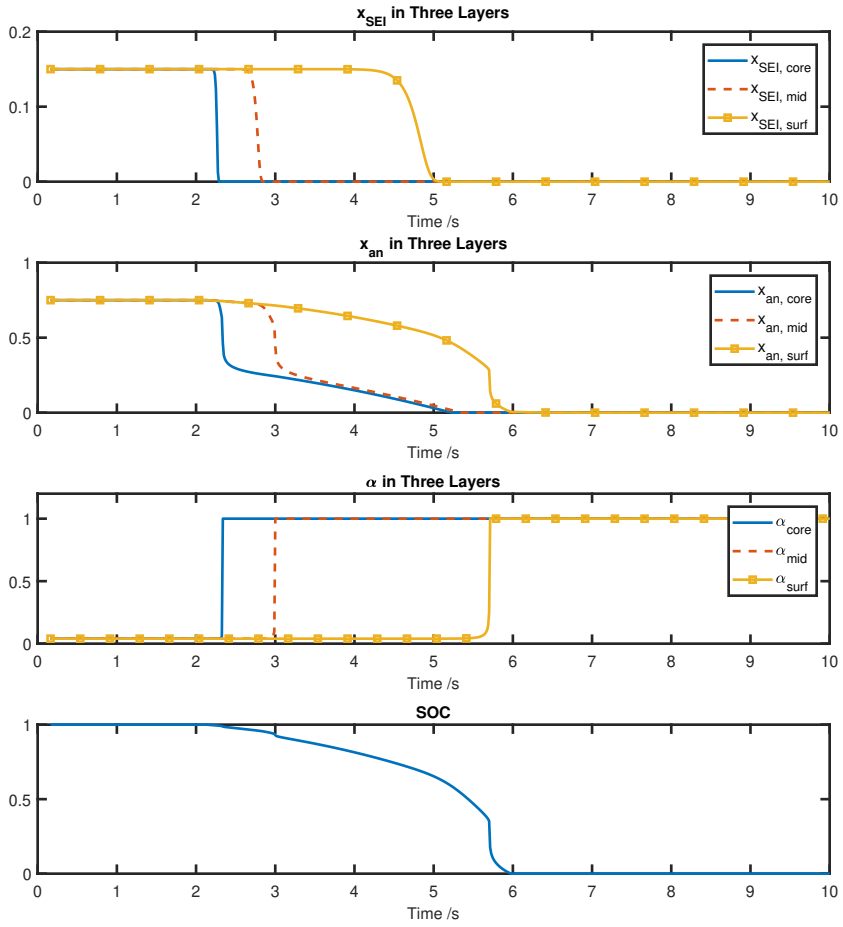

Figure 2.7: Test one result (catastrophic thermal runaway). (b) Side reaction parameters show the side reactions sequence during a thermal runaway

relatively small in this thermal runaway event. On the overall time scale, the model fits with experiment data and predicts total battery failure at approximately the same time as the experiment.

2.4.1.2 Temperature Analysis

The RTD sensors are located in different regions of the pouch cell, as seen in Figure 2.5a. The ISC trigger device is located near the surface, as described by Pannala [47]. As seen from the sensor locations of Fig 2.5b, the RTD sensor #2 corresponds to the surface layer in the model but is physically located directly above the ISC area. RTD sensor #1, #3 and #4 measure the temperatures at the surface, each

RTD sensor is spaced 1.75 mm apart [46], RTD sensor #5 measures the temperature of the bulk surface.

The second subplot in figure 2.6 shows the comparison of model and experimental temperatures. The experimental data above 450 °C has been ignored, because the melting point of Kapton used in RTD sensor is 400 °C. The readings from RTD sensor #1 and #2 are very similar due to their close proximity, the same for RTD sensor #3 and #4. RTD sensor #6 was damaged prior to installation, and could not be used. For readability, only data from sensor #2,#4 and #5 will be presented and analyzed.

The RTD sensor #2 is at the surface layer of the battery model, but it is located above the middle layer and core part, so its response should be close to our modeled middle layer temperatures. The experimental data from RTD sensor #2 (the purple solid line in the plot) is in between the modeled middle layer temperature (dashed red line) and the modeled surface temperature (dashed yellow line), and this is due to the small middle layer chosen in this study, so the RTD sensor #2 response will be slower than the modeled middle layer temperature. RTD sensor #4 (green solid line) and #5 (blue solid line) measure the surface temperature and match well with the modeled surface layer temperature.

With proper tuning on the mass of middle layer, the model can match with the temperature measured experimentally, which indicates that this pouch cell ISC event can be modeled using the proposed three section model. However, a highly discretized distributed model or 3D finite element method is recommended if the temperature at different points of the cell surface is the main focus.

At around 5.8 seconds, the model predicts a sudden surface temperature rise. This sudden rise is due to cathode decomposition in the surface layer which released a vast amount of energy in a short time around 5.8 seconds, as shown in Fig. 2.7. The sudden rise of surface temperature also increased other exothermic reactions including anode decomposition, which depleted SOC in the cell. At 5.8 seconds, the cell reached peak surface temperature, and it completed the exothermic reactions and internal short circuit process in this thermal runaway event.

2.4.1.3 Force and Gas Analysis

As there is no good way of measuring battery core temperature directly in the experiment, the force measurement is the chosen alternative for early detection of thermal runaway inside the battery.

From the experimental data we see a sharp rise and drop of force measurement. Compared with the battery force signal at the start of experiment, the force increased

11.1 N due to battery thermal expansion caused by a 30°C temperature increase. After the short circuit, before venting, the peak force rose over 1800 N. The sharp rise of force is the result of pressure that is built up due to formed gas. Pannala[47] using a thermocouple placed between the tabs, also detected vented hot gases following a quick drop of force. So the quick drop of force is the result of venting of the pouch.

In the model, the primary source of CO_2 during the early stage of thermal runaway is assumed to come from SEI breakdown. The model predicted force comes from gas pressure build-up due to SEI breakdown in the core section.

According to the observed decomposition reactions of each layer in the three-section model, the predicted gas generation will include additive contributions from each of three sections, core, middle layer, and surface layer. A significant amount of gas is generated when the middle layer and surface layer reach the critical temperature. However, since the pouch breaks soon after the first stage gas pressure build-up, only the CO_2 generated in core section is presented in the third subplot of Fig. 2.6. Also, since the force measurement and gas pressure have different scale units, so the force data and gas pressure are both normalized to 1 using the maximum value over the experiment duration.

From the third subplot of Fig. 2.6, the two peaks of force and predicted gas pressure align well. The model successfully predicts the battery core temperature rise prior to surface temperature rise, and the timing of core temperature rise matches well with our experimental force measurement. The model is therefore able to predict the feature of gas pressure build-up during a fast internal short circuit event.

2.4.2 Test Two: Half Charged Cell

For the half charged cell (50% SOC), which was also heated to 57 °C, an ISC was triggered but didn't evolve into a catastrophic thermal runaway. In Test Two, the cell experienced a rapid decrease and subsequent recovery of voltage after the ISC was triggered. It then progressed to a slow self-discharge process that completely used up the available lithium ions after 8000 seconds. Fig. 2.8 shows this behavior in our experiment over 10000 seconds. This behavior is similar to the result in previous study on internal short-circuit [48] or described as fusing phenomenon [23]. In the fusing phenomenon, the shutdown of the internal short circuit and the quick voltage recovery happen because of the burnt-out of the area around the initial ISC. Then a following small-scale ISC event occurs resulting in a slow self-discharge process [23].

Kim [48] used an infrared camera and showed the peak temperature for the nail penetration region in a short circuit fusing phenomenon is around 200 °C to 210

°C. In the current model, 200 °C will be used as the critical temperature of fusing phenomenon. The ISC stops after the core region reaches 200 °C. This temperature range fits well with both experimental and model data in this study.

For Test Two, the internal short circuit was assumed to shut down when the core temperature reached 200°C. Similar to Test One, a function ϵ_{ISC_t2} is implemented here to control the state of ISC of Test Two. $\epsilon_{ISC\_t2} = 0$ represents no massive ISC, while $\epsilon_{ISC\_t2} = 1$ represents an ongoing ISC in the cell. Defined same as test one, $T_{max} = max\{T_{core}|_{t \leq t_0}\}$. ϵ_{ISC_t2} is a function of T_{max}, and can be expressed as:

$$\epsilon_{ISC\_t2} = \begin{cases} 1, & \text{if } T_{max} > 57\ ^{\circ}C\ \&\ T_{max} \leq 200\ ^{\circ}C. \\ 0, & \text{otherwise.} \end{cases} \tag{2.34}$$

Test Two result is shown in Fig. 2.9. The solid line represents the experiment results, and the dashed line is the model prediction. The side reaction parameters predicted by the model are given in Fig. 2.10.

2.4.2.1 Voltage Analysis

The first subplot of Fig. 2.9 is a comparison of voltage from the experiment and model. The voltage drop at t=2.65 s represents the start of the internal short circuit event. With the use of ϵ_{ISC_t2} to control the ISC state, the model fits with experimental data on the timescale and overall trend. It also shows the shutdown of ISC and the voltage recovering.

2.4.2.2 Temperature Analysis

Temperature sensor locations for Test Two are the same for Test One. In this test, the cell didn't trigger a quick thermal runaway.

As the core temperature reached 200 °C, the ISC is assumed to stop due to burnout of the short circuit region, so the ISC process only lasted for a small period of time and caused core layer temperature rise only. In this short circuit test without a thermal runaway, RTD sensors located on the battery surface showed almost constant temperature during the ISC process. Specifically, after 5 seconds of the ISC event, the measured surface temperature increased only 1 °C. The model prediction matches well with the measured temperature on the battery surface, and at the same time predicts core temperature rise (blue dashed line), which cannot be measured by RTD sensors in the experiment.

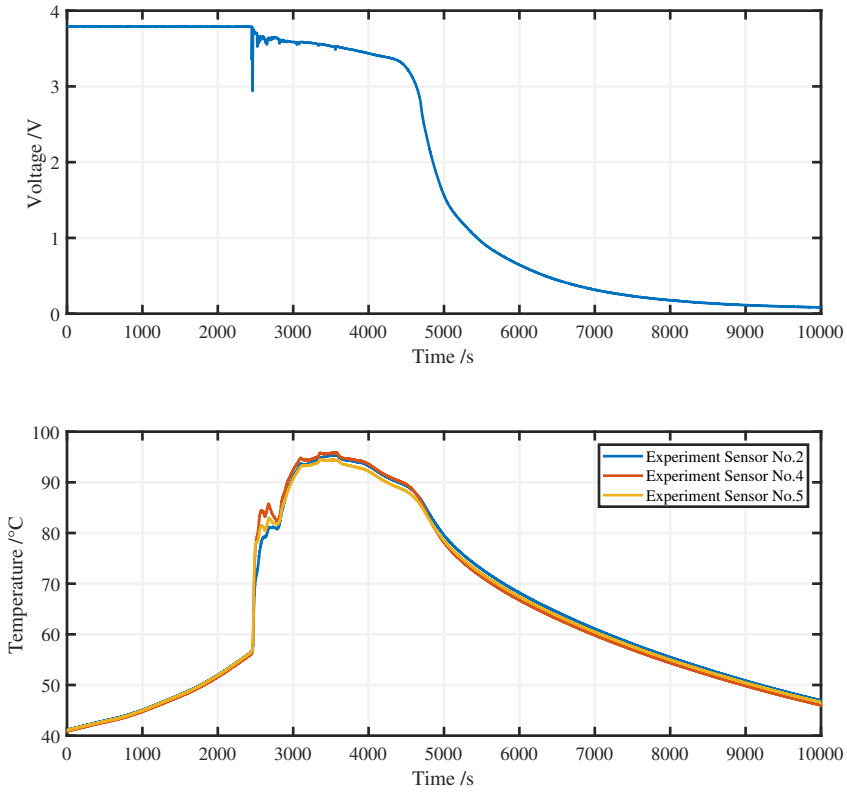

Figure 2.8: Test two result (slow self-discharge). (a) The terminal voltage and temperature profile of 50% SOC cell from experiment over 10000 seconds. No thermal runaway was observed, but a slow self-discharge process after triggering ISC.

2.4.2.3 Force and Gas Analysis

Similar to Test One, the force measurement can be used to detect potential ISC within the cell. From the third subplot of Fig. 2.9 for Test Two, the time for the peak of measured expansion force and the predicted gas pressure rise time align well. With the use of ϵ_{ISC_t2} to control the ISC state, the model predicts the battery core temperature rise, and while at the same time shows that the battery didn't progress into a quick thermal runaway.

2.4.3 Analysis for Different ISC Modes

Both Test One and Test Two were conducted under the same conditions, except for cell SOC but each progressed to a different ISC event. The fully charged cell went into thermal runaway while the 50% SOC cell experienced fusing phenomenon and didn't explode. However, SOC is not the only factor in determining the ISC mode.

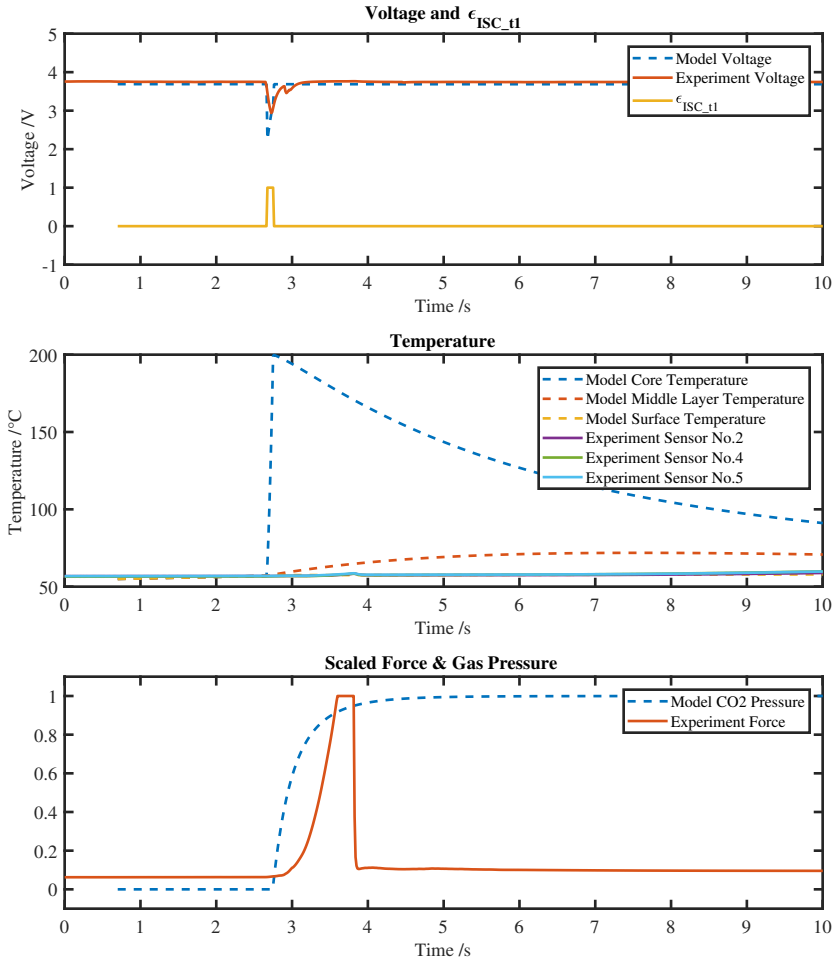

Figure 2.9: Test two result (slow self-discharge). (b) The model matches the measured voltage, temperature, and build-up of internal pressure well

Previous nail penetration experiments and computational analysis pointed out that SOC, separator material [48] and ISC radius [23] will all affect the types of ISC mode.

It is possible that the temperature increase speed for core and neighboring layers is the dominant factor for ISC mode. Unlike the fully charged cell, the 50% SOC cell had a slower temperature rise and a smaller spatial temperature gradient, which in the end didn't trigger a massive additional short circuit that can lead to a catastrophic thermal runaway.

In this study, different model settings of ISC modes are given for Test one and Test two to describe the results. At this stage, this model cannot predict the modes of an ISC event. However, future work with more internal short circuit tests is required to

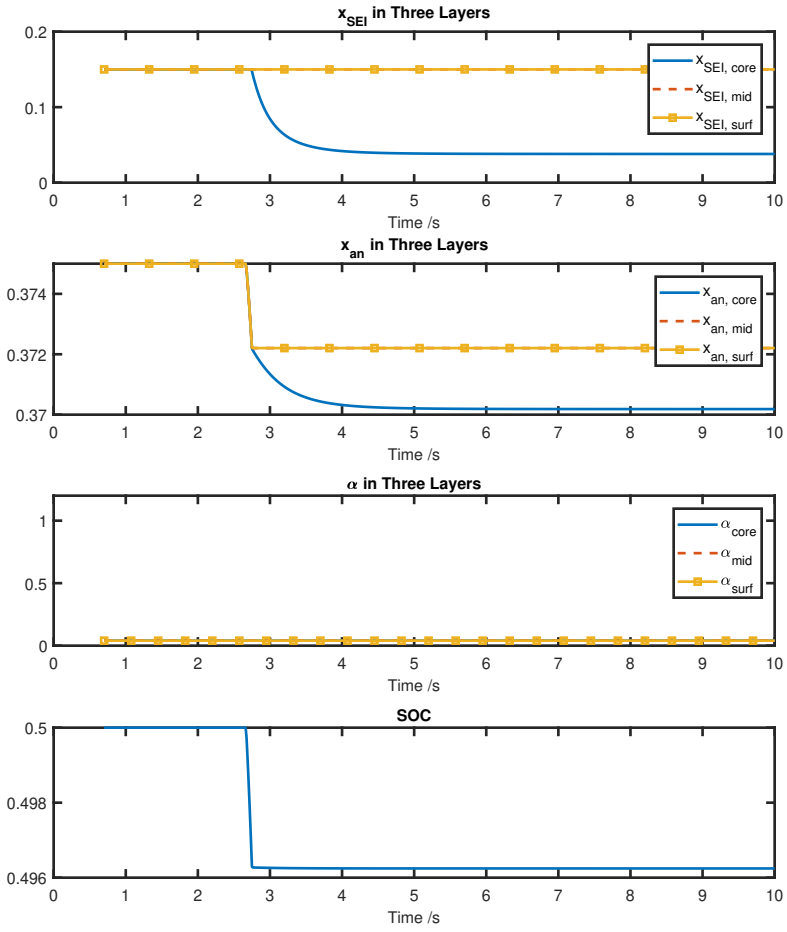

Figure 2.10: Test two result (slow self-discharge). (c) Side reaction parameters show the SEI decomposition is the only active side reaction

study the criteria to predict whether the cell triggers thermal runaway or not during an ISC event.

2.5 Model Parametric Study

Most of the parameters in the proposed model come from the battery's physical properties. In this study, with the ISC area known, parameters like ISC resistance can be estimated. However, when applying this model to a real case, the ISC resistance and ratio of core mass to total cell mass are usually unknown and need to be tuned to match the experimental data. A parametric study of the thermal runaway model will help to explore the sensitivity of parameters on the model. In this parametric

study, ISC resistance, core mass ratio and ISC radius will be studied.

For a parametric study of ISC radius, anode to cathode ISC will be the focus, as anode to cathode ISC is the most common type of ISC [25]. In such a case, changes made to the ISC radius will be applied to both ISC resistance and core mass ratio. As discussed in previous sections, ISC resistance is a function of ISC radius, and the increase of ISC radius will decrease ISC resistance as a result of the larger ISC area. The core mass ratio is also a function of ISC radius. The core section is the battery area affected by the initial ISC, and as expressed by Eq. 2.4: $V_{core} = \pi r_{short}^2 H$, where r_{short} is the radius of short, and H is the height of cylindrical short area. The increase of ISC radius will increase the core mass. The parameters used in experimental sessions will serve as a benchmark case for our model parametric study, with ISC resistance 3.68 $m\Omega$, core mass ratio 1%, and ISC radius of 10 mm.

2.5.1 ISC Resistance

In this section, ISC resistance will be changed to study the influence of model parameters on the prediction of the electrical, thermal and mechanical behavior. Feng [22] used $R_{short} = 20\ \Omega$ to study the online detection of ISC. For comparison, ISC resistance will be chosen 5 Ω in this parametric study, while the benchmark ISC resistance is 3.68 $m\Omega$.

The second subplot for Fig. 2.11 and red dashed line in Fig. 2.12 shows the temperature and voltage predicted by the model given different ISC resistances. From the plot, we see the temperature rise of a cell with low ISC resistance is much quicker, and depletes its active material in less than 10 seconds. The cell with high ISC resistance releases the heat slowly, and won't trigger a thermal runaway event. Increasing the resistance will slow the ISC process and possibly prevent a potential thermal runaway event.

Large ISC resistance will have a slow temperature rise, and usually represents micro-shorts in the battery or separator penetrated by a low electric conductivity material. The parametric study of this model can be used to predict the severity of an ISC event, and based on its short circuit radius, it may predict whether the cell will trigger thermal runaway or not.

Fig. 2.13 shows the amount of CO_2 generated by core SEI decomposition. With ISC resistance so large, the core area will not reach its SEI decomposition critical temperature, even after a few minutes. In this case, the amount of gas generated is limited and can hardly be detected by force or gas sensors.

2.5.2 Core Mass Ratio

In this section, we demonstrate the effect of changing the core layer mass ratio. The core layer mass ratio is chosen to be 20% of total cell mass, while the benchmark core mass ratio is 1%.

The third subplot for Fig. 2.11 and yellow dashed line in Fig. 2.12 shows the temperature and voltage predicted by the model given different core mass ratios. From the plot, we see that with high core mass ratio, the time to reach thermal runaway has been delayed. This is due to the increased effective thermal mass of the core area which decreases the rate of temperature rise and delays the time at which a critical temperature for exothermic reactions is achieved.

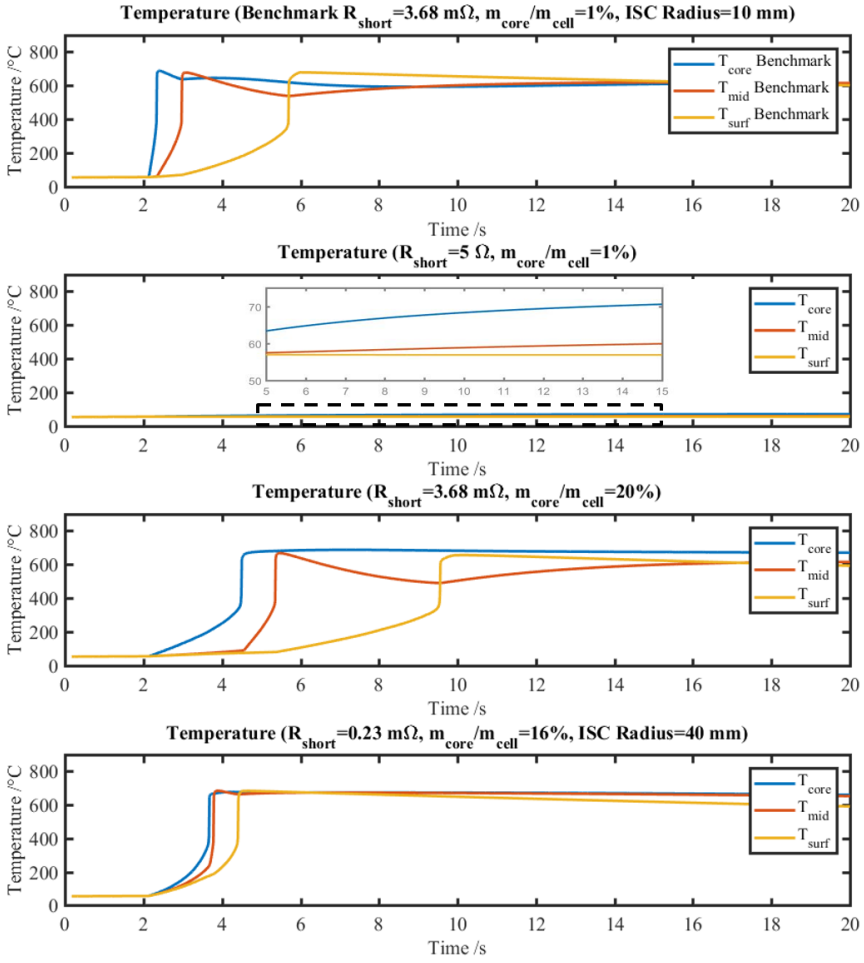

Figure 2.11: Model parametric study on ISC resistance, core mass ratio and ISC radius. (a) Temperature

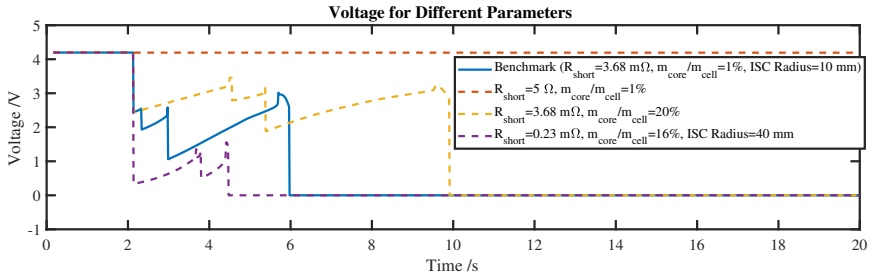

Figure 2.12: Model parametric study on ISC resistance, core mass ratio and ISC radius. (b) Voltage

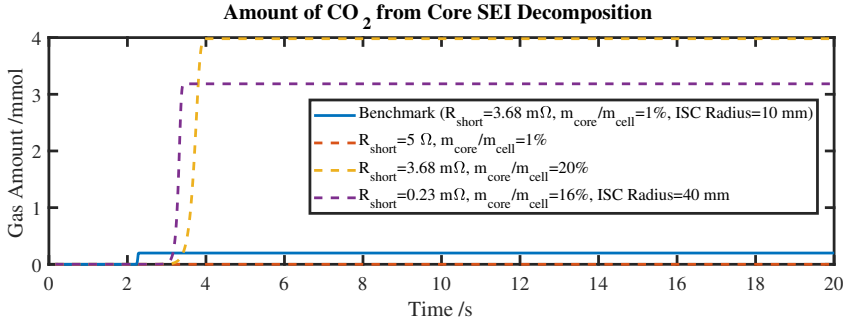

Figure 2.13: Model parametric study on ISC resistance, core mass ratio and ISC radius. (c) CO_2 generation by SEI decomposition in core area

2.5.3 ISC Radius

Previous parametric studies have revealed the influence of critical ISC parameters on model performance. For the most common Cathode to Anode ISC, with high conductivity material crossing the separator, core mass ratio and ISC resistance are both a function of ISC area, as indicated by Eq. 2.4 and Eq. 2.12. Changes in ISC area will influence the ISC resistance and core mass ratio.

In this study, the ISC radius is chosen as 40 mm, while the benchmark is 10 mm. From the previous discussion of section 2, for ISC radius of 10mm and 40mm, the geometric resistance (R_{geo}) is sufficient for calculation. The resulting electric resistances are 3.68 $m\Omega$ and 0.23 $m\Omega$, respectively. The core mass ratio for our benchmark is 1%, and with the ISC radius increase to 40 mm, the core mass ratio will now increase from 1% to 16%. The increased mass ratio reflects the increased ISC area. The thermal resistance term r_{c2m} also changes accordingly with the change of contact area for core to middle layer by Eq. 2.31. The simulation results with the different ISC radius are presented in the fourth subplot of Fig. 2.11 and Fig. 2.12.

From the plot, we see that for Cathode to Anode ISC, at large ISC radius, the temperature distribution in the battery is more uniform. The difference between the three temperature states is small throughout the whole process of thermal runaway. A large ISC radius will make the ISC process seem to approach an external short circuit process. In this specific condition, the three-state thermal model predicts similar temperature dynamics as a lumped thermal model, and a lumped model would be accurate enough.

2.6 Summary

A model for Li-ion battery thermal runaway has been formulated using a three section discretization. The three sections correspond to three battery temperature states: the core temperature, middle layer temperature, and surface layer temperature. A side reaction model, an electrical model, a gas evolution model are also developed. The predicted gas pressure from the gas evolution model can be used to predict battery force during the early stage of thermal runaway. This force behavior indicates a potential method for early detection of thermal runaway. In this study, the prediction of gas pressure from the model is also compared with measured force behavior from experiments.

In the experiment, an internal short circuit is triggered at the core part of two pouch cells. Test One cell with 100% SOC triggered a quick thermal runaway, while the other test cell, with 50% SOC, didn't go to thermal runaway. With proper tuning, the model can match the experimental voltage, temperature, and force for both cases when given the type of ISC modes. Although proper tuning is required for this model to match the data, we have shown the potential of the proposed three-section model to describe the complicated behavior of both an ISC induced thermal runaway event as well as an ISC fusing phenomenon without a thermal runaway.

The significant difference between our two tests is whether the ISC shuts down or leads to additional ISC after the burn-out of the initial ISC. This difference leads to two different results, a catastrophic thermal runaway or a safe, slow self-discharge process. This model cannot predict the ISC modes and future work including more internal short circuit experiments is needed to study the criteria that differentiate such cases. With more experiments to validate this model, it will allow further prediction of the ISC mode based on cell parameters and short circuit areas, to predict whether the cell will go to thermal runaway or not.

The model bridges the connection between the expansion force increase with the

gas evolution model at the early stage of an ISC event, and demonstrates the potential of using expansion force measurement for identifying ISC events through modeling work and experiments. With this measurement, higher confidence levels detection can be achieved compared to voltage and temperature sensing alone.

CHAPTER III

Internal Short Circuit Detection Using Force Measurement

3.1 Introduction

Many of the Li-ion battery accidents started with an overcharge, overheat, mechanical abuse [6] or lithium plating that leads to battery internal short circuit (ISC). Joule heating, caused by an ISC event, can elevate the battery temperature to thermal runaway critical temperature [43]. Detection of an ISC event should be made early to avoid further damages.

On the other hand, false positives for ISC detection are also undesirable as many thermal runaway mitigation techniques, such as activating pyrotechnic safety switches, would disable the vehicle. Therefore, high confidence level detection with fast response to ISC events is required.

Previous methods of detecting ISC are usually based on voltage measurement. Since battery abuse testing usually shows a significant battery voltage drop after the cell failure [23, 26]. Xia [49] proposed a fault-tolerant method that can distinguish between cell failure and voltage sensor failure. The fault detection can be model-free with correlation coefficient calculated for neighboring cells in series [50]. The model also features fast detection speed, as the voltage drop is almost instantaneous after an ISC [25].

Other methods of ISC detection using surface temperature measurements can be found in [21, 22, 51]. These fault detection methods work well with soft ISC, where the temperature gradient inside the cell is not huge. For hard ISC, the battery's internal temperature can be elevated in a few seconds, causing a huge temperature gradient inside the cell. Prior works divided the battery into three temperature sections [35, 52], and showing that at the early stage of ISC, the battery ISC region

has a higher temperature. Surface temperature rise for such event is slower than voltage drop and expansion force rise.

In this chapter, we develop an ISC detection method based on expansion force measurement. In a hard internal short event, high temperature and battery side reactions in the ISC region will produce a large amount of gas. This leads to a quick cell swelling and a sudden increase of expansion force [52]. In the proposed algorithm, we build an observer for the cell expansion force in normal operating conditions. The observer value is compared with online force measurement. An alarm will be triggered when the deviation of the observer value and the measurement exceeds the adaptive threshold. For higher confidence level detection, we also use voltage signals to detect abnormal voltage behaviors. The simulation results for a single cell demonstrate the effectiveness of the proposed algorithm in detecting a hard ISC event.

3.2 Limitation of Temperature Based Detection

During normal operating conditions, there exists temperature gradient in the battery core and surface [41]. In an ISC event, the temperature gradient will be larger due to the higher local rate of heat release which results in a fast temperature increase of cell core region [52]. The ISC happens at battery core regions first, and it takes time for the battery surface to heat up. The following analysis for battery surface temperature measurement shows that the temperature detection method has its limitation in estimating ISC core temperature.

The battery cell can be divided into three regions, core, middle layer and surface layer [52]. The thermal model can be written as

$$C_p m_{core} \frac{dT_{core}}{dt} = (\dot{Q}_{exo,core} + \dot{Q}_{ohmic,core}) + \frac{T_{mid} - T_{core}}{r_{c2m}} \tag{3.1}$$

$$C_p m_{mid} \frac{dT_{mid}}{dt} = (\dot{Q}_{exo,mid} + \dot{Q}_{ohmic,mid}) - \frac{T_{mid} - T_{core}}{r_{c2m}} + \frac{T_{surf} - T_{mid}}{r_{m2s}} \tag{3.2}$$

$$C_p m_{surf} \frac{dT_{surf}}{dt} = (\dot{Q}_{exo,surf} + \dot{Q}_{ohmic,surf}) + \frac{T_{amb} - T_{surf}}{r_{s2a}} - \frac{T_{surf} - T_{mid}}{r_{m2s}} \tag{3.3}$$

where T_{core}, T_{mid}, T_{surf} represent core, middle layer and surface temperature. m_{core}, m_{mid}, m_{surf} represent mass of core, middle layer and surface. r_{c2m}, m_{m2s}, m_{s2a} represent thermal resistance of core to middle layer (c2m), middle layer to surface (m2s) and surface to ambient (s2a). Q_{exo} is the exothermic side reactions heat, Q_{ohmic} is the ohmic heat from ISC.

At the first few seconds of ISC process, T_{core} quickly rise to 120 $°C$ (driven by the ohmic heating in the short circuit), while T_{mid} and T_{surf} remain at 57.5 $°C$ [52]. The system is linearized at this point to asses the surface temperature detection method. At this working condition, exothermic reaction heat and ohmic heat in middle layer and surface can be neglected.

For the exothermic reactions, Solid Electrolyte Interface (SEI) decomposition becomes active above 120 °C [6]. Comparing to ISC ohmic heat, exothermic reaction heat can be neglected at this temperature, but must be included as the cell temperate continues to rise because the reaction rate will increase exponentially with temperature [32].

The thermal model can be represented in state space representation form

$$\begin{bmatrix} \dot{T}_{core} \\ \dot{T}_{mid} \\ \dot{T}_{surf} \end{bmatrix} = A \begin{bmatrix} T_{core} \\ T_{mid} \\ T_{surf} \end{bmatrix} + \begin{bmatrix} \dot{Q}_{ohmic,core} \\ 0 \\ \frac{T_{amb}}{C_p m_{surf} r_{s2a}} \end{bmatrix} \tag{3.4}$$

$$y = C \begin{bmatrix} T_{core} \\ T_{mid} \\ T_{surf} \end{bmatrix} \tag{3.5}$$

where $C = [0, 0, 1]$ and the output here is the surface temperature.

In details, the A matrix is

$$A = \begin{bmatrix} A_{11} & A_{12} & 0 \\ A_{21} & A_{22} & A_{23} \\ 0 & A_{32} & A_{33} \end{bmatrix}$$

where $A_{11} = -\frac{1}{C_p m_{core} r_{c2m}}$, $A_{12} = \frac{1}{C_p m_{core} r_{c2m}}$
$A_{21} = \frac{1}{C_p m_{mid} r_{c2m}}$, $A_{22} = -\frac{r_{c2m}+r_{m2s}}{r_{c2m} r_{m2s} C_p m_{mid}}$, $A_{23} = \frac{1}{C_p m_{mid} r_{m2s}}$
$A_{32} = \frac{1}{C_p m_{surf} r_{m2s}}$, $A_{33} = -\frac{r_{m2s}+r_{s2a}}{r_{m2s} r_{s2a} C_p m_{surf}}$

For system with surface temperature as the only output, the observability matrix is

$$Q = \begin{bmatrix} C \\ CA \\ CA^2 \end{bmatrix} \tag{3.6}$$

Take the numerical values from the modeling result [52]. We have the observability matrix expressed as

$$Q = \begin{bmatrix} 0 & 0 & 1 \\ 0 & 0.0058 & -0.015 \\ 3.52 \times 10^{-4} & -0.0011 & 9.22 \times 10^{-4} \end{bmatrix} \tag{3.7}$$

The observability matrix is full rank, which means the system is observable with the surface temperature output alone. However, if we do Singular Value Decomposition (SVD) for the observability matrix

$$Q = U\Sigma V^* \tag{3.8}$$

The singular values σ_i will be given by the diagonal entries of

$$\Sigma = \begin{bmatrix} 1.0001 & 0 & 0 \\ 0 & 0.0059 & 0 \\ 0 & 0 & 0.0003 \end{bmatrix} \tag{3.9}$$

The observability matrix has a very high condition number

$$\kappa(Q) = \frac{\sigma(max)}{\sigma(min)} = 2892 \tag{3.10}$$

This shows that the observability matrix is close being rank deficient. This analysis demonstrates the poor observability for the internal temperature state based on surface temperature measurement alone. In real practice, with thermocouples located only at a few spots in a battery pack, the temperature response will be even slower. Better approaches are needed to identify the ISC event.

3.3 ISC Detection Based on Force

Previous studies [52] on single cell triggering hard internal short showed the relative slow response of surface temperature, and fast response of voltage and expansion force. The expansion force comes from the cell swelling due to gas generation. The SEI decomposition becomes active at around 120 $^\circ C$ [6], and follows the expression below [6]

$$(CH_2OCO_2Li)_2 \rightarrow Li_2CO_3 + C_2H_4 + CO_2 + 0.5O_2$$

The SEI decomposition directly generate gas that can contribute to severe cell swelling. The cell swelling converts to expansion signal. The expansion force, due to its fast response after a hard internal short, can be used for ISC detection.

As discussed previously, voltage and current signal are usually used for battery fault detection. However, the voltage based detection will not work for all cases. The cell casing may be compromised due to mechanical abuse, and for an intact cell with an unsealed cell casing, the cell can still operate normally in voltage with the applied current [53]. In this case, the expansion force sensor can help with the fault detection by identifying the over-stress before the cell casing is compromised. Additionally, introducing expansion force sensor for fault detection can help achieve high confidence level detection.

3.3.1 Expansion Force Model

At normal operating conditions, the cell expansion force can be expressed as a function of temperature and State of Charge (SOC). Previous studies showed the change of cell expansion force from fully discharged to fully charged state is around 155 N or 30% of the base preload for NMC-Graphite cells [54]. Compared to the peak force observed prior to venting during a thermal event, which was over 1800 N [52], the expansion due to SOC is small. We assume the temperature dependency and SOC dependency functions are separable [55]. We can then express the expansion force as

$$F = f_1(T) + f_2(SOC) \tag{3.11}$$

For the SOC dependency, the experiment of expansion force measurement uses the same setting as in [54]. The experiment settings for expansion force measurement are shown in Fig 3.1a. The expansion force measurement comes from the four load cells at four corners of the fixture. We use a eighth order of polynomial fit for the experimental data. The resulted expansion force with SOC dependency is shown in Fig 3.1b.

For the temperature dependency, here we use a linear thermal expansion model for the expansion force. The temperature dependency can be expressed as

$$f_1(T) = \alpha(T - T_0) \tag{3.12}$$

where T_0 is the initial temperature, and α is the thermal expansion rate. For α, different fixture and battery will have different thermal expansion coefficient. Here, we

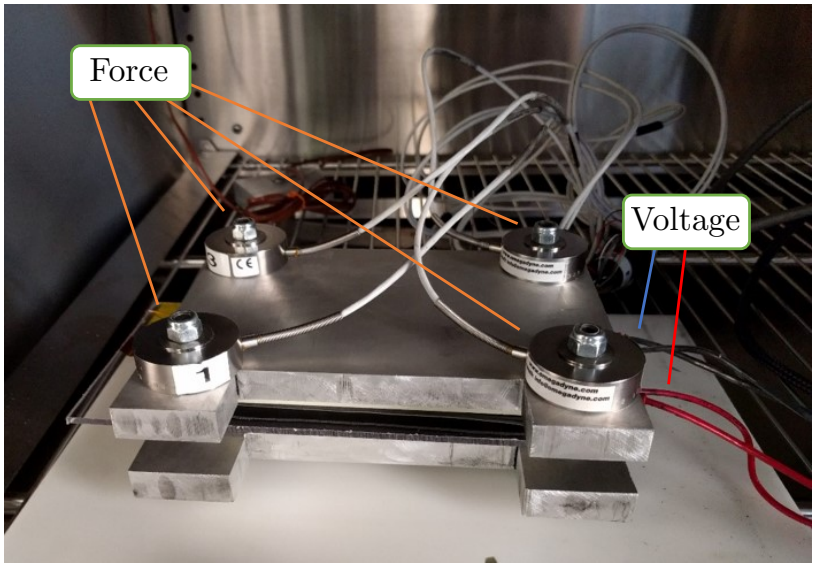

(a)

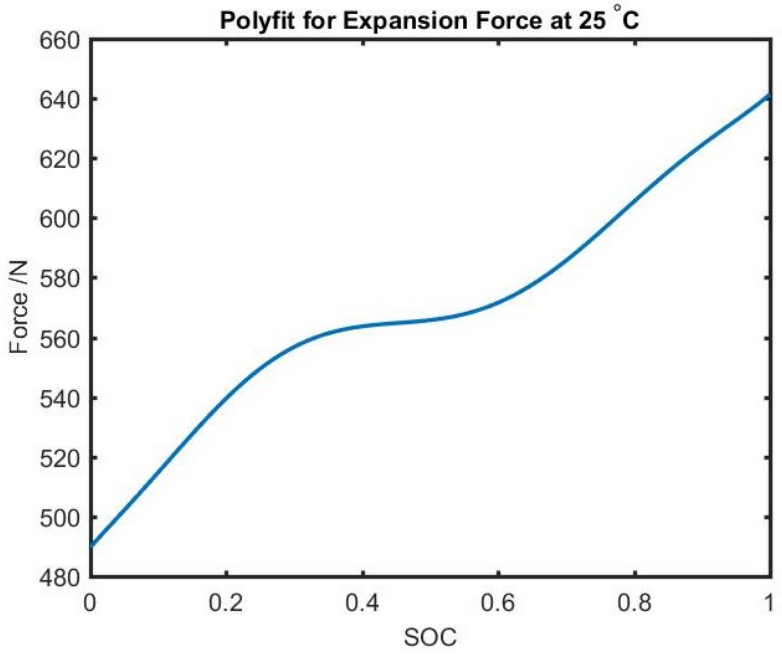

(b)

Figure 3.1: (a) Expansion force measurement setup. (b) Expansion force as a function of SOC.

calculate it based on the expansion force for the pouch cell at different temperature. The α in this study is 2.06 $N/°C$

During normal operating conditions, temperature distribution is rather uniform within a cell. The measured surface temperature can be used in the thermal expansion

model.

Other factors that impact expansion force include pre-load force. We assume local linearization for the force model that allows the separation of temperature, SOC and pre-load [55]. With pre-load force included in the model, the expansion force during normal operating conditions can then be expressed as

$$F = f_1(T) + f_2(SOC) + F_0 \tag{3.13}$$

where F_0 is the pre-load force.

3.3.2 Fault Detection Algorithm

Based on the expansion force model at normal operating conditions, we can build an observer for the expansion force

$$\hat{F} = f_1(T) + f_2(\hat{SOC}) + F_0 \tag{3.14}$$

$$\Theta_F = \bar{F} - \hat{F} \tag{3.15}$$

where $\bar{F}$ is the measured force, and Θ is the estimated residual from force signal. The residual of force signal is calculated from force measurement and estimated expansion force.

Here, we assume the $\hat{SOC}$ can be estimated by current and voltage measurement. Common methods for SOC estimation include Coulomb Counting method and Open Circuit Voltage inversion method. Coulomb Counting method is more popular in industry, as the battery terminal voltage changes in dynamic operations [54]. SOC estimation error can come from sensor noise and drift, model mismatch due to cell aging [13]. A 5% error in the estimated SOC would result in a prediction error of 8.9 N for Θ_F, based on the maximum slope in figure 3.1b. Closed-loop SOC estimation is needed with Kalman Filter [56] to balance between process error and sensor noise and achieve less SOC estimation error. To simplify the analysis here, we will use Coulomb Counting method for SOC estimation in this study.

At normal operating conditions, by assuming perfect model, the force measurement should be equal to the estimated expansion force, and Θ_F should ideally be zero. The F_{fault} term represents the force that comes from battery swelling due to an internal short. To put the two cases in summary:

During Normal Conditions

$$\bar{F} = f_1(T) + f_2(SOC) + F_0$$

$$\hat{F} = f_1(T) + f_2(\hat{SOC}) + F_0$$

$$\Theta_F \to 0$$

At Fault Conditions

$$\bar{F} = f_1(T) + f_2(SOC) + F_0 + F_{fault}$$

$$\hat{F} = f_1(T) + f_2(\hat{SOC}) + F_0$$

$$\Theta_F \to F_{fault}$$

The residual Θ_F should be zero during normal operating conditions with a perfect force model. At fault conditions, the residual Θ_F represents the fault force signal. Thus, the detection can be made using a threshold ϵ_F. When the estimated residual is larger than the threshold, a fault is indicated.

3.3.3 Adaptive Threshold

The estimated residual Θ_F and the fault detection depends heavily on the modeling accuracy. However, the cell degradation and aging will bring model mismatch over time. An adaptive threshold that considers the long term model drifts is required to improve the fault detection accuracy [57].

Considering the variation of the estimated residual Θ_F with input, the mean and variance of the estimated residual at the kth sample point in a moving window can be expressed as

$$R_k = \frac{1}{m}\sum_{i=1}^{m}\Theta_{F,k-i+1} \tag{3.16}$$

$$\sigma_{F,k}^2 = \frac{1}{m-1}\sum_{i=1}^{m}(\Theta_{F,k-i+1} - R_k)^2 \tag{3.17}$$

where m is the moving window size, which is set as 500 in this study [58], which corresponds to 50 seconds time window for 10 Hz sampling rate. R_k is the average value of the estimated residual Θ_F in the moving window, and $\sigma_{F,k}^2$ is the variance between Θ_F and the moving window average value R_k.

By assuming Gaussian distribution of the estimated residual for the expansion force [59], the confidence limits of estimated residual that represent a confidence of $(1-\alpha)$ is

$$P\{R_k - z\sigma_{F,k} < \Theta_F < R_k + z\sigma_{F,k}\} = 1 - \alpha \tag{3.18}$$

where α is the confidence level, and z is the coefficient related to the confidence level. z and α are correlated through the Gaussian distribution (eg. $z = 3$ corresponds to 99.7% confidence level). In this study, since the expansion force will change drastically during a fault, we can set the threshold higher without hurting the detectability. Upon detection of the ISC event, severe warning and emergency responses will follow, therefore false positive is strong undesired within a battery pack's lifetime. The coefficient z is 8 to ensure false positive rate less than 1×10^{-10}.

The adaptive threshold is then $R_k \pm 8\sigma_{F,k}$. The upper and lower bound of the adaptive threshold are shown as below

$$\epsilon_{F+} = R_k + 8\sigma_{F,k} \tag{3.19}$$

$$\epsilon_{F-} = R_k - 8\sigma_{F,k} \tag{3.20}$$

3.3.4 Adding Voltage Signal for High Confidence Level Detection

For high confidence level detection of battery faults, we can use multiple detection algorithms from different input measurement. If both detection algorithms indicate a fault, then an ISC alert will be confirmed and made.

We define the fault voltage as

$$V_{fault} = \hat{V} - \bar{V} \tag{3.21}$$

where $\bar{V}$ is the measured voltage, and $\hat{V}$ is the estimated cell voltage at normal operating conditions. The $\hat{V}$ term can be calculated from OCV-R-RC equivalent circuit model, as shown by Fig. 3.2. The detailed OCV-R-RC model parameter is shown in Table 3.1, which is measured from the pouch cell manufactured by University of Michigan Battery Lab.

Table 3.1: Cell equivalent circuit model parameters

Capacity	R_s	R_1	C_1
$4.5Ah$	$5.3m\Omega$	$10.4m\Omega$	$4.81 \times 10^3 F$

For single cell, after an ISC event, the terminal voltage experiences a significant drop. Since the large ISC current, the changes in State of Charge (SOC) has to be taken into consideration. The battery open circuit voltage $V(SOC)$ is a function of

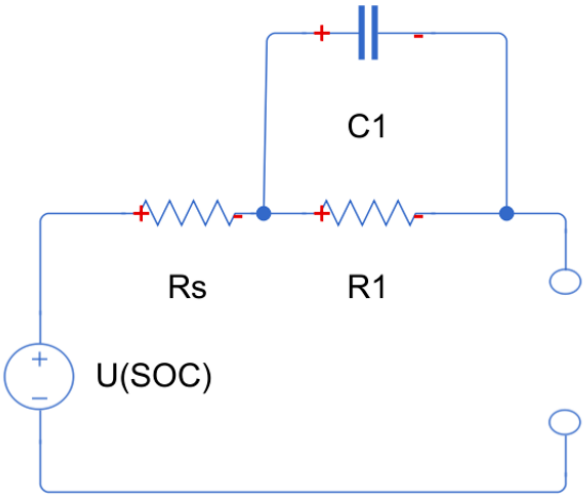

Figure 3.2: Equivalent circuit model representing the cell

SOC. The following equations describe the model for the estimated terminal voltage ($\hat{V}$)

$$\hat{V} = V(SOC) - IR_s - V_1 \tag{3.22}$$

$$\frac{dV_1}{dt} = \frac{-V_1}{R_1 C_1} + \frac{I}{C_1} \tag{3.23}$$

$$\frac{dSOC}{dt} = -\frac{I}{C_{cell}} \tag{3.24}$$

where C_{cell} represents the cell capacity.

Similarly, the adaptive threshold is used for fault voltage V_{fault}, and the upper and lower bound of the adaptive threshold can be set as

$$r_k = \frac{1}{m}\sum_{i=1}^{m} V_{fault,k-i+1} \tag{3.25}$$

$$\sigma_{V,k}^2 = \frac{1}{m-1}\sum_{i=1}^{m}(V_{fault,k-i+1} - r_k)^2 \tag{3.26}$$

$$\epsilon_{V+} = r_k + 8\sigma_{V,k} \tag{3.27}$$

$$\epsilon_{V-} = r_k - 8\sigma_{V,k} \tag{3.28}$$

If the fault voltage value falls out of the adaptive threshold, then the voltage detection system will trigger an alarm. After receiving alarms from both force and voltage, an ISC event is believed to happen and confirmed by both detection systems. In a summary:

Table 3.2: Detection logic with expansion force and voltage

Voltage	Force	Decision
$V_{fault} \notin [\epsilon_{V-}, \epsilon_{V+}]$	$\Theta_F \notin [\epsilon_{F-}, \epsilon_{F+}]$	ISC Alert, Confirmed
$V_{fault} \notin [\epsilon_{V-}, \epsilon_{V+}]$	$\Theta_F \in [\epsilon_{F-}, \epsilon_{F+}]$	ISC Warning, Electrical Fault
$V_{fault} \in [\epsilon_{V-}, \epsilon_{V+}]$	$\Theta_F \notin [\epsilon_{F-}, \epsilon_{F+}]$	ISC Warning, Overstress
$V_{fault} \in [\epsilon_{V-}, \epsilon_{V+}]$	$\Theta_F \in [\epsilon_{F-}, \epsilon_{F+}]$	Normal

In this study, after the battery ISC fault, the expansion force and voltage change drastically, and the model prediction will have large difference with the measurements. This difference is not a reflection of the modeling error in the normal operating conditions, therefore the σ_V and σ_F will stop updating after fault being detected.

3.4 Simulation Result

For this study, we consider a 4.5 Ah NMC pouch cell. The parameters of the cell are adopted from [52]. To emulate real measurements, here, we add zero mean white Gaussian noise ($N(0, \sigma^2)$) to the measurement. In details, for voltage measurement, the noise has covariance $\sigma_V = 5\ mV$. For current measurement, $\sigma_I = 5\ mA$. For temperature measurement, $\sigma_T = 0.5\ ^\circ C$. For force measurement, $\sigma_F = 8.9\ N$.

The simulation can be divided into two conditions: normal operating conditions and fault conditions. In the normal operating conditions, the Urban Dynamomenter Driving Schedule (UDDS) is used for the current profile. In the fault condition, the model from [52] is used to simulate a hard ISC case.

To analyze the algorithm's robustness against modeling error, we add the modeling error to the simulation during normal operating conditions. While the cell true capacity is 4.5 Ah, here we assume the cell capacity in the model is 5 Ah. For the expansion force model, we assume the model has an incorrect $f_2(SOC)$, and underestimates the expansion due to SOC change by 15%.

The battery SOC is initialized at $SOC = 100\%$ in the simulation. For the normal operating conditions, the UDDS current profile and the corresponding terminal voltage (V_T) and expansion force responses have been shown in Fig. 3.5. During normal operating conditions, even though we added sensor noise and modeling error to the simulation, both detection quantities stay far below the detection threshold, and no false alarms is triggered during the simulation.

For fault condition, the battery SOC is still initialized at $SOC = 100\%$, and the

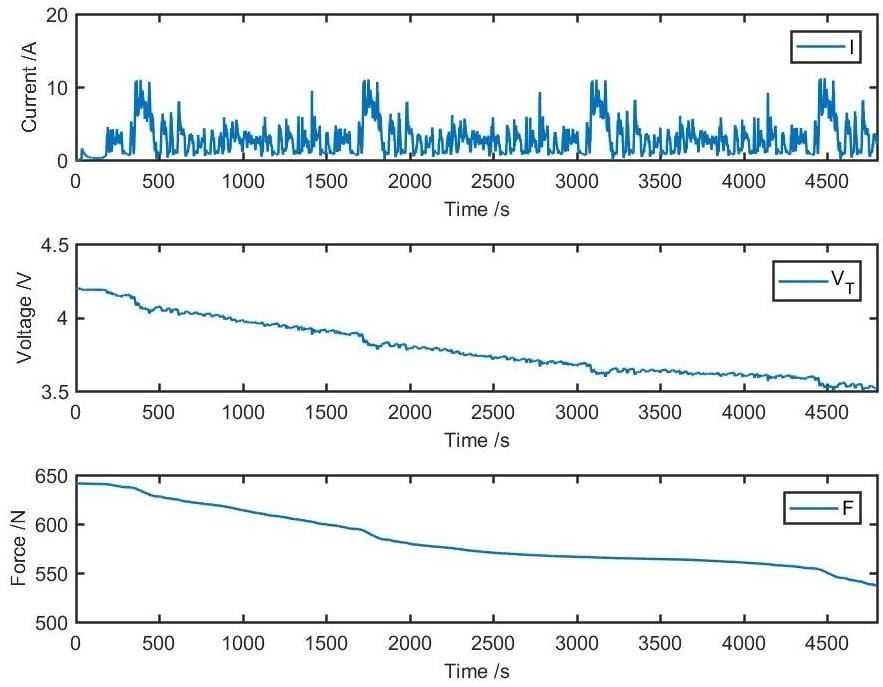

Figure 3.3: Current, terminal voltage and expansion force profile under UDDS profile at normal operating conditions

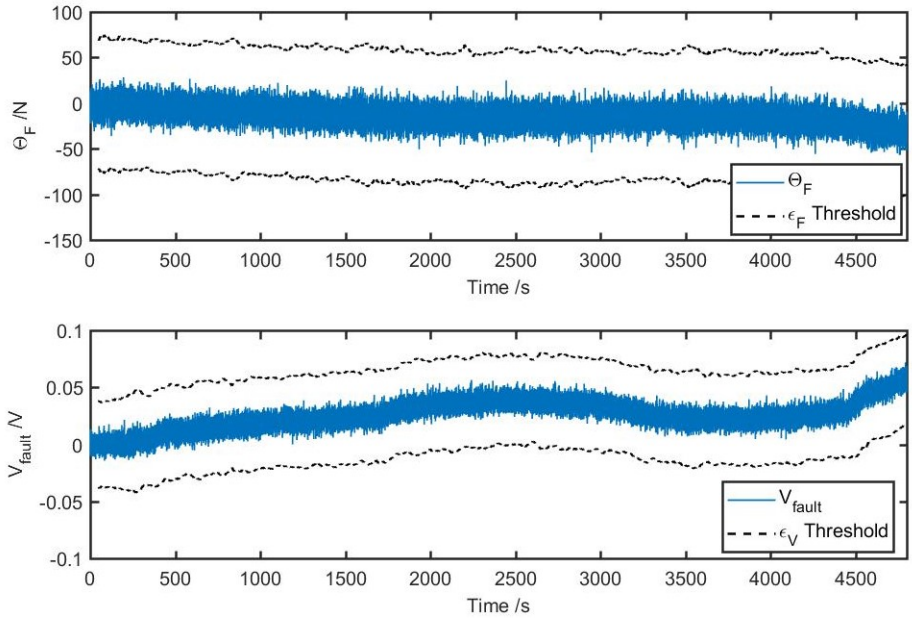

Figure 3.4: Both detection quantities, Θ_F and V_{fault} fall within the adaptive threshold during the normal operating conditions

UDDS current profile is applied in the first 10 seconds. At $t = 10s$, an ISC is triggered in the simulation which finally leads to a thermal runaway event. After the ISC event,

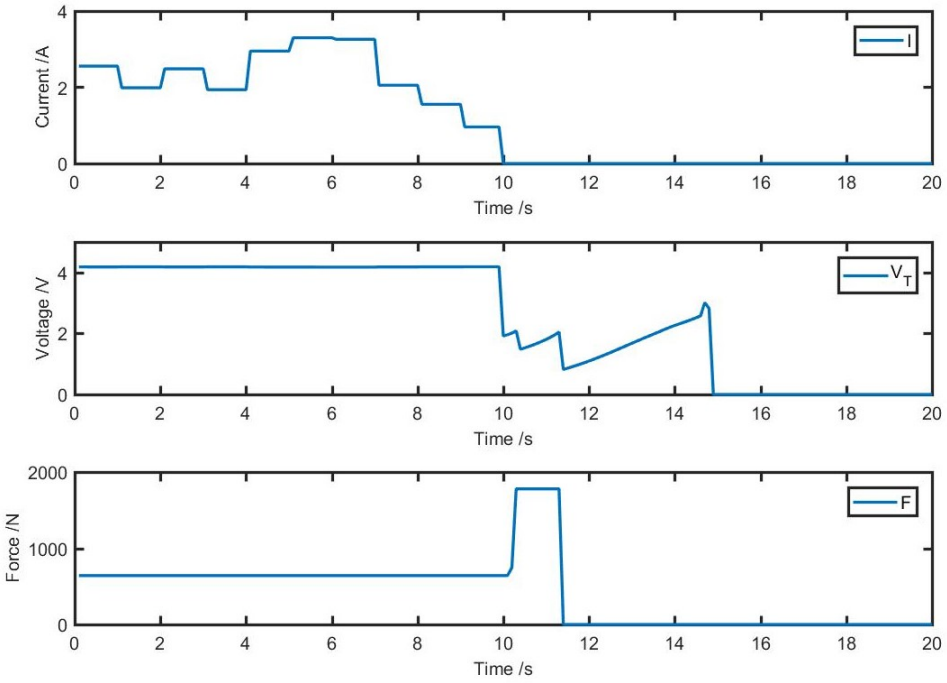

Figure 3.5: Current, terminal voltage and expansion force profile under a fault condition, with a hard short circuit triggered at $t = 10s$

we assume there is no external current flowing through the cell. The model from [52] is adopted to simulate a hard short which leads to a thermal runaway event. The simulated hard ISC event is shown in Fig. 3.5 for the current, voltage and force profile.

The estimated voltage fault term V_{fault}, estimated force fault term Θ_F after a short circuit triggered are shown in Fig. 3.6a. At the time of 10 seconds, the voltage fault term first detects an ISC event. At the time of 10.2 seconds, the force detection algorithm identifies the fault, and confirms the ISC event. Even though the confirmation of an ISC event requires threshold crossing from both voltage and force detection signals, it still achieves fast detection for a hard internal short event.

To be noticed, in Fig. 3.6b, at the time of 11.4 seconds, the Θ_F drops below the lower bound of threshold. This is due to the rupture of the cell, which leads to sudden drop of measured expansion force. The increase of surface temperature also follows the rupture and thermal runaway, which leads to higher estimated expansion force. These two factors cause the Θ_F to drop below the lower bound of threshold. This feature makes the force detection to continually identify this fault even after a long time of triggering the fault.

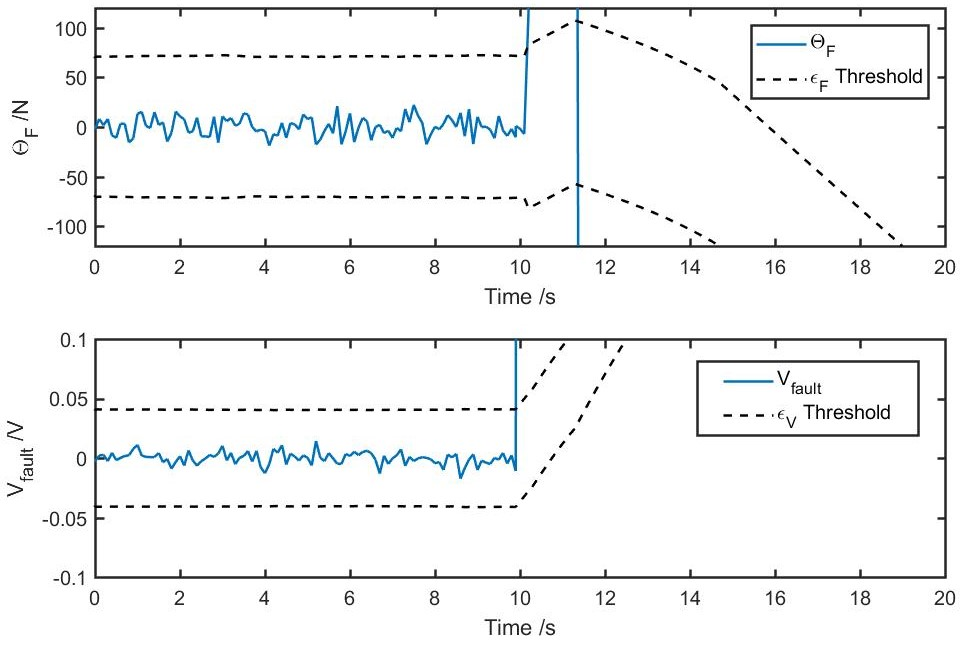

(a)

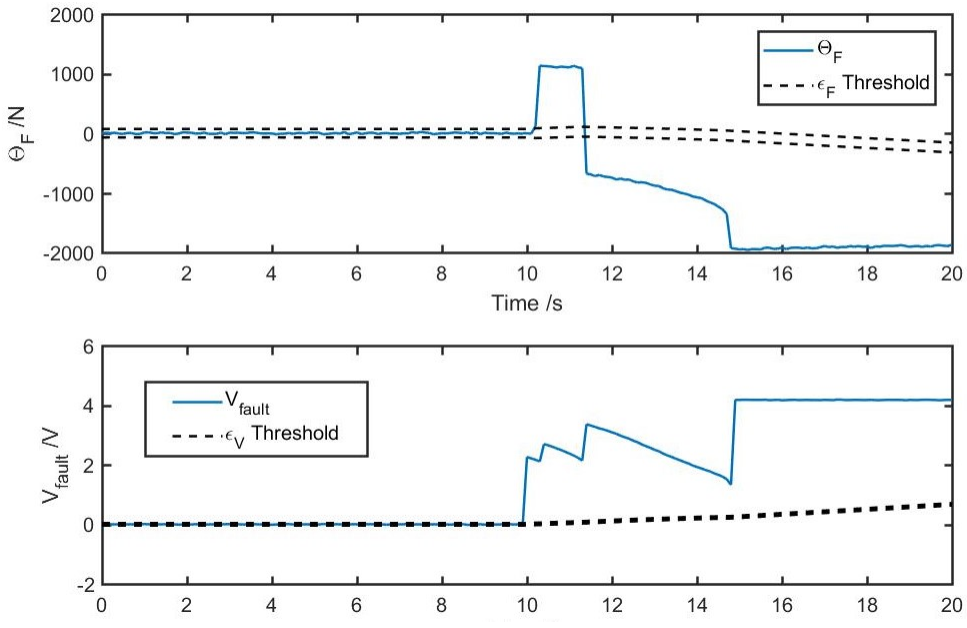

(b)

Figure 3.6: At fault conditions, voltage detection V_{fault} identifies a fault at $t = 10s$, and force detection Θ_F confirms the fault at $t = 10.2s$. (a) Zoom-in view (b) Overview of the detection quantities.

3.5 Summary

In this chapter, we propose a battery ISC detection method based on the measurement of the expansion force and voltage. Combining voltage and force signals for fault estimation can achieve a higher confidence level for detection of the fault and avoid unnecessary false alarms. The simulation results demonstrate the fast response of the detection algorithm after an ISC event. The simulation also verified that the method is robust to sensor noise and modeling error. Future work is encouraged with experimental validation for the detection method.

CHAPTER IV

Gas Sensing for Detection of Battery Venting

4.1 Introduction

Due to the drawbacks of the existing fault detection methods in battery packs, many studies have focused on gas detection for battery failure, primarily because of the fast response of gas sensing for cell failure and the easy implementation of gas sensors. The cell venting is usually categorized into first venting and thermal runaway gas venting [37]. The first venting happens when the cell internal pressure exceeds a critical value and the pressure burst disk opens [24]. The first venting happens before cell thermal runaway and can be used as a precursor of thermal runaway. The subsequent gas venting during thermal runaway is more aggressive and releases more vent-gas [37]. Prior studies on detecting cell thermal runaway in battery storage depots showed that a gas detection method targeting at CO_2 concentration has a much faster response than monitoring temperature at the storage drum surface [60].

Focusing on gas detection method for battery packs, the structure of this chapter is as followed. In Section 4.2, a summary of single-cell abuse experiments is presented to explore the compositions of vent-gas under different battery abuse conditions. Single-cell nail penetration, overheating and overcharging tests showed high concentrations of CO_2 in most cases with different battery chemistries and SOC. Due to the early presence in first venting, good consistency, and the ability to detect cell leakage, CO_2 is considered a good target gas. In Section 4.3, from implementation aspect of gas detection, low-cost volatile organic compounds (VOCs) sensors and CO_2 sensors are compared. In Section 4.4, a single cell abuse experiment is discussed where the Non-Dispersive Infrared (NDIR) CO_2 sensor is shown to support detection within seconds after the gas-venting occurs. In Section 4.5, we show how the CO_2 concentration data collected from a single cell venting experiment can be used to bound the CO_2

detection threshold and help with the gas detection algorithm design in a battery pack.

4.2 Review of Gas Compositions in Abuse Tests

To evaluate the gas evolution during all of the major battery failure modes, battery abuse experiments from the literature were summarized. In most tests, CO_2, CO, H_2 and volatile organic components (VOCs) were the main components, with other minor components in the produced gas such as oxygen (O_2) [61] and hydrogen fluoride (HF) [62]. Since many VOC sensors are sensitive to hydrocarbons (e.g. methane and ethane), we included them as VOCs in our summary. After considering a variety of abuse conditions, CO_2 has high concentrations in all conditions and is easy to detect, therefore CO_2 is selected as the target gas species for detection.

4.2.1 Case of Overheating Tests

In a prior work from Golubkov [63], thermal ramp overheating tests were conducted in inert gas atmosphere for Lithium Iron Phosphate (LFP) and Lithium Nickel Cobalt Aluminum Oxide (NCA) 18650 cylindrical cells at different State of Charge (SOC) ranging from 0% to 143%, and the vent-gas was analyzed using Gas Chromatography (GC). The results indicated that CO_2 is the primary gas in most cases, and in all tests CO_2 was significant in total molar concentration, constituting at least 17.5% and as high as 96.6% of the vent-gas. For CO, the generated amounts were relatively large compared to CO_2 for NCA cells at high SOC. However, at low SOC and LFP cells, CO concentrations were significantly lower than that of CO_2, constituting only about 1% of the total vent-gas. H_2 was another main component of vent-gas at high SOC, but similarly to CO, the percentage of H_2 in the vent-gas was around 1% at low SOC. The VOCs consisted of a relatively small percentage of the total vent-gas across the range of SOC, and in most cases it was less than 10%.

Similar overheating tests in inert gas atmosphere for fully charged Lithium Cobalt Oxide/Nickel Manganese Cobalt Oxide (LCO/NMC), Lithium Nickel Manganese Cobalt Oxide (NMC) and LFP 18650 cylindrical cells revealed that the main components of the produced gases were H_2 and CO_2 for each chemistry [64]. CO was the main component in LCO/NMC and NMC cells, but constituted only 5% of the vent-gas in moles for LFP cells. CO_2 ranged from 25% to 53% of total gas for all three types of cells, while the VOCs consisted of only around 15%.

Lammer [37] showed that in thermal ramp overheating tests for NCA cells in inert

gas atmosphere, CO_2 was again the dominant component for the first venting gas, ranging from 82% to 100% in moles for three kinds of commercial 18650 NCA cells. In the final deflagration stage, a large amount of gas was generated, where H_2, CO_2 and CO were the main components. The percentage of VOCs was found to be less than 10% after combustion.

In an experiment of cascading failure for battery arrays of 18650 LCO cells triggered by surface heating [65], a large spike of CO_2 concentration of 2% in volumes was observed after the first cell thermal runaway. After the rest of the cells went into thermal runaway, the detected CO_2 concentration increased to around 8% in volumes. The cell heating tests in N_2 atmosphere generated CO_2, CO, H_2 and hydrocarbons (HC). For tests in an inert gas atmosphere, higher volume percentages of HCs and CO were observed, which confirmed that the released HCs and CO will react with oxygen in the air. Similar phenomenon can be found for other overheating tests conducted in air. When the HCs and CO are ignited, their concentrations decrease significantly [66, 67]. This indicates that there will be a lack of consistency for these gas species, as they can react with outside oxygen, and could impair the detection of thermal runaway.

The battery pack active and passive mitigation method for suppressing thermal runaway can also impact the gas concentrations in a thermal runaway event [68, 69]. When employed with different mitigation methods, the CO_2 were still found in high concentrations in all cases, while HCs and CO were found in low concentrations in water mist system [69].

To summarize the gas composition results for overheating tests, CO and H_2 can only be detected in high concentrations for high SOC cells and only for select cell chemistries. On the other hand, VOCs can be detected in most cases, but gas detection with VOC may pose additional reliability challenges due to the decline in concentration after exposure to air [65, 70]. Lastly, CO_2 can be detected in high concentrations in all cases, regardless of cell SOC and cell chemistry.

4.2.2 Case of Nail Penetration Tests

During nail penetration tests, it was reported that gas was immediately emitted from the hole around the nail as it penetrated the cell, and swelling of the pouch cell exterior was observed due to the gas pressure [71]. However, gas component analysis was not conducted for this experiment.

In nail penetration tests for large scale NMC pouch cells [27], a gas sensor made with a tin dioxide (SnO_2) semiconductor was used for gas detection, and is sensitive

to methane (CH_4), propane (C_3H_8) and carbon monoxide (CO). The gas sensor had a clear signal after nail penetration, and detected the event 2 seconds after the nail penetrated the cell, while the cell voltage dropped 40 seconds later.

In another nail penetration study for NMC pouch cells conducted in air [72], the gas emission was analyzed by Gas Chromatography-Mass Spectrometry (GCMS) and Quadrupole Mass Spectrometry (QMS). Several kinds of VOCs (such as EMC, DEC, EC and benzene) were detected with gas chromatography. H_2, CO and CO_2 were detected in high concentrations from the QMS results. In one test, the concentrations for CO and CO_2 were both above 20,000 ppm, while another test using a neutralization filter system for the gas emissions showed lower concentrations for both gases.

In a summary for nail penetration tests, all four major gas species (CO_2, CO, H_2 and VOCs) can be detected in high concentrations.

4.2.3 Case of Overcharging Tests

Overcharging experiments for 18650 LFP cells conducted in air from [73] showed that the main components of the vent-gas at the end of the test were CO_2, H_2, C_2H_4, and CO, with CO_2 accounting for 47% of the sampled gas. The real-time gas concentrations during the abuse tests was also measured and showed that the concentrations of DMC in ppmv (parts per million volume) was much higher than that of CO_2 during the abuse tests. In the first venting event, which represents 0.7% of the total gas release, DMC can also be detected.

In another overcharging test for NMC prismatic cells conducted in air [74], CO_2 and CO were the main components of out-gas with CO_2 composing 32%-58% and CO composing 32%-45% of the total vent-gas.

4.2.4 Case of External Short Circuit Tests

External short circuit experiments for a pouch cell from [77] showed cell venting and peak cell temperature occurring at around 100 °C. In another study, external short circuit tests for single 18650 NMC cells showed the peak temperature reaching 96 °C, and cell leakage was observed [78]. These tests showed cell venting occurring 30 seconds after the short circuit.

Studies for external short circuit in battery packs pointed out that battery packs connected in series have higher short circuit current than that for a single cell [79], which can cause higher rates of temperature increase. Additionally, the short circuit behavior might be different in high-voltage systems, as the current interrupt device

Table 4.1: Summary of vent-gas composition under different battery abuse conditions (in volume %). CO_2 is the most consistent gas composition.

Conditions		CO_2	CO	H_2	$VOCs$ *
Overheating	NCA cylindrical (I), SOC=0%-25% [63]	62.7 - 96.6%	1 - 5.5%	0.8 - 15.5%	1.3 - 16.2%
	NCA cylindrical (I), SOC=50%-143% [63]	16.2 - 33.8%	39.9 - 49.2%	17.5 - 28.8%	6.1 - 12.5%
	NCA cylindrical (I), SOC=100% [37]	9.8 - 20.4%	37.2 - 58.4%	15.9 - 43.2%	5.3 - 9.9%
	→ First-venting	82.2 - 100%	0%	0 - 2.4%	0 - 15.4%
	LFP cylindrical (I) , SOC=0%-130% [63]	48.3 - 93.5%	1.8 - 9.1%	2.7 - 34%	2.1 - 13.1%
	LFP cylindrical (I), SOC=100% [64]	53%	4.8%	30.9%	11.2%
	LFP cylindrical (I), SOC=100% [66]	11.1%	4.7%	80.1%	4.1%
	LCO/NMC cylindrical (I), SOC=100% [64]	24.9%	27.6%	30%	17.5%
	NMC cylindrical (I), SOC=100% [64]	41.2%	13%	30.8%	15%
	NMC prismatic (I), SOC=100% [75]	25.2%	29.7%	10.4%	34.6%
	NMC pouch & hard case (A), SOC=100% [76]	36.6%	28.4%	22.3%	12.4%
	LCO cylindrical (I), SOC=100% [65]	12.7 - 13.9%	25.8 - 27%	18.2 - 18.5%	40.5 - 42.7%
	LCO cylindrical (A), SOC=100% [65]	8% (peak)	10% (peak)	–	2.5% (peak)
	→ First-venting	2%	<1%	–	0%
Nail Penetration	NMC pouch (A), charged to 4.3V [72]	>2%	>2%	Detected	High intensity
Overcharging	LFP cylindrical (A), at the end of test [73]	47%	4.9%	23%	24%
	LFP cylindrical (A), total gas [73]	18%	1.9%	9%	68.5%
	→ First-venting	DMC> CO_2 > CO			
	NMC prismatic (A) [74]	32.2 - 58.4%	31.7 - 45.1%	–	4.7 - 9.1%
Cell Leakage	LCO cylindrical, vacuum [53]	1.7%	–	–	44.6%

∗ Since VOC sensors are sensitive to hydrocarbons (e.g. methane and ethane), we count them into VOCs

(I) Experiments conducted in inert gas; (A) Experiments conducted in air

– Not reported

(CID) and positive temperature coefficient (PTC) have relatively low voltage tolerances, meaning that the devices can be ineffective under high voltage [77]. Sea water immersion tests conducted at 300V resulted in an electric arc under water and large amounts of gas were produced [80]. A fire was also observed while the cell was still

submerged in the water, which was due to the leakage of electrolyte.

The gas components in these experiments were not revealed. However, if the external short circuit in the battery pack leads to overheating of the cells and causes thermal runaway, then the thermal runaway characteristics will be similar to the overheating tests. Therefore, it is likely that VOCs, H_2, CO, CO_2 can be detected. Future experiments associated with battery external short circuit out-gassing components are required for verification.

4.2.5 Case of Cell Leakage

Cell leakage here represents an intact cell with an unsealed cell casing, which leads to a slow process of electrolyte evaporation to the outside of the cell. The cell casing can be compromised due to manufacturing defects or mechanical abuse. Experiments for 18650 LCO cells operated under normal conditions in vacuum condition showed that the leaked gas components include HCs and CO_2 [53]. It is likely that CO_2 comes from the reaction of VOCs with ambient oxygen [72]. If the leaking cell was overcharged or over-discharged, due to the accelerated electrolyte decomposition, the volume of generated gas and the percentage of CO_2 in the generated gas would increase significantly [53].

4.2.6 Target Gas Identification

The above discussions for battery abuse testing showed that different abuse conditions, cell SOC, cell chemistry, and atmosphere (in air or inert gas) can all influence the composition of out-gassing components. From this, the following criteria should be used to select the target gas:

(1) Consistency: The gas is consistently found with relatively high concentrations for all cell chemistries and abuse conditions.

(2) Early presence: Ideally, the gas can be found in the first vent-gas and be detected within seconds of being emitted.

(3) Leakage detection: the gas is a main component of cell leakage, so that the gas sensor can also be used to detect cell leakage.

Table. 4.2 shows the summary of different target gas species for detection. The explanations for the grades are given below.

Carbon Dioxide (CO_2): CO_2 was found in large concentrations for all test conditions reviewed in the literature, as shown in Table 4.1. The major component of first venting gas was CO_2, which was verified in experiments from literature [37,

Table 4.2: Summary of different target gases for detecting thermal runaway. Grading ranges from good (+), neutral (N) and bad (–).

Gas Species	Consistency [a]	Early Presence [b]	Leakage Detection
CO_2	+	+	+
CO	–	N	–
H_2	–	N	–
VOC	N	+	+

[a] Consistency: The gas is found with high concentrations consistently in all thermal runaway tests.
[b] Early Presence: The gas is found with high concentrations in first venting before thermal runaway.

65, 73]. Overheating experiments for over 50 cells also indicated CO_2 as having the highest volume percentage in the vent-gas [76]. Prior work [24] also assumes the primary component for first venting gas is CO_2, so CO_2 is considered to have early presence during a cell venting. Finally, CO_2 is found in the cell leakage gas, so the sensor can be used during slow leakage with CO_2 detection.

Carbon Monoxide (CO): CO was found in large amounts in the vent-gas of battery abuse tests. However, the concentration of CO decreased for cells with lower SOC [81] and in the LFP cell thermal runaway case [63], so CO is considered inconsistent regarding detection. For first venting events, some experiments reported the presence of CO [65, 73], while others did not [37]. Due to this inconsistency, a neutral score is given for early presence of CO. Finally, CO is not found in the cell leakage gas.

Hydrogen (H_2): H_2 was found in large amounts in some battery abuse tests, but not for cells with lower SOC, so the consistency is considered low for H_2. Similar to CO, H_2 was not detected consistently in first venting events, so the early presence is considered neutral for H_2. Finally, H_2 is not detected in the cell leakage gas.

Volatile Organic Components (VOC): VOCs were found in large amounts in most cases. However, the concentrations of VOCs are significantly lower in experiments conducted in air and gases after combustion [37, 65]. VOCs can also gradually react with oxygen from the environment to form CO_2 and H_2O [72], which can reduce the detection consistency in large packs. Based on the inconsistency of VOC concentrations in different conditions, a neutral grade is given for consistency of VOCs. For early presence, the first venting events are usually accompanied by a leakage of solvent, which can provide large amounts of VOCs upon first venting. Additionally, VOCs are the main components of cell leakage, so VOC sensors also enable the cell

leakage detection.

In a summary, CO_2 and VOC are found in high concentrations in vent-gas from all thermal runaway experiments. Both gas species exist in the first vent-gas, and enable cell leakage detection, so these two gas species are considered good for detection purposes.

4.3 Gas Sensor Types

To apply the gas detection methods to battery packs, the ideal sensor should satisfy the feasibility requirement: small in size, low-cost, low-power consumption, small sensor drift over the lifetime and low potential for sensor poisoning. VOC sensors include photo-ionization detectors, electrochemical gas sensors, semiconductor sensors (resistive sensors), spectroscopic sensors, micro gas chromatographs, and electronic noses and sensor arrays [82]. CO_2 sensors include chemical sensors and NDIR sensors. Since CO_2 and VOCs are major components of released gas, high accuracy sensors are not needed for detection. Therefore, lower-cost sensors can be used. Here, we only analyzed the sensor feasibility of some common and low-cost gas sensors for VOCs and CO_2. The summary of different sensors is listed in Table 4.3, and is described in detail below:

Table 4.3: Summary of common low-cost gas sensors for VOCs and CO_2

Gas Sensor Type	Principle	Cross Sensitivity	Drift (% per year)	Lifetime (years)	Unit Price ($)
Electrochemical VOC	Measure potential or current for reaction at the electrodes	Yes	2 - 15%	7 - 10	20 - 30
Semiconductor VOC	Measure electrical resistance of metal oxide	Yes	5%	5	5 - 10
Chemical CO_2	Sensitive layers for detection	Yes	3 - 5%	2 - 5	15 - 35
NDIR CO_2	Optically measure specific wavelengths of light	No	0.15%	15	8 - 20

Electrochemical VOC sensor: Electrochemical VOC sensors (amperometric sensors) are made of a measuring electrode, a counter electrode, and a reference electrode [82]. These sensors are low cost, low power, and compact, but they also are cross-sensitive to other gases, suffer long-term drift (up to 15% drift per year), and

can be damaged in low-humidity environments [82]. The price of an electrochemical VOC sensor is generally about $ 20 to $ 30 [83].

Semiconductor VOC sensor: By monitoring the electrical resistance of metal oxide, detection can be made for VOCs. Tin dioxide (SnO_2) is the most used sensor of this type due to its broad reactivity to VOCs and large changes in resistance [82]. The broad reactivity means that SnO_2 semiconductor sensors are sensitive to not only various VOCs, but also NO, NO_2 and CO [82]. However, this sensor suffers from sensor contamination [84] and signal drift [85] and has a large power consumption [27]. The unit price of a semiconductor VOC sensor generally ranges from $ 5 to $ 10 [86, 87].

Chemical CO_2 sensor: Chemical gas sensors with sensitive layers targeted at CO_2 have a low energy consumption. The sensor price is generally from $ 15 to $ 35 [88]. However, the sensor drifts over time and degrades quickly [89]. Due to the drift and degradation, this sensor needs frequent replacement and hence increases the total cost of using the battery pack.

NDIR CO_2 sensor: The sensor is based on optical principles. Since many gases absorb specific wavelengths of infrared light, it is possible to calculate the gas concentration by passing light of a defined wavelength and measuring how much light is absorbed [90]. For CO_2, the commonly used wavelength is 4.26 μm, which is not absorbed by other commonly found gases or water vapor [90]. The NDIR CO_2 sensor is the most commonly used CO_2 sensor type in HVAC applications [91]. The sensor is highly selective for CO_2, and due to the absorption exclusivity of the selected wavelength, any sensor cross-sensitivity can be largely avoided [90]. The atmospheric CO_2 concentration can also be used to calibrate sensors on a daily basis, which prevents sensor drift over time and ensures long-term use without maintenance. The NDIR CO_2 sensor has a unit price ranging from $ 8 to $ 20 [92], and has a lifetime up to 15 years.

→ Due to the good selectivity, reasonable cost, small sensor drift and good lifetime, the NDIR CO_2 sensor feasibility is considered good and is selected as the gas sensor for detection.

4.4 NDIR Detection Response Experiment

Most of the previously published works used gas chromatography for component analysis, which provides accurate and detailed results but the measurements are only at selected time points (usually at the end of the test). Gas sensors for specific

gases can enable real-time gas measurement [93], which is needed by the Battery Management System (BMS) to detect cell failure if specific gas concentrations exceed certain thresholds. To this end, an overcharging abuse experiment was conducted to show the effectiveness of NDIR gas sensor targeting CO_2 by causing venting for a commercial prismatic cell inside a small enclosure.

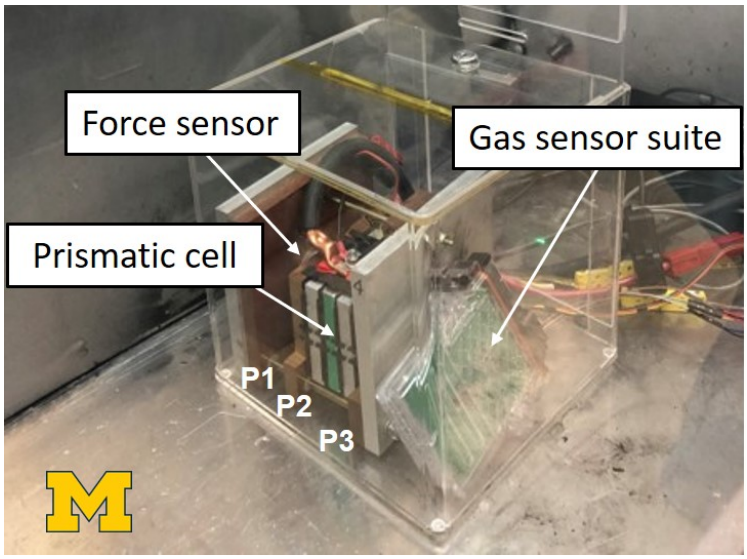

Figure 4.1: The overcharging experimental setup. The fixture was placed in an unsealed enclosure with a prototype gas sensor suite by Amphenol Advanced Sensors, which measures the CO_2 concentration, humidity and gas temperature.

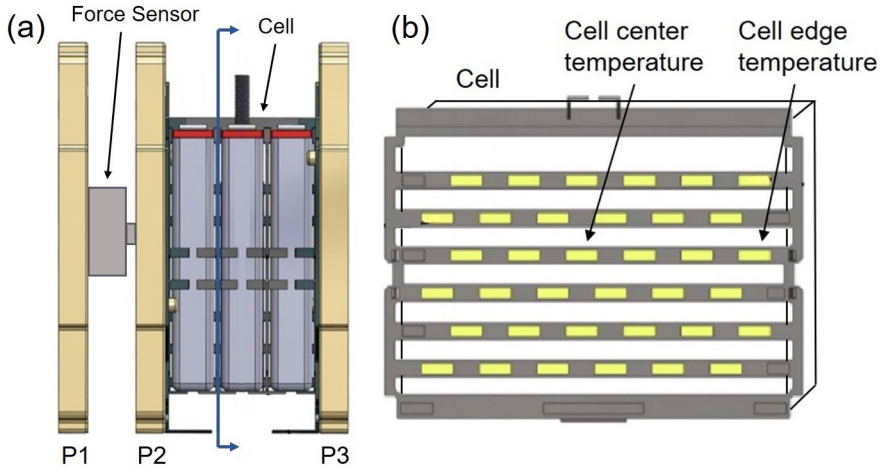

Figure 4.2: Schematics of the fixture with battery cell (a) and the plastic spacer (b). The battery and two aluminum dummy cells were placed in the fixture, with a force sensor measuring the expansion force. The plastic spacers separated the cell and the aluminum dummy cells. The K-type thermocouples were inserted to measure cell temperature.

4.4.1 Experimental Method

A commercial Lithium Nickel Manganese Cobalt Oxide (NMC) prismatic cell manufactured by Sanyo with an electrical capacity of 4.9 Ah and a voltage range of 3.0 V to 4.2 V was used in an overcharging abuse test. The size of the prismatic cell is $120 \times 85 \times 14\ mm$.

The cell was charged with a constant current of 15A (3C rate) until a SOC of 213% was reached, and then the current was increased to 20A (4C rate) until gas venting occurred. The overcharging experiment is illustrated in Fig. 4.1. The prismatic cell is located between two aluminum blocks in a fixture similar to the one used in [94]. The schematics of the fixture is shown in Fig. 4.2, where the plates "P1", "P2" and "P3" correspond to the same plates in Fig. 4.1. The expansion force was recorded by the force sensor located at the side of the fixture. The gas sensor was located next to the fixture. The whole device was placed inside an acrylic box that had a small opening at the backside due to the wiring at the bottom. The unsealed design of the acrylic box was to avoid pressure build-up.

The voltage, current, cell surface temperature, expansion force, gas temperature, CO_2 concentration, humidity and pressure were recorded using a LabVIEW PXI-based data acquisition system. The CO_2 sensor is a Telaire T6703 NDIR CO_2 sensor from Amphenol Advanced Sensors [92], with an accuracy of $\pm 10\%$. The gas temperature sensor measures the temperature of the detected gas on the gas sensor. The pressure sensor, gas temperature sensor, humidity sensor and NDIR CO_2 sensor are all integrated into the prototype gas sensor suite provided by Amphenol Advanced Sensors. The force sensor is an Omegadyne LC305-500 load cell.

4.4.2 Results and Discussion

Due to the six-volt voltage protection limit of the power supply, the charging current decreased after the gas venting event, and no thermal runaway was triggered. The cell was later discharged to safely handle the device. Fig. 4.3 shows the battery fixture inside the acrylic box before and after the gas venting event. The enclosure was filled up by vent-gas and white fumes. The produced white fume was mainly due to the released electrolyte vapors [95]. The cell voltage, charging current, expansion force and temperature are shown in Fig. 4.4.

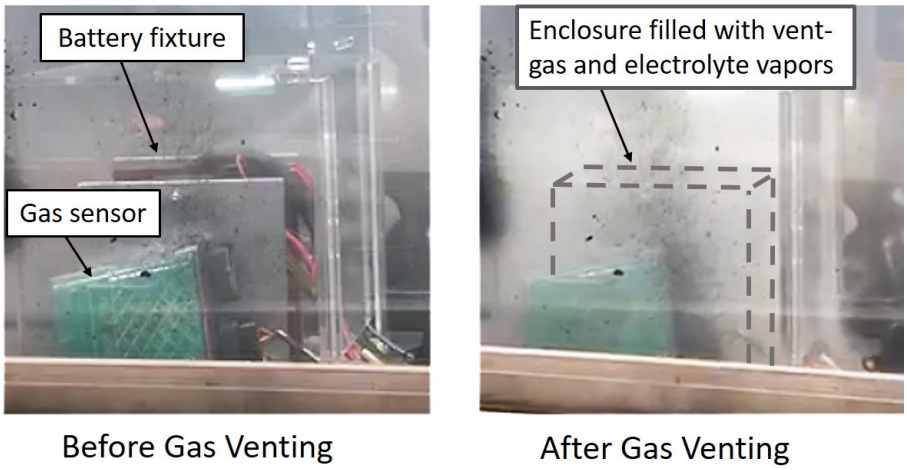

Figure 4.3: The battery fixture before and after the gas venting event. After the gas venting, the enclosure was filled up by vent-gas and white fumes of electrolyte vapors.

4.4.2.1 Voltage, force and temperature response

During the overcharging test, the voltage increased gradually but later showed a drop at t=300 s. This voltage overshoot behavior during overcharging was also observed in [96], and can be attributed to the sudden increase of transport resistance in the electrolyte associated with lithium plating [96]. Shortly before the cell failure, the voltage increased rapidly and peaked at 4.79 V when the gas venting occurred. After the gas venting, the cell voltage quickly reached 5.23 V, which was the saturation limit of the voltage measurement system.

As the cell started to overcharge, the measured cell expansion force increased and peaked at 2,900 lbf (12,900 N), which reached the force sensor saturation limit. After the gas venting occurred at t=1,181 s, the expansion force quickly dropped to 140 lbf (622 N). This drop of expansion force is also used to characterise the timing of the gas venting event.

Since the battery and the fixture had a rigid connection, the increased expansion force represented the battery internal pressure. The battery internal pressure can be estimated using the measured expansion force and the contact area of the cell. Accounting for the maximum expansion force (12,900 N), the contact area of the cell ($120 \times 85\ mm$) and the atmospheric pressure, the equivalent internal gas pressure was about 1,360 kpa. This estimated pressure is comparable to the critical vent pressure of 1,224 kpa reported in [24].

The cell internal resistance can be approximated using the voltage drop by interrupting the charging current.The cell resistance increased significantly from 5 $m\Omega$ before the experiment to 165 $m\Omega$ after the gas venting. This was likely due to the loss

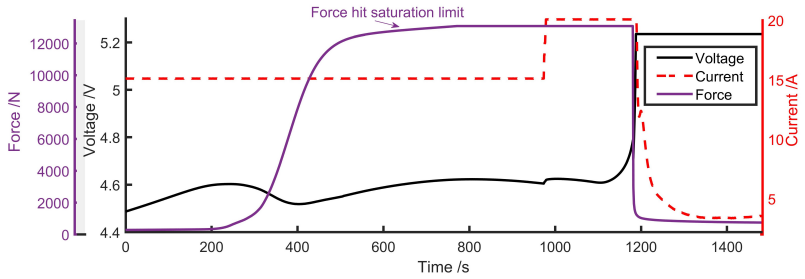

(a)

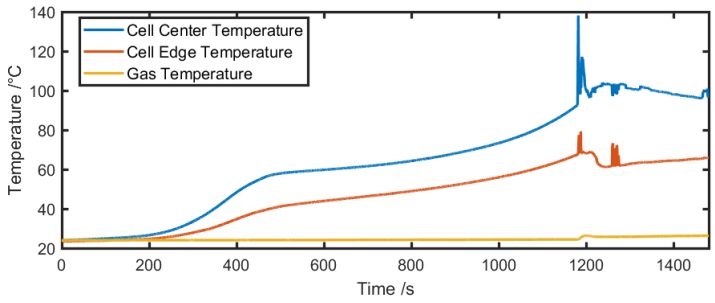

(b)

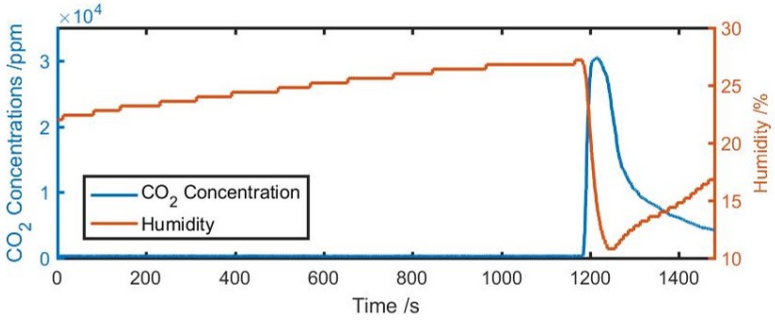

(c)

Figure 4.4: Voltage, current, force, temperature, gas and humidity measurement during an overcharging experiment are shown. (a) The gas venting occurred at t=1,181 s based on the sudden drop of battery expansion force observed. (b) The peak surface temperature at the center of the cell was 138 °C, however no thermal runaway was triggered. (c) After gas venting, the CO_2 concentrations quickly reached over 30,000 ppm.

of electrolyte from venting. Due to the increased internal resistance and the power supply voltage protection, the charging current decreased after the venting.

The cell surface temperature at the center of the face reached a peak of 138 °C. Because this was a thick prismatic cell (14 mm thickness) with a heavy aluminum casing, the cell core temperature may be higher. The difference between the cell center temperature and edge temperature also reveals the temperature gradient of

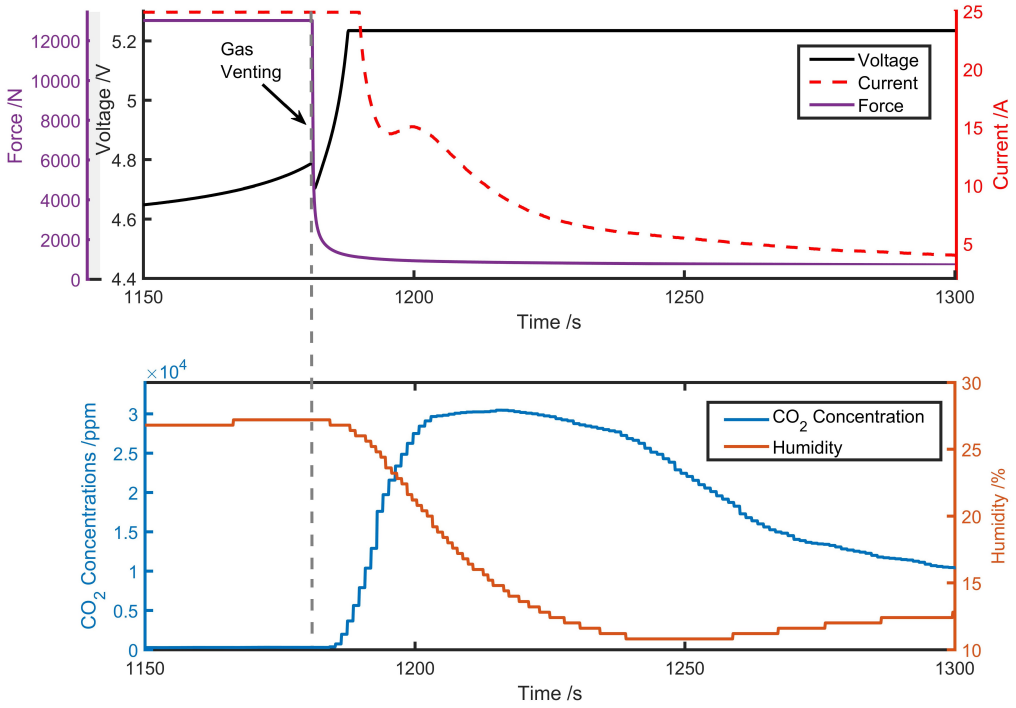

Figure 4.5: After the gas venting, the CO_2 concentration started to increase within 5 seconds, and eventually dropped since the enclosure was not sealed. At the same time, humidity was shown to drop from the vent gases.

the cell. Before the venting, the temperature difference for the cell center and cell edge was 25 °C. During the venting, this temperature difference reached 70 °C. With a core temperature above 130 °C, the SEI and electrolyte will start to decompose [6], and CO_2 will be generated. Notably, the gas temperature readings from the gas sensor were almost constant, which might be due to the Joule-Thomson effect that caused the cooling of the vent-gas [36] and the relatively large volume of the box.

4.4.2.2 Gas sensor response

The pressure sensor readings, however, showed little change during the gas venting event and is not included in the plot. This is mainly due to the small openings at the backside of the acrylic box. Koch et al. [27] also indicated that the pressure sensor will only work for a well-sealed battery pack. We used these openings to avoid pressure build-up in the box and avoid a possible explosion.

The CO_2 concentration increased quickly after the gas venting, reaching 10,000 ppm in 11 seconds and 30,000 ppm in 26 seconds after gas-venting occurred. As a reference, the atmospheric CO_2 concentration is only around 400 ppm, which is the sensor reading before the gas venting event. The acrylic box has a volume of 21.5 L.

The fixture, battery, and sensor have a total volume of around 3.1 L, so this will leave 18.4 L of ambient air volume inside the acrylic box. By using the maximum CO_2 concentration and the ambient air volume, and neglecting the gas that escaped the box, we can roughly estimate the amount of CO_2 to be 0.55 L. At room temperature and atmospheric pressure, this volume corresponds to 22.7 mmol of CO_2 released in the gas venting.

As shown in Fig. 4.5, the measured humidity decreased after the gas venting event. Since there was no water in the vent-gas or inside the cell, the vent-gas occupied the volume of air, leading to a decrease in humidity. Additionally, $LiPF_6$ in the electrolyte can react with water or moist air and can also decrease the humidity [62]. After the experiment, we observed some transparent liquid in the acrylic box, which came from the condensation of electrolyte and solvent vapor.

In conclusion, the NDIR CO_2 sensor showed a fast response, reaching 10,000 ppm in 11 seconds after the overcharging-induced gas-venting event, and therefore can be used for detecting gas-venting events.

4.5 Gas Detection Case Study in an EV Battery Pack

The single-cell gas release experiment verified the responsiveness of the sensor. Battery pack level analysis is then required to apply the gas detection method to packs. A survey for the battery pack gas venting system is the first step to investigate the applicability of the gas detection method. The effectiveness of the gas sensor for detection depends on the threshold setting. Based on a single cell venting test and the volumes of the battery pack vent-channel, one can set the detection threshold boundary. Here as an example, we studied the Ford Fusion hybrid electric 1.4 kWh battery pack, and suggested an upper bound of detection threshold for this specific pack.

4.5.1 Survey of Battery Pack Venting Systems

From surveying existing pack venting system designs, the most popular design uses a network of vent-channels to route the gas directly from the modules to a common gas outlet at the bottom of the pack casing. The 2013-2016 Ford Fusion Hybrid [97] and 2017 Toyota Prius Prime [98] battery packs are key examples of this, where the gas exhaust vents lie on top of the cell stacks and direct the gas to a single outlet. Other packs have slight modifications but follow the same general design. In Nissan's battery pack design patent, the ducts are located on both the upper and lower sides

of the modules and converge to a single outlet [99]. In a Fiat 500e battery pack, the venting system has multiple gas egress points due to the modules being grouped. Each group has a gas outlet [100, 101]. In all designs, the vent-gas will be released to the vehicle exterior through the gas outlet. By placing the gas sensor at the vent-gas outlet, the sensor can monitor the conditions of the entire pack.

During normal vehicle operation, the membrane at the outlet is designed to protect the pack from contaminants, equalize pressure inside the pack, and provide ventilation to expel damp air [102]. In the case of gas venting events, the membrane is designed to open due to the pressure build-up to allow large amounts of vent gas to be released [102].

To help illustrate the gas detection for thermal runaway events in a pack with vent-channels, a specific battery pack and its vent channel configuration are shown in Fig. 4.6a. The pack is based on the 2013 Ford Fusion hybrid electric 1.4 kWh pack [94]. Each module has a vent channel on the top of the cells that could receive, trap and evacuate the gas of any vented cells. The CO_2 sensor is located at the outlet of the gas venting channel, as depicted in the schematic.

To apply the gas detection methods in battery packs, two issues must be considered: (1) the delay of gas detection in packs due to the time needed for gas propagation, and (2) the threshold for gas detection.

4.5.2 Gas Detection Response Time

According to the overcharging experiment, the NDIR CO_2 sensor has a fast response time when placed next to the vented cell. After 11 seconds of cell venting, the recorded CO_2 concentration from the sensor exceeded 10,000 ppm. Considering the fast sensor response time, the main factor for the delay of gas detection method is the gas flow time.

In a battery pack, the damaged cell may not be located near the gas sensor and might delay the response due to the time needed for gas propagation. The gas propagation process is mainly driven by diffusion and convective mass transfer. While the diffusion process might have a time constant of over hundreds of seconds [103], the convective mass transfer will be much faster considering the fast speed of gas venting.

Most commercial cells have a critical gas venting pressure of 1224 kpa [24], and the outlet of the vent channel is atmospheric pressure (100 kpa). The large pressure difference can lead to a very fast venting flow speed, and by assuming isentropic nozzle flow, simulations have shown that the gas or ejecta venting speed can be supersonic

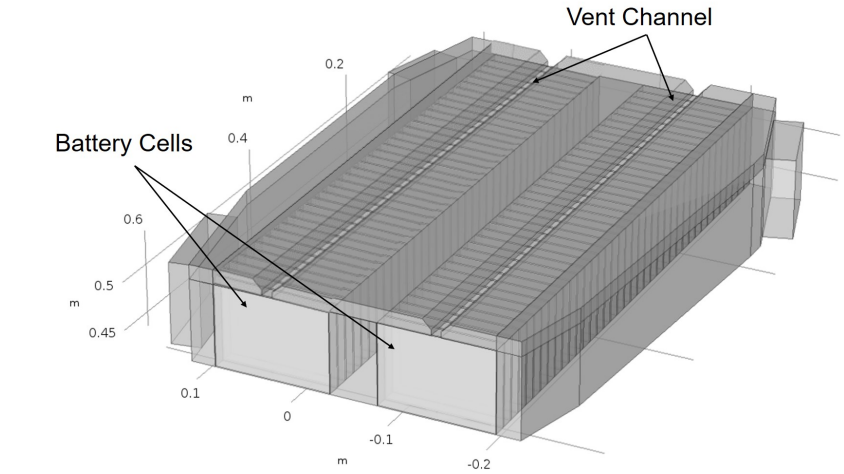

(a)

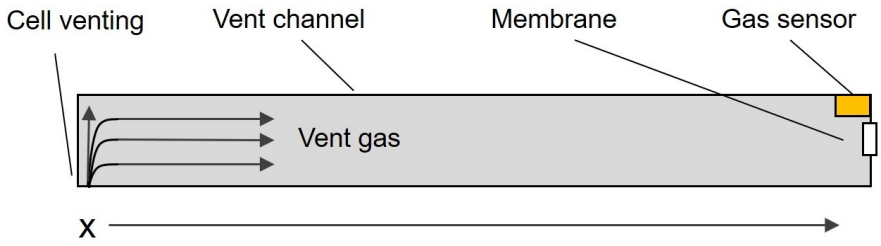

(b)

Figure 4.6: Schematic of a battery pack module and vent channel. (a) The vent-gas can easily enter the vent channel located above the cells, which will be detected by the gas sensor. (b) Cross-sectional view of the vent channel, where the vent-gas enters from the left side, and the gas sensor and membrane are located on the right.

[104]. In reality, due to the resistance, drag, and the pressure decrease after the initial venting, the vent gas speed will not reach that ideal velocity.

By using a high speed camera, prior studies showed that the flames of the first venting gas traveled 0.3 m in less than 300 ms [104], which corresponds to a gas flow velocity of over 1 m/s. Considering that the high speed camera only captured the flame speed, the velocity of the vent-gas and ejecta can be even higher. With a vent-channel length of 0.6 m, the vent-gas can easily reach the gas sensor location in a few seconds.

Since the travel time for the gas in the vent channel is considered fast, the major focus of gas detection methods is the gas detection threshold.

Table 4.4: Upper bound of detection threshold for CO_2 concentrations

Detection Event	Abuse Condition	Cell Type	CO_2 Release /mmol	Upper Bound of Detection Threshold* /ppm
First Venting	Overcharging	NMC prismatic, from this study	22.7	238,000
First Venting	Overheating	NCA 18650 [37]	1.6 - 6.2	22,000 - 79,000
Thermal Runaway	Overheating	NCA 18650 [37]	22.6 - 38.8	237,000 - 348,000
Thermal Runaway	Overheating	LCO 18650 [65]	28.9 - 34.3	285,000 - 321,000

* The upper bound of detection threshold is the volume-averaged CO_2 concentration.
Setting the threshold above this value can lead to failure to detect venting.

4.5.3 Gas Detection Threshold

The detection threshold selection is a trade-off between detectability and false-positive rates. A smaller threshold may lead to improved detectability of the fault but will bring higher false alarm rates. A large threshold can have a smaller false positive rate but will suffer from lower detectability. The volume-averaged CO_2 concentration and the single cell experiment can help to set the detection threshold boundary.

Due to the difference in pack volumes, the gas concentrations will vary in different cases. Here, we study the gas detection threshold that can be applied to the 2013 Ford Fusion hybrid electric battery pack. For the size of the vent channel, we assume it has a length of 0.6 m, width of 0.05 m, and height of 0.06 m. As seen in Fig. 4.6a, there are two stacks of cells in the battery pack, and correspond to two vent channels on top of cells.

A cross-sectional view of the vent channel is shown in Fig. 4.6b, where a membrane is located at the outlet of the vent channel. The membrane usually opens at a pressure between 20 and 100 millibars [105]. During gas release events, due to the membrane design, the gas in the channel takes time to vent to the outside of the pack. We assume the vent-gas mixes well with the vent channel air and the loss of vent-gas through the membrane will not change the relative percentage of CO_2 upstream. The volume-averaged CO_2 concentration in ppm (parts per million in volume) can be estimated by

$$c(CO_2)_{avg}\ [ppm] = \frac{10^6\ [ppm] \cdot n(CO_2)\ [mol]}{n(CO_2)\ [mol] + n(air)\ [mol]} \tag{4.1}$$

where $c(CO_2)_{avg}$ is the volume-averaged CO_2 concentration in the vent channel in ppm, $n(CO_2)$ is the amount of CO_2 in moles, and $n(air)$ is the amount of air in the

vent channel in moles. The $n(air)$ can be estimated through the volume of a single vent-channel ($V_{channel}$) using the ideal gas law

$$n(air)\ [mol] = \frac{P_{atm}\ [Pa] \cdot V_{channel}\ [m^3]}{R\ [m^3 \cdot Pa \cdot K^{-1} \cdot mol^{-1}] \cdot T\ [K]} \tag{4.2}$$

where R is gas constant, 8.314 $[m^3 \cdot Pa \cdot K^{-1} \cdot mol^{-1}]$. T is the average vent-channel temperature before venting, which is assumed to be 20 °C (293 K). P_{atm} is the atmospheric pressure, 10^5 Pa. In the assumed pack, $n(air) = 72.6$ $mmol$.

The $c(CO_2)_{avg}$ does not represent the actual CO_2 sensor readings, but due to the fast gas propagation, equilibrium can quickly be reached. Therefore, the $c(CO_2)_{avg}$ term is considered representative of the sensor readings upon a gas venting event.

When the amount of CO_2 generated is much smaller than the amount of air in the pack volume ($n(CO_2) \ll n(air)$), the volume-averaged concentration $c(CO_2)_{avg}$ in ppm can be approximated as a function of $n(CO_2)$ and $V_{channel}$:

$$\begin{aligned} c(CO_2)_{avg}\ [ppm] \approx K\ [ppm \cdot m^3 \cdot mol^{-1}] \\ \cdot \frac{n(CO_2)\ [mol]}{V_{channel}\ [m^3]} + c(CO_2)_{atm}\ [ppm] \end{aligned} \tag{4.3}$$

where $K = 10^6 \cdot RT/P_{atm}$. When the average temperate is 20 °C, the constant K is 2.4×10^4 $[ppm \cdot m^3 \cdot mol^{-1}]$. When the amount of CO_2 generated is small, the atmospheric CO_2 needs to be considered. $c(CO_2)_{atm}$ is the CO_2 concentration in the atmosphere, which is set as 400 ppm.

In section 4, upon the first venting event from overcharging for the prismatic cell, approximately 22.7 mmol of CO_2 was released ($n(CO_2) = 22.7$ $mmol$). Based on this, the volume-averaged CO_2 concentration can be calculated using Eq. 4.1. If the detection threshold is set higher than the volume-averaged CO_2 concentration, it can cause false negatives or failure to detect cell venting events. Therefore, the volume-averaged CO_2 concentration is the upper bound (ub) of the detection threshold (dthr) for the prismatic cell upon overcharging.

$$c(CO_2)^{ub}_{dthr} = 238,000\ ppm \tag{4.4}$$

For comparison, the CO_2 release and the upper bound of the detection threshold for different cells upon different abuse conditions are listed in Table. 4.4.

Since CO_2 can be generated from other sources in daily life, such as human respi-

ration and car exhaust, setting the detection threshold too low can trigger unwanted false alarms. As an example, for electric vehicle applications, in most cases the pack vent gas channel is directed to the vehicle exterior [106], so the car exhaust from outside can potentially lead to a false alarm. A study on CO_2 concentration on Minnesota highways reported a mean CO_2 concentration of 762 ppm with a standard deviation 75 ppm [107]. Assuming Gaussian distribution of the CO_2 concentration in highways under this condition, setting a detection threshold over 10,000 ppm can ensure the probability of having a false positive to be negligible ($< 0.001\%$). The lower bound for the detection threshold should be determined based on the specific usage of the pack and measurements of CO_2 concentrations in all operating conditions.

In summary, for the given battery pack and prismatic cell, the upper bound for CO_2 concentration detection threshold is 238,000 ppm for an overcharge-induced cell out-gassing event. For different cells or different abuse conditions including battery leakage, the upper bound for the detection threshold can also be informed by cell level experiments as in Section 5 and the volume-averaged CO_2 concentration based on the pack vent channel design details.

4.6 Summary

This study proposed a gas detection method for battery cell venting in battery packs. The summary of prior battery abuse experiments with overheating, overcharging and nail penetration all indicated the presence of CO_2 in the vent-gas. At the same time, CO, H_2, and VOCs were found in many battery abuse experiments, but lacked consistency across testing conditions. Considering the early presence in first venting, good consistency, ability to detect cell leakage, and sensor feasibility, CO_2 was selected as the indicator for gas venting events. The NDIR CO_2 sensor was selected for cell-level validation. The overcharging experiment demonstrated the fast and clear signal from the gas sensors after cell venting occurred.

A battery pack with a vent-gas channel located above the cells was investigated to evaluate the performance of gas detection. To help design the detection threshold, the idea of volume-averaged CO_2 concentration in the vent-channel was proposed to represent the gas sensor readings and was used as the upper bound for the detection threshold. Setting the detection threshold above this value can fail to detect venting events. In this study, based on the first venting event of the prismatic cell triggered by overcharging, the upper bound for the CO_2 concentration detection threshold is 238,000 ppm. The detection threshold boundaries for cell leakage and other abuse

conditions can be identified with additional cell-level experiments.

The overcharging experiments demonstrated the effectiveness of CO_2 detection upon gas venting in a single cell case, and the analysis for the pack showed the fast response and effectiveness of a gas detection system in a large battery pack. The proposed gas detection system requires only one gas sensor at the outlet of the vent gas channel. Additionally, the gas detection system has the unique advantage of being insensitive to the location of the vented cells.

The proposed gas detection system, however, is only sensitive to battery faults that involve gas venting. It requires other sensors and algorithms to detect different types of battery faults that do not have a gas venting phenomenon, including micro-internal shorts. Combined with multiple types of sensors, the system can be used for higher confidence level detection of battery thermal runaway events and diagnosis of battery internal short circuit events.

CHAPTER V

Cell Venting and Gas Flow Simulation

5.1 Introduction

In chapter 4, it is revealed that CO_2 is the major gas species released during the cell's first venting and a thermal runaway event. This chapter will follow the analysis of simulating the onset of cell first venting and gas release. The first venting model enables the estimation of CO_2 gas released for setting the gas detection threshold without the need for expensive testing. We then proceed with the analysis of gas flow in a battery storage drum after a cell failure to investigate the gas detection speed and sensor placement in the drum..

In battery packs, a single cell thermal runaway can lead to thermal runaway propagation of neighboring cells. Kim [108] simulated thermal runaway propagation in a large battery module, and showed that a single cell thermal runaway could lead other cells in the module to thermal runaway. The new thermal runaway cells could heat and damage more cells, causing a chain reaction. It is important that early detection should be made early enough before the second cell triggering thermal runaway so that mitigation strategies can be deployed. This time is referred to as propagation critical time (t_{crit}). In this chapter, the detection time is evaluated based on the comparison with thermal runaway propagation critical time.

In large battery storage containers, voltage, current and temperature measurement for every single cell is not available. Therefore, a method for monitoring the whole container's state is important. As indicated later in this study, traditional temperature sensing can be very late for the thermal runaway detection of large storage containers. Instead, using gas sensing will enable early detection in this system and be able to start emergency procedures before the thermal runaway propagates.

In this study, we focus on the scenario with a single 18650 cell thermal runaway in a 55 gallon (0.208 m^3) battery storage drum. The single-cell triggering thermal runaway

will vent gas and propagate the heat to neighboring cells. To show the effectiveness of the gas detection method, in this case, the gas flow in the battery storage drum is simulated in this work. The result shows that drum surface temperature monitoring is too slow to make the detection, while the proposed gas sensing method is much faster, and its detection time is before propagation critical time.

5.2 Modeling Onset of Cell Venting

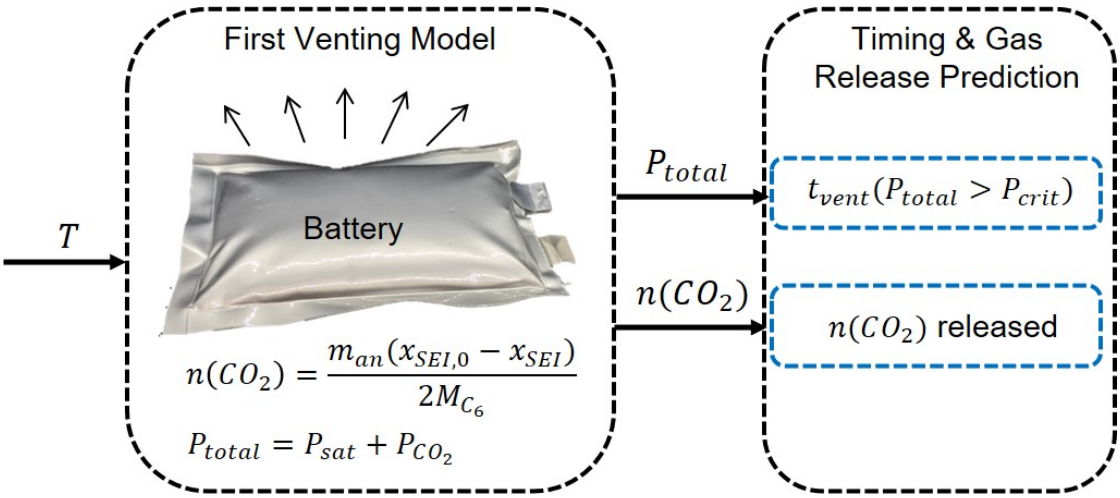

Figure 5.1: Overview of the first venting model. The model takes cell temperature as input, and outputs the generated CO_2 amount $n(CO_2)$ and the cell internal pressure P_{total}.

The overview of the model is shown in Fig. 5.1. The battery first venting model takes the measured cell surface temperature T as an input. If it is coupled with a battery thermal model, then it can be the average cell temperature from the model. The output of the model includes the the predicted amount of CO_2 released in the first venting event, $n(CO_2)$, and the cell internal pressure, P_{total}, which can be compared with the critical pressure to determine when the cell vents.

5.2.1 Modeling Gas Evolution

Gas evolution is one of the most important feature in battery safety events. Under battery abuse condition when the cell is at high temperature, the generated gas from side reactions can directly increase the cell internal pressure and leads to cell rupture [52]. One of the early exothermic reactions, the SEI decomposition, directly generates gas that can cause venting [52]. The SEI decomposition reaction follows the expression below [6]

$(CH_2OCO_2Li)_2 \rightarrow Li_2CO_3 + C_2H_4 + CO_2 + 0.5O_2$

The primary gas species detected in the first venting is CO_2 [37], and the CO_2 gas generation process is assumed to be associated with SEI decomposition in Ref [24]. In this model, we only consider the CO_2 generated by SEI decomposition to characterize $n(CO_2)$. The SEI decomposition reaction rate will increase exponentially with temperature [12, 32], and can be expressed as below

$$\frac{dx_{SEI}}{dt} = -A_{SEI} \cdot x_{SEI} \cdot \exp\left(-\frac{E_{SEI}}{k_b T}\right) \tag{5.1}$$

where x_{SEI} is the fraction of Li in the SEI, representing the progress of SEI decomposition, A_{SEI} is the frequency factor for SEI decomposition and E_{SEI} is the activation energy for SEI decomposition, k_b is Boltzmann's constant, and T is the cell temperature.

The amount of CO_2 produced from SEI decomposition can be expressed as a function of SEI decomposition progress x_{SEI} [52]

$$n(CO_2) = \frac{m_{an}(x_{SEI,0} - x_{SEI})}{2M_{C_6}} \tag{5.2}$$

where $n(CO_2)$ is the amount of CO_2 in mole, m_{an} is the anode mass, $x_{SEI,0}$ is the initial x_{SEI} before side reactions become active, and M_{C_6} is the molar mass (g/mol) for C_6.

5.2.2 Modeling Cell Internal Pressure

Before the cell evolves into a full thermal runaway, gas venting will be triggered when the cell internal pressure reaches a critical value. The exact pressure at which the battery vents depends on the form-factor and design. As an example, for the 18650 cylindrical cell studied by [24], the first venting would occur when the cell internal pressure reached 1224 kPa. The pouch cell in this study has a critical vent pressure of 158 kPa, which was determined experimental and estimated based on the measurement from a load cell as described below. Immediately after venting, the pressure drops significantly and the generated gas is released. During the first venting event, the gas and some electrolyte will be ejected to the outside. The loss of electrolyte in the cell will lead to changes of the cell properties. This can be observed as an increase in resistance and loss of active materials [31]. This study only focuses on the cell behavior before first venting.

The total internal pressure of the cell includes two components: first, pressure

from the evaporation of electrolyte, which is equal to the vapor saturation pressure; second, pressure from the generated gas. The cell internal pressure P_{total} can be expressed as

$$P_{total} = P_{sat} + P_{CO_2} \tag{5.3}$$

where P_{sat} is the saturation pressure of the electrolyte vapor, and P_{CO_2} is the pressure from the CO_2 generated during SEI decomposition. The saturation pressure of the electrolyte vapor can be expressed by using the Antoine equation [109]

$$log(P_{sat}/kPa) = A - \frac{B}{T/K + C} \tag{5.4}$$

where T represents temperature in K, and the Antoine coefficients for dimethyl carbonate (DMC) and ethylene carbonate (EC) are shown in Table. 5.1

Table 5.1: Antoine coefficients of the pure electrolyte

Component	A	B	C
DMC [109]	6.4338	1413.0	-44.25
EC [109]	6.4897	1836.57	-102.23

For systems with mixed electrolyte components of EC and DMC, the saturation pressure can be expressed by adding the partial pressure of each component

$$P_{sat} = y_{EC} \cdot P_{sat,EC} + y_{DMC} \cdot P_{sat,DMC} \tag{5.5}$$

where the y_{EC} and y_{DMC} refer to the molar fraction of EC and DMC in the electrolyte, and in this cell $y_{EC} = 30\%$, $y_{DMC} = 70\%$. $P_{sat,EC}$ and $P_{sat,DMC}$ represent the saturation pressure for pure component calculated in Eq. 5.4. The assumption that the system is in equilibrium at the saturation pressure is valid only when the system is closed. After the venting, the pressure drops and the equation does not hold true. To this end, we will only consider the gas pressure before the gas venting.

The P_{CO_2} is the gas pressure from the generated CO_2. The partial pressure P_{CO_2} can be calculated using the ideal gas law

$$P_{CO_2} = \frac{n(CO_2)RT}{V_h} \tag{5.6}$$

where $n(CO_2)$ is the generated amount of CO_2 in moles, R is the ideal gas constant, and V_h is the volume of headspace of the cell, corresponding to the volume of gas in the cell. The volume of headspace varies for each cell. As an example, for a 18650

cylindrical cell in [24], V_h is 7% of the total cell volume. For this study, we consider a vacuum-sealed pouch cell, which has room to expand before the internal pressure begins to build. Once the free volume $V_{h,0}$ is filled, the increase in internal pressure deforms the surface of the pouch primarily in the direction perpendicular to the plane of the separator due to the aspect ratio and cell construction. The total volume for gas V_h can be estimated by

$$V_h = V_{h,0} + A_{surf} \times (\Delta d - \alpha_{cell} \cdot \Delta T) \tag{5.7}$$

where $V_{h,0}$ is the volume of headspace before the cell surface area deforms, and is estimated using direct measurements of the pouch cell. The pouch cell initial headspace volume can be estimated by measuring the dimensions of the electrode and the cell sealing edges, as shown in Fig. 5.2.

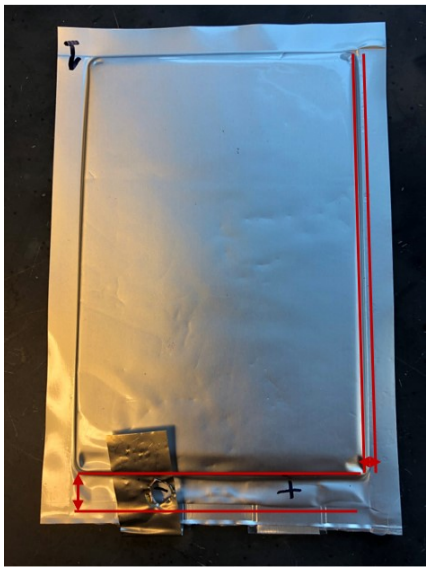

Figure 5.2: Headspace measurement for the pouch cell. The red lines indicate the widths of headspace areas. $V_{h,0}$ can be estimated using the measured headspace area and the cell thickness. This pouch cell's headspace volume is estimated to be 13.5% of total cell volume.

The second term in Eq. 5.7 represents the increased volume due to gas generation minus the thermal swelling of the active material, where A_{surf} is the cell surface area, Δd is the change in cell thickness, and ΔT is the change of cell temperature from the initial ($\Delta T = T - T_0$). The internal cell pressure is balanced by the pressure on surface of the pouch. The change in cell thickness Δd can be expressed as

$$\Delta d = L \, \frac{\Delta \sigma}{E} \tag{5.8}$$

where E and L are the Young's modulus and nominal thickness of poron sheets, respectively. $\Delta\sigma$ is the increased compression stress in the fixture due to gas pressure and thermal expansion of the battery, and can be expressed as

$$\Delta\sigma = \max\left(P_{total} - \sigma_0 - P_{atm}, \frac{E \cdot \alpha_{cell} \cdot \Delta T}{L}\right) \tag{5.9}$$

where α_{cell} represents the cell thermal expansion coefficient, σ_0 represents the initial compression stress in the fixture, and P_{atm} represents the atmospheric pressure. At the early stage, the cell is under-inflated, and P_{total} is smaller than the initial compression stress and atmospheric pressure, so a max operator is used to ensure $\Delta\sigma$ equals the thermal expansion term before the gas pressure builds and breaks contact.

When the cell internal pressure exceeds the critical pressure P_{crit}, cell rupture or gas venting will occur. The critical vent pressure of the pouch cell can be measured using the maximum measured expansion force F_{max}, the contact area between cell and fixture A_{surf} and the atmospheric pressure P_{atm}.

$$P_{crit} = \frac{F_{max}}{A_{surf}} + P_{atm} \tag{5.10}$$

The critical vent pressure for the pouch cell will be based on experimental measurements discussed in the next section.

A summary of the model parameters used is listed below, and the detailed specifications for the pouch cell including anode and cathode mass can be found in the Appendix.

Table 5.2: Summary of first venting model parameters

Parameter	Value	Unit	Physical Meaning	Source
A_{SEI}	2.25×10^{15}	s^{-1}	Frequency factor for SEI decomposition	[32]
E_{SEI}	2.24×10^{-19}	J	Activation energy for SEI decomposition	[32]
$x_{SEI,0}$	0.15	-	Initial fraction of Li in SEI	[32]
M_{C_6}	72	g/mol	Molar mass for C_6	-
m_{an}	19.1	g	Anode mass	From Manufacturer
$V_{h,0}$	6.65×10^{-6}	m^3	Initial volume of headspace	Measured
A_{surf}	0.009	m^2	Contact area between cell surface and fixture	Measured
L	2.4	mm	Thickness of two Poron sheets	Measured
E	0.19	MPa	Young's modulus for Poron sheets	Measured
α_{cell}	1.1	$\mu m/K$	Cell thermal expansion coefficient	[110]
P_{atm}	101	kPa	Atmospheric pressure	-
P_{crit}	158	kPa	Critical vent pressure	Measured

5.3 Experimental Validation for First Venting Model

Most of the previous published works used gas chromatography for gas component analysis [75, 76], which provides detailed compositions of the vent-gas but the measurements are usually taken at the end of the test. Since the organic solvent in the leaked electrolyte can also react with oxygen from the environment to form CO_2 and H_2O [72], this will lead to increased CO_2 amount over time, and using this measured value for detection can artificially increase the detection threshold, leading to false negative of gas detection.

For gas detection of cell venting events, the initial amount of CO_2 released at the first venting event is the key parameter. To this end, real-time gas sensor measurements are needed, and an ESC experiment using a 4.6 Ah NMC pouch cell was set up to validate the first venting model from the timing of venting to CO_2 release amount.

5.3.1 External Short Circuit Experiment

The battery used in this experiment was manufactured at the University of Michigan Battery Lab. The pouch cell size is 130 $mm \times 89\ mm \times 5.5\ mm$. The 1 kHz impedance of cell, from EIS testing, was 5.7 $m\Omega$ at 20 °C. The experiment was performed for a fully charged cell (100% SOC).

The short circuit was initiated using a Gigavac GV141BAB DC contactor. When no voltage is applied to the contactor coil, the circuit was open (insulation resistance over 100 $M\Omega$). When a 12 V voltage was applied to the contactor coil, the contactor closed the circuit (electrical resistance only 0.3 $m\Omega$). The short circuit current was measured using a current shunt with 250 A rated maximum current.

The pouch cell was stacked between a garolite plate and an acrylic plate in the fixture with a layer of poron on both sides of the cell, and the schematic for the fixture is shown in Fig. 5.3a. The bolts hold the two end-plates at a fixed distance. An Omegadyne LC305-500 load cell was placed between the plates and used to measure the cell expansion force during ESC experiments.

There were two K-type thermocouples placed on the surface of the cell to measure the surface temperature at the center of the cell and near the cell tabs, as shown in Fig. 5.3b. Similar to the experiment setup in [111], the whole fixture was placed inside an acrylic box, which had a small opening at the back due to the wiring at the bottom.

The voltage, current, cell surface temperature, expansion force, and CO_2 concentration were recorded using a LabVIEW PXI-based data acquisition system. CO_2

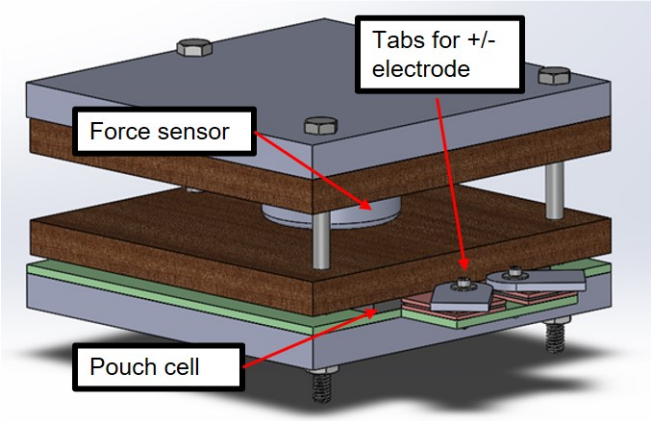

(a)

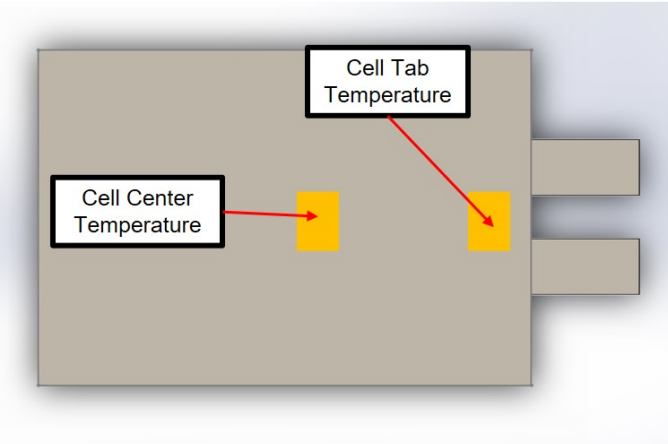

(b)

Figure 5.3: ESC experiment setup (a) Pouch cell was stacked in the fixture, and the cell expansion force was measured (b) K-type thermocouples were used to measure the cell center temperature and cell tab temperature.

concentration was measured using a Telaire T6703 NDIR CO_2 sensor from Amphenol Advanced Sensors with an accuracy of $\pm 10\%$ and updated signal every 5 seconds. The gas sensor was placed adjacent to the fixture.

5.3.2 Experiment Results

During the ESC experiment, gas venting was observed without thermal runaway. After the gas venting event, the release of vent-gas during venting was visible due to the electrolyte vapor, creating a white fume ([95]). The cell voltage, charging current, expansion force, and temperature are shown in Fig. 5.4.

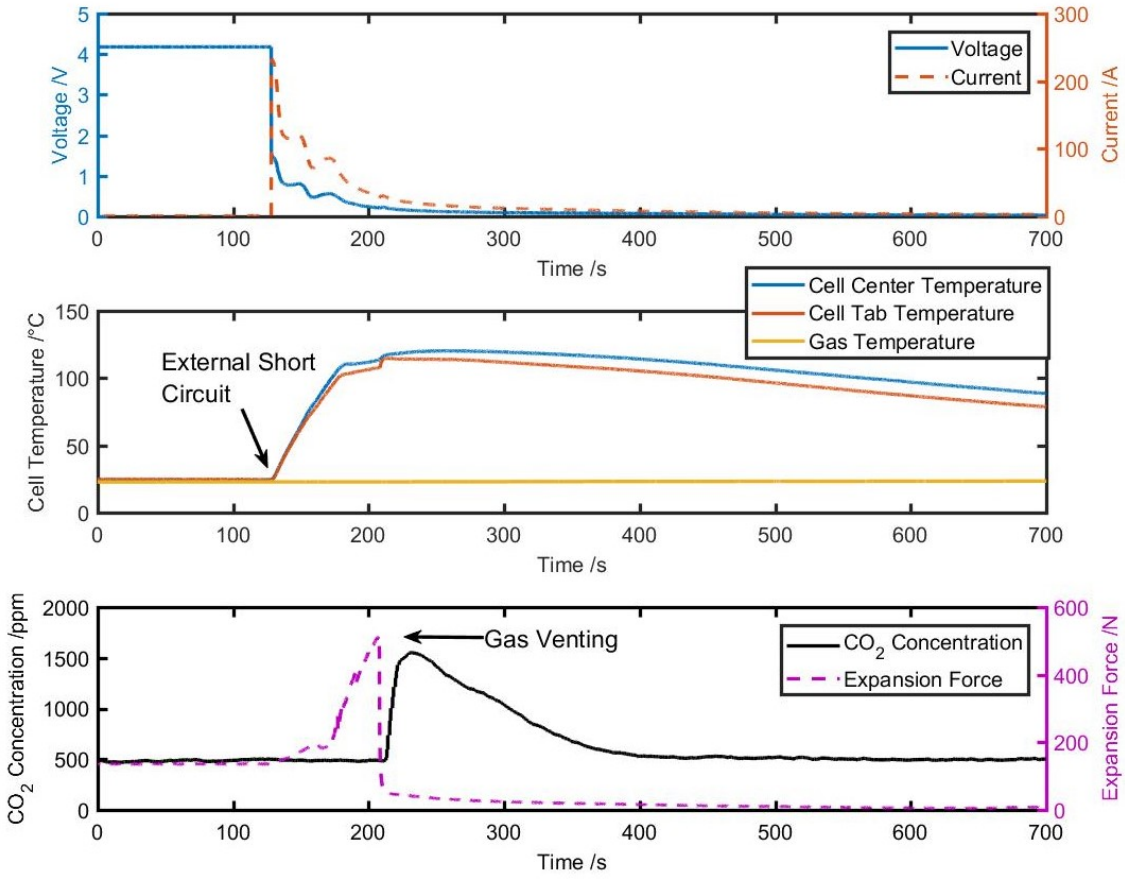

Figure 5.4: Voltage, current, force, temperature, gas and measurements during an ESC experiment are shown. No thermal runaway was triggered in this ESC experiment.

5.3.2.1 Voltage, current and temperature response

The external short started at t=128 s, and the cell terminal voltage dropped to 1.5 V immediately, and slowly decreased to 0.2 V before the venting occurred. The ESC current peaked at the start of the short circuit event, reaching 233 A.

After the initial peak, the current then decreased with time, and the short circuit current was 31 A before the gas venting. After the gas venting event, due to the shortage of electrolyte in the cell, cell internal resistance would increase significantly [31]. According to the EIS testing result after the ESC experiment, the leaked cell's 1 kHz impedance was 163 $m\Omega$, comparing to 5.7 $m\Omega$ before the ESC experiment. Because of the large increase of cell resistance, the short circuit current decreased even further.

The cell temperature started to increase after the initiation of the ESC experiment. The cell surface temperature at the center reached 114 °C before the gas venting event,

and the cell tab temperature was at 108 °C. After the gas venting, the cell center reached a maximum of 120 °C before the cell cooled down.

5.3.2.2 Expansion force and gas response

After the ESC started, the expansion force increased rapidly and reached a peak of 517 N before the gas venting. When the cell ruptured, the expansion force quickly dropped to 50 N at $t = 208\ s$, indicating gas venting.

After the gas venting, the built-up gas was released and the measured CO_2 concentration quickly increased, reaching a peak of 1550 ppm at $t = 230\ s$. Due to the small opening at the back of acrylic box, the vent-gas gradually diffused out of the acrylic box, causing a decline in the CO_2 concentration.

5.3.2.3 Critical vent pressure and gas release

The critical vent pressure and CO_2 gas release amount can be estimated by using the available force and gas sensor measurements.

For determining the critical vent pressure, the maximum expansion force was 517 N, and the contact area between cell and fixture A_{surf} was 0.009 m^3. Therefore the critical vent pressure for the pouch cell from Eq. 5.10 is estimated to be 158 kPa.

The amount of CO_2 gas released can be estimated using the maximum measured CO_2 concentration in the acrylic box (1550 ppm). Since the atmospheric CO_2 concentration is 400 ppm, then the increased CO_2 concentration ($\Delta c(CO_2)_{max}$) is 1150 ppm. The acrylic box has a volume of 21.5 L. The fixture, battery, and sensor have a total volume of 3.1 L, leaving 18.4 L of ambient air volume inside the acrylic box ($V_{air} = 18.4\ L$). By using the increased CO_2 concentration and the ambient air volume, neglecting the gas that escaped the box, and assuming the CO_2 reached equilibrium, we can roughly estimate the volume of CO_2 ($V(CO_2)_{exp}$) to be 20 mL.

$$V(CO_2)_{exp} = \frac{\Delta c(CO_2)_{max}\ [ppm]}{10^6\ [ppm]} \times V_{air}\ [L] = 20\ mL \tag{5.11}$$

At room temperature and atmospheric pressure, from ideal gas law, the amount of CO_2 released from experiment $n(CO_2)_{exp}$ can be derived. For the equation below, P_{atm} is the atmospheric pressure ($P_{atm} = 10^5\ Pa$), R is the ideal gas constant ($R = 8.314\ m^3 \cdot Pa \cdot K^{-1} \cdot mol^{-1}$), and T is the room temperature ($T = 298\ K$). The amount of CO_2 released from the experiment was approximated to be 0.8 mmol.

$$n(CO_2)_{exp} = \frac{V(CO_2)_{exp} \cdot P_{atm}}{RT} = 0.8\ mmol \tag{5.12}$$

This value here is an approximation because of the following assumptions: 1. We neglect the vent-gas that escaped from the box in the first 20 seconds. 2. We assume the vent-gas mixes well in the box and CO_2 concentration has reached an equilibrium in the box.

5.3.3 Comparing Model with Experiment

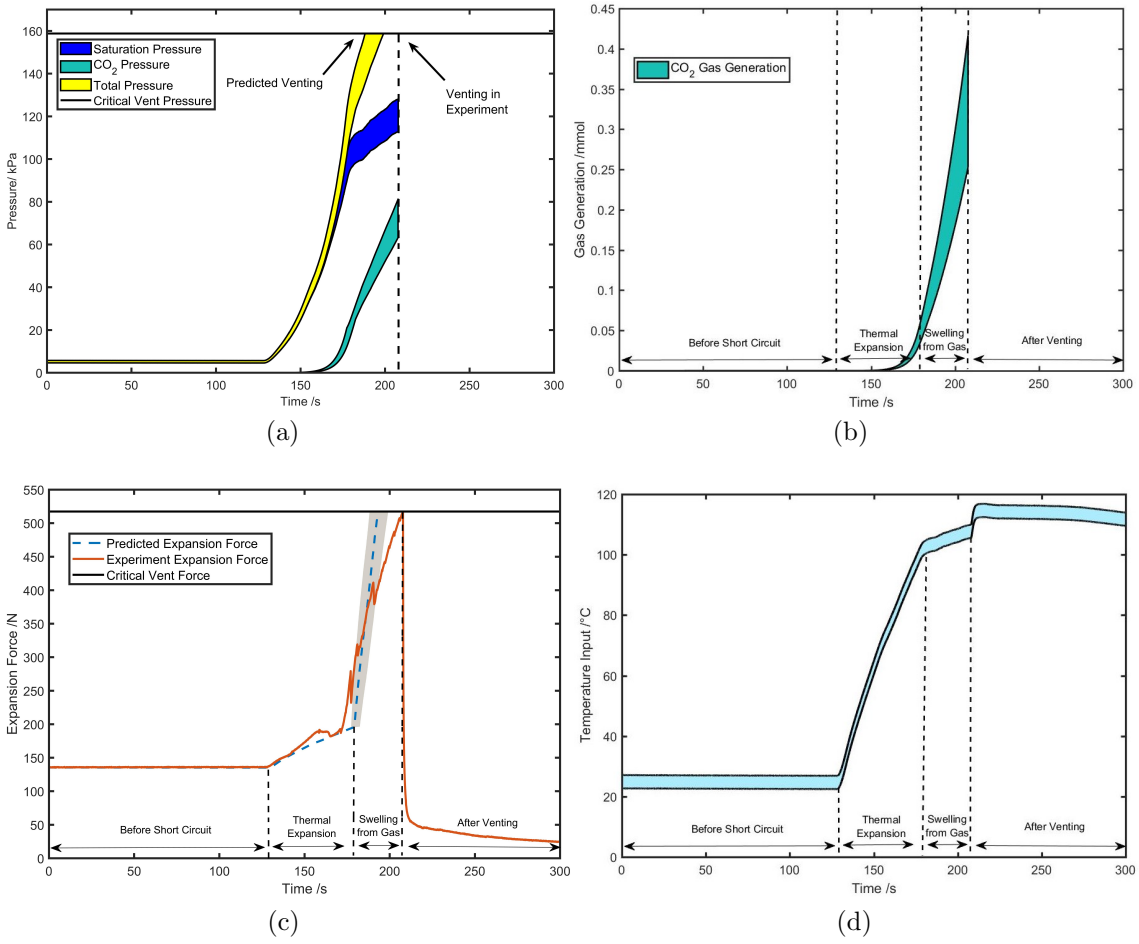

Figure 5.5: Model prediction for the ESC experiment, the shaded region corresponds to model outputs after considering temperature measurement errors. (a) Cell internal pressure, which is composed of saturation pressure and gas pressure. The gas venting occurs when the pressure exceeds the critical vent pressure. (b) CO_2 gas generation before the cell venting occurs. (c) Battery expansion force before cell venting, compared with experiment measured expansion force. (d) Temperature input to the model with ± 2.2 degrees from the measured value.

The measured temperature from the experiment will be used as model input, and the first venting time and amount of gas generation are the model outputs. These

outputs in addition to the predicted battery expansion force, will be compared with the experiment measurements.

The measured cell tab temperature is used as the temperature input, because the gas venting happened near the cell tab area. Since the K-type thermocouples have an accuracy of $\pm 2.2\ ^{\circ}C$, and the model outputs of gas generation and pressure are highly sensitive to temperature inputs, therefore the model predictions of the ESC experiment include confidence bounds based on the temperature intervals.

The first venting model predicts that venting will occur between $t = 187\ s$ and $t = 199\ s$. The experiment shows that the venting occurred at $t = 208\ s$. This discrepancy might come from the error in the modeled temperature. The generation rate of gas is strongly temperature dependent, and small errors in the modeled temperature can result in large difference in predicted venting times. Further more, the frequency factor and activation energy were taken from [32], and correspond to a slightly different anode formulation. These parameters could be tuned to better match the timing of cell venting in the experiment.

The cell expansion measurement can be used to infer the gas generation during the initial phases of cell failure before the venting. The model predicts the two slopes in measured load prior to the first venting event, as shown in Fig. 5.5c, the short circuit process can be separated into four regions: 1, before short circuit. 2, thermal expansion. 3, cell swelling from gas. 4, after venting. For the second stage, the thermal expansion stage, the initial relatively slow increase in force is due to the thermal expansion of the active material. Then at the third stage, once the generated gas has filled the headspace and overcomes the combined pre-load and thermal expansion force within the fixture, the swelling due to the generated gas causes a faster increase in force. At the fourth stage, after the cell venting, the expansion force drops suddenly.

Table 5.3: CO_2 Gas Generation from Model Prediction and Experiments (mmol)

Model			Experiment
CO_2 before venting	CO_2 after venting	Total CO_2	Total CO_2
0.25 - 0.42	0.35 - 0.55	0.6 - 0.97	0.8

After venting, the CO_2 gas concentration is used for quantifying the progression of the reaction. The experiment measured CO_2 concentration reflects the total gas release, which includes the gas generated before cell venting and after venting. The model predicts the amount of CO_2 before venting, and the total amount of CO_2 can be predicted by continuing the SEI decomposition reaction in the model beyond venting

for comparison with experimental data. The results are summarized in Table. 5.3, and the model generally matches with the experimental release results.

5.4 Simulating Single Cell Thermal Runaway

After modeling the cell venting events and the CO_2 gas release in the first venting, we can now simulate a single cell thermal runaway and estimate the amount of CO_2 gas release in a thermal runaway event. The thermal runaway model for a 18650 cell will be based on [35], and includes a lumped thermal model, an electrical model for short circuit ohmic heat, and a side reaction model for exothermic reaction heat.

5.4.1 Lumped Thermal Model

For the thermal model, earlier studies [12, 32] have used lumped thermal models to describe battery temperature during thermal runaway. The lumped thermal model assumes a uniform temperature distribution and one temperature state to represent the whole cell. Cai et al. [35] addressed the importance of having multiple temperature states in the thermal model in cases of a local internal short circuit. In this chapter, we focus on a massive internal short circuit event, where we assume the short circuit ohmic heat distributes evenly across the cell. To simplify the analysis of single-cell thermal runaway, a lumped thermal model will be used for the cell triggering thermal runaway.

$$C_{p,cell} m_{cell} \frac{dT_{cell}}{dt} = (\dot{Q}_{exo} + \dot{Q}_{ohmic}) + \frac{T_{amb} - T_{cell}}{r_{c2a}} \tag{5.13}$$

where T_{cell} and T_{amb} represent the cell temperature and atmospheric temperature respectively and r_{c2a} is the thermal resistance between the cell and atmosphere.

The heat source term $\dot{Q}_{exo}$ is the side reaction heat from SEI decomposition, anode decomposition and cathode decomposition [32, 35]. The other heat source term $\dot{Q}_{ohmic}$ represents the short circuit ohmic heat.

5.4.2 Short Circuit Model

During a thermal runaway event, the battery short circuit will produce a significant amount of heat. This study focuses on the massive internal short circuit that occurs in a fully charged battery and finally leads to thermal runaway. The battery short circuit process can be represented by an equivalent circuit model, and the

terminal voltage can be represented as

$$V_T = U(SOC) - I \cdot R_{cell} \tag{5.14}$$

where I is the short circuit self-discharge current. R_{cell} is the cell internal resistance and $U(SOC)$ is the battery open-circuit voltage (OCV). Similar to Chapter 2, the OCV is a function of SOC.

An equivalent circuit model can be developed to describe the internal short circuit process. In this simulation for a massive internal short circuit case, for convenience, we assume the short circuit resistance is zero ($R_{short} = 0$). The short circuit current can be found using Kirchoff's laws directly for the simple circuit.

$$I_{short} = \frac{U(SOC)}{R_{cell}} \tag{5.15}$$

The heat release due to self discharge is given by,

$$\dot{Q}_{ohmic} = I_{short}^2 R_{cell} \tag{5.16}$$

Following the assumption of the lumped thermal model, the ohmic heat $\dot{Q}_{ohmic}$ distributes evenly in the whole battery, so the whole cell temperature is elevated due to the short circuit process.

5.4.3 Exothermic Reactions and Gas Evolution Model

The major exothermic reactions during a thermal runaway include SEI decomposition, anode decomposition, and cathode decomposition [12]. The side reaction model is the same as described in Chapter 2.

In the previous discussions of this chapter, the gas evolution process is modeled and the first venting happens when the cell internal pressure exceeds the critical vent pressure. For commercial 18650 cells, it usually features a higher critical vent pressure (around 1224 kPa [24]). In a thermal runaway event triggered by a massive internal short circuit, the temperature rise is very fast and the SEI decomposition can finish within few seconds.

Based on this, we assume the released CO_2 in the first venting event all come from SEI decomposition. The estimated gas release will be used for simulating gas detection of a thermal runaway event.

Table 5.4: Thermal runaway model parameters for 18650 cell

Parameter	Value	Unit	Physical Meaning
A_{an}	2.5×10^{13} [32, 42]	s^{-1}	Frequency factor for anode decomposition
A_{ca}	2.55×10^{14} [42]	s^{-1}	Frequency factor for cathode decomposition
A_{SEI}	2.25×10^{15} [42]	s^{-1}	Frequency factor for SEI decomposition
C	2.4	Ah	Capacity of the 18650 cell
$C_{p,cell}$	830 [22]	$J\ kg^{-1}\ K^{-1}$	Specific heat capacity of cell
E_{an}	2.24×10^{-19} [32, 42]	J	Activation energy for anode decomposition
E_{ca}	2.64×10^{-19} [42]	J	Activation energy for cathode decomposition
E_{SEI}	2.24×10^{-19} [32, 42]	J	Activation energy for SEI decomposition
h_{an}	1714 [32, 42]	$J\ g^{-1}$	Enthalpy of anode decomposition
h_{ca}	790 [42]	$J\ g^{-1}$	Enthalpy of cathode decomposition
h_{SEI}	257 [32, 42]	$J\ g^{-1}$	Enthalpy of SEI decomposition
k_{cell}	3.4, 3.4, 28 [32]	$W\ m^{-1}\ K^{-1}$	Thermal conductivity of cell
m_{an}	8.1	g	Mass of anode
m_{ca}	18.3	g	Mass of cathode
m_{cell}	42.9	g	Total mass of cell
r_{c2a}	23.9	$K\ W^{-1}$	Thermal resistance between cell and atmosphere
R_{cell}	15	$m\Omega$	Cell internal resistance
SOC_0	1	-	Initial State of Charge
T_{amb}	20	°C	Ambient temperature
$x_{an,0}$	0.75 [32, 42]	-	Initial fraction of Li in anode for fully charged cell
$x_{SEI,0}$	0.15 [32, 42]	-	Initial fraction of Li in SEI
z_0	0.033 [32, 42]	-	Initial dimensionless SEI thickness
α_0	0.04 [32, 42]	-	Initial degree of cathode decomposition conversion

5.4.4 Results of Thermal Runaway Simulation

Given the major components of a single cell thermal runaway model, a simulation will be presented here for an internal short circuit of a 18650 NMC Li-ion cell. In this simulation, short circuit resistance will be neglected for simplicity. The model parameters for single-cell thermal runaway are shown in Table 5.4.

The evolution of battery temperature is shown in Fig 5.6a. It is clear that the battery experienced a thermal runaway event and the maximum temperature reached over 800 °C.

The amount of initial gas generation by SEI decomposition is shown in Fig 5.6b. According to the simulation result, there will be 7.5 mmol CO_2 as the first venting gas. This result generally agrees with the previous experimental results, which indicated CO_2 release ranges from 1.6 to 6.2 mmol in first venting events for 18650 cell [37].

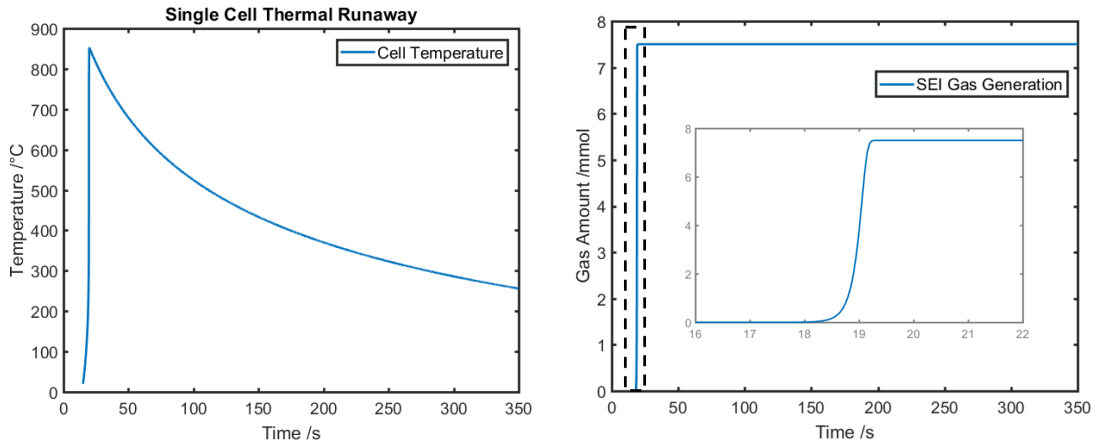

(a) (b)

Figure 5.6: (a) Single cell thermal runaway temperature; (b) First venting gas from SEI decomposition

5.5 Critical Timeline of Detection Before Thermal Runaway Propagation

After the first cell triggering a thermal runaway, the neighboring cells and the drum will be heated. The challenge arises when the neighboring cells reach critical temperatures, these cells will also trigger thermal runaway [108].

In this study, the thermal runaway propagation follows the single-cell thermal runaway event described in the previous section. The critical time of thermal runaway propagation is the time when the second cell triggers thermal runaway. To prevent thermal runaway propagation, it is important to detect a thermal runaway event before the critical time.

In this thermal runaway propagation simulation, a set of cells are placed in parallel and series to represent a typical laptop battery, as shown in Fig. 5.7a. The thermal runaway propagation is simulated with cells not in direct contact, and the heat is propagated through the air in this simulation.

The cell in the center (cell #5) triggers thermal runaway, leading neighboring cells to thermal runaway. The governing equation for this heat propagation process is

$$\rho C_p \frac{\partial T}{\partial t} + \rho C_p u \cdot \nabla T - K \nabla^2 T = Q \tag{5.17}$$

where ρ is the density, C_p is the heat capacity, T is the temperature, u is the convective flow velocity, K is the thermal diffusivity and Q is the heat generation. We can separate the simulation into two domains, battery and air. In the battery

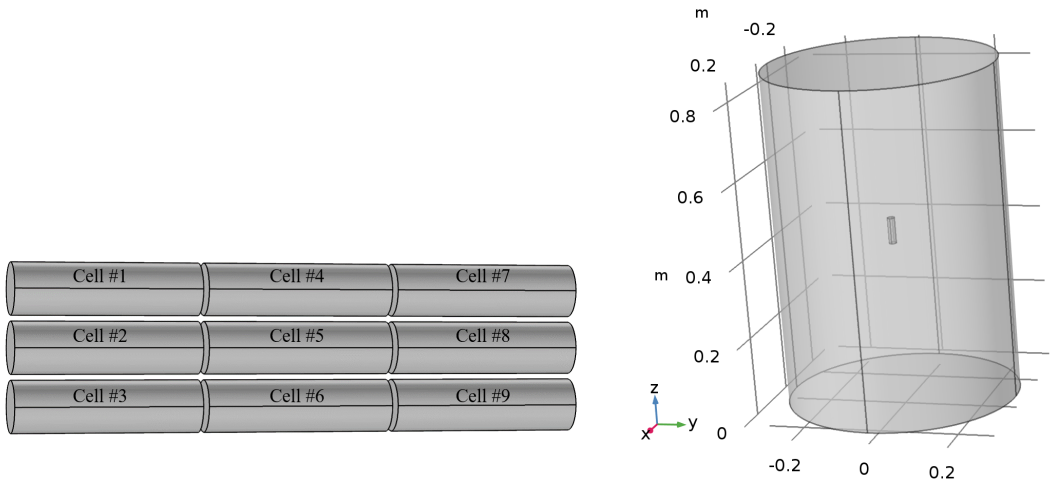

(a) (b)

Figure 5.7: (a) Cell placement during thermal runaway propagation; (b) Drum with thermal runaway cell in center

domain, the $\rho_{cell}C_{p,cell}\frac{\partial T_{cell}}{\partial t}$ term represents the internal energy temporal evolution of battery, Q_{cell} represents the battery heat generation. We assume $u = 0$ inside the battery, and the heat can propagate due to the thermal diffusion term $K_{cell}\nabla^2 T_{cell}$. In air domain, the $\rho_{air}C_{p,air}\frac{\partial T_{air}}{\partial t}$ term represents the air temperature change, $\rho_{air}C_{p,air}u \cdot \nabla T_{air}$ represents convection term in air domain, $K_{air}\nabla^2 T_{air}$ represents diffusion term in air, and there is no heat generation term Q in air domain.

This process is simulated in the COMSOL heat transfer module. The heat source is the battery thermal runaway heat from the single-cell model. Fig 5.8a-5.8d shows the process of cell surface temperature change before and after the second cell triggering thermal runaway.

Fig. 5.9 shows the temperature for each cell from the first cell thermal runaway to the end of propagation. To be noticed, the difference of peak temperatures in Fig. 5.9 and the previous single-cell result is due to different boundary conditions of heat transfer. The critical time for the second cell to trigger a thermal runaway is around 710 seconds. Thermal runaway propagation critical time (t_{crit}) for this case is then 710 seconds. Detection for a thermal runaway event is needed before propagation critical time, so the hazard of a chain reaction can be avoided.

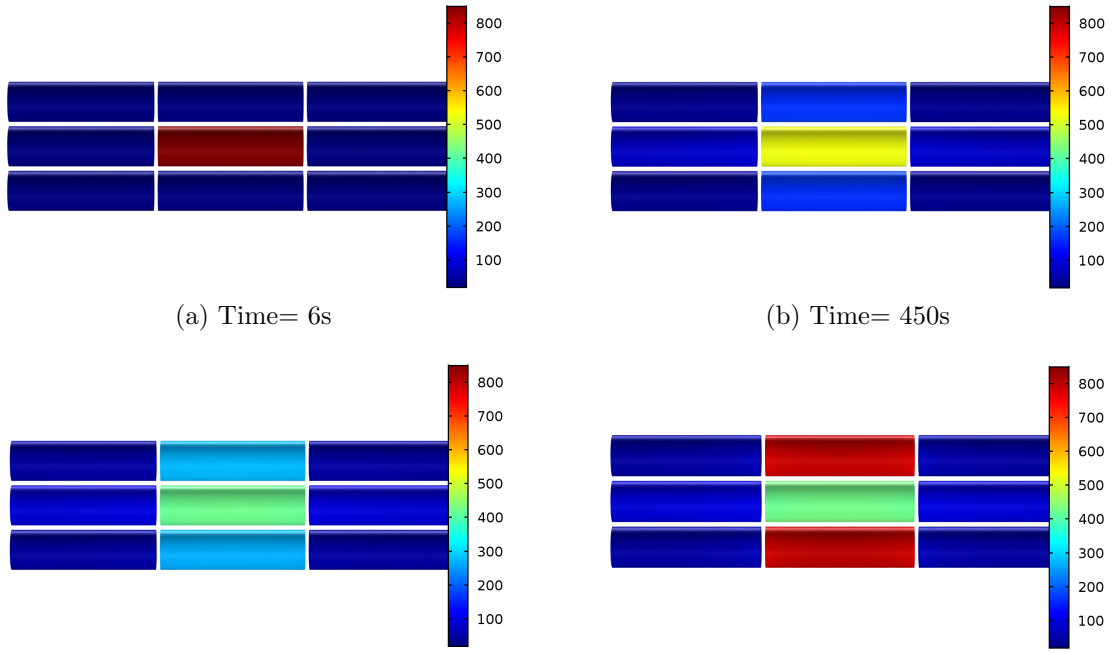

(a) Time= 6s (b) Time= 450s

(c) Time= 690s (d) Time= 710s

Figure 5.8: Cell surface temperature distribution (°C)

5.6 Thermal Runaway Detection in Battery Storage Drums

In this part, two detection methods using surface temperature monitoring and gas sensing will be analyzed, focusing on a thermal runaway event inside a cylindrical drum. The cylindrical drum has a radius of 0.292 m and height of 0.85 m, as shown in Fig 5.7b. The drum center coordinate is (0, 0, 0.425 m).

The small cylinder in the center of the drum represents the initial thermal runaway cell and is located at the center of the drum. The cell center coordinate is (0, 0, 0.425 m). In this study, the drum is a mix of batteries and air, and its lumped thermal parameters are measured by the drum heating test. The thermal parameters of the drum are included in Table. 5.5.

5.6.1 Detection Based on Drum Surface Temperature

First, a drum surface temperature sensor is used to monitor potential thermal runaway events inside the drum. The temperature sensor coordinate is (0.292 m, 0, 0.425 m). The detection time will then be compared with the thermal runaway critical time t_{crit}.

Fig. 5.10a shows the drum temperature distribution of cross-sectional plane at $z = 0.425\ m$ when $t = 710\ s$. It is clear that with the large thermal mass of the

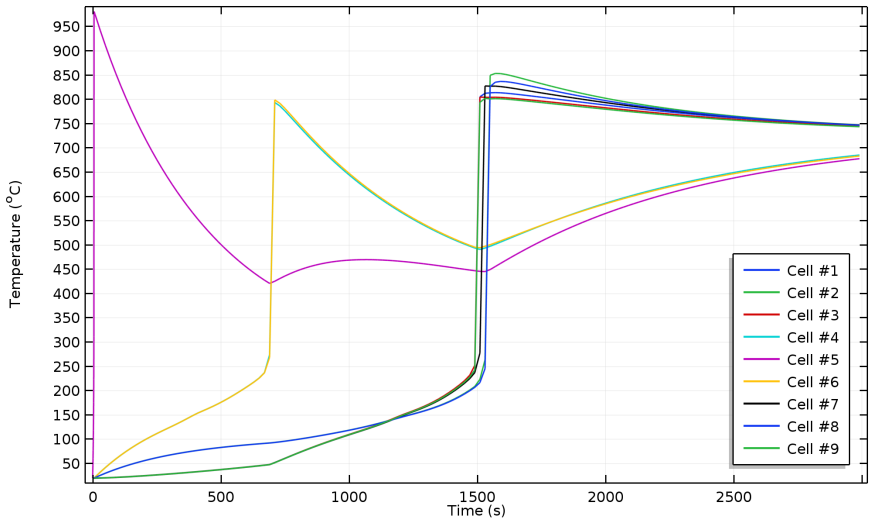

Figure 5.9: Cell Temperature During Thermal Runaway Propagation

Table 5.5: Storage drum parameters

Parameter	Value	Unit	Physical Meaning
ρ	2580	$kg\ m^{-3}$	Density of drum mix
ϵ	0.25	-	Porosity of drum mix
$C_{p,drum}$	650	$J\ kg^{-1}\ K^{-1}$	Heat capacity of drum mix
H_{drum}	0.85	m	Height of drum
λ_{drum}	1.2	$W\ m^{-1}\ K^{-1}$	Thermal conductivity of drum mix
R_{drum}	0.292	m	Radius of drum

drum, the surface temperature change on the drum is subtle. In this simulation, at $t = 710\ s$, the surface temperature change is less than 0.001 °C and this small change can hardly be detected with a temperature sensor. After $t = 710s$, with neighboring cells triggering thermal runaway, any detection after that is considered too late.

In conclusion, the surface temperature sensor cannot detect such subtle changes during a thermal runaway event before propagation critical time. When the surface temperature measurement detects the thermal runaway, the thermal runaway has already propagated to neighboring cells, causing even more damage. Therefore, a fast and robust thermal runaway detection method is needed for large-scale battery storage applications.

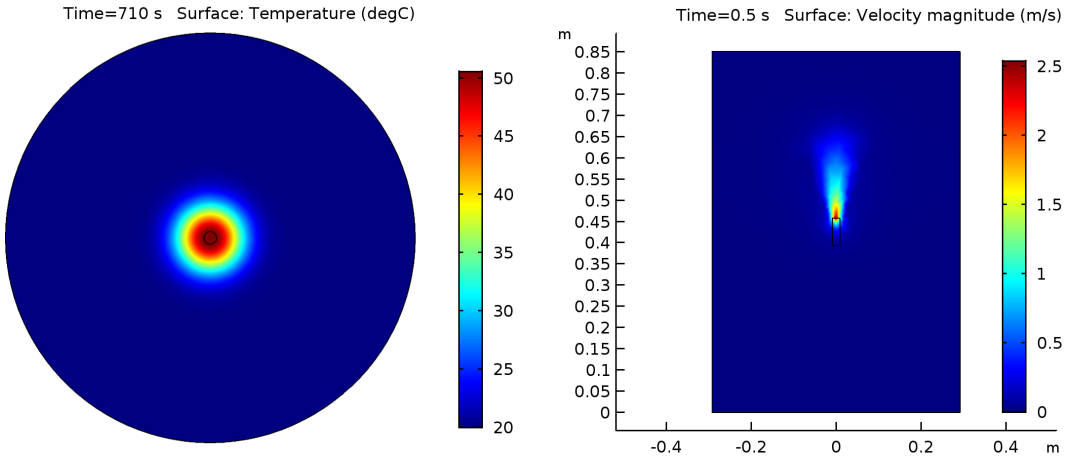

(a) (b)

Figure 5.10: (a) Temperature distribution at 710s; (b)Cross-sectional view of vented gas velocity

5.6.2 Detection Based on Gas

Monitor the air inside the drum allows faster detection because the airflow is faster than the heat propagation speed of solid materials. To monitor the air, one can measure the air temperature or detect vented gas concentrations. However, for the first approach, measuring air temperature, the hot vented gas can only elevate the average air temperature with less than 1°C after sufficient mixing of air in the drum. Detection based on CO_2 concentrations will be more robust, because there is a significant change of average CO_2 concentrations after the thermal runaway. To demonstrate the effectiveness of gas detection, a CO_2 gas sensor will be placed at the center of the drum top, with coordinate (0, 0, 0.85 m).

Following the result from previous sections, during the first cell thermal runaway, 7.5 mmol CO_2 will be released. This study will focus on the gas flow for this 7.5 mmol CO_2, which is used for thermal runaway detection. The gas flow of CO_2 will be simulated in a 55 gallon (0.208 m^3) cylindrical drum. Initial gas venting speed can be approximated by the amount of gas vented and the duration of venting from the single-cell modeling result, and the estimated average venting speed is 1.5 m/s. The estimated venting speed generally agrees with the experimental measurements in [104] and the analysis in Chapter 4.5. Fig. 5.10b shows the initial speed of vented gas in the simulation.

This gas flow process is simulated in COMSOL, using the module Transport of Diluted Species in Porous Media. The simulation settings for transport mechanisms

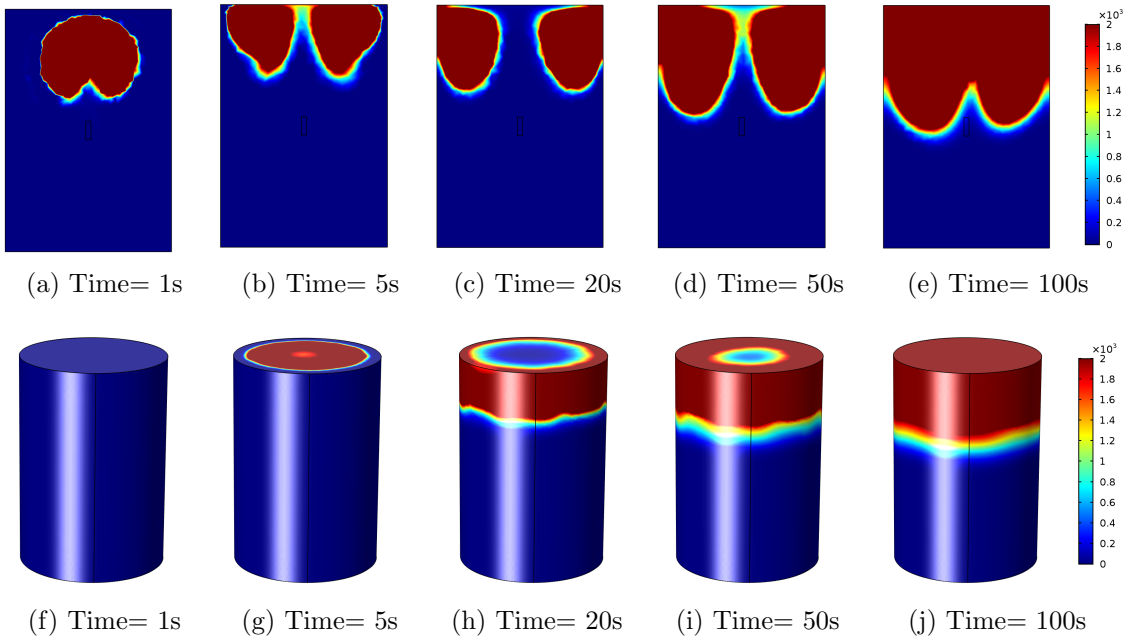

(a) Time= 1s (b) Time= 5s (c) Time= 20s (d) Time= 50s (e) Time= 100s

(f) Time= 1s (g) Time= 5s (h) Time= 20s (i) Time= 50s (j) Time= 100s

Figure 5.11: CO_2 concentrations in ppm. (a-e) Cross-sectional view at x=0; (f-j) Surface concentrations

include convection and mass transfer in porous media. The laminar flow module is used to simulate the initial gas venting speed.

The gas sensor readings for CO_2 concentrations determine the presence of a thermal runaway event. Considering the atmospheric CO_2 concentration is 400 ppm, a reasonable CO_2 concentration threshold of 2000 ppm is set. If the CO_2 gas detector reading exceeds 2000 ppm for more than 10 seconds, then a thermal runaway event is believed to happen.

Fig. 5.11 shows the simulation result of drum gas flow after the gas venting. The distribution of CO_2 concentrations in ppm is shown in both cross-sectional view and drum surface view. The red region corresponds to areas with CO_2 concentrations larger than 2000 ppm and will be able to trigger the alarm. It is clear that after 100 seconds of the first cell thermal runaway, the vented gas will propagate to most areas in the upper part of the drum.

By using gas sensing for thermal runaway detection in this simulation, as shown in Fig. 5.12, the thermal runaway can be detected at 85 seconds, which is ahead of the thermal runaway critical time ($t_{crit} = 710s$).

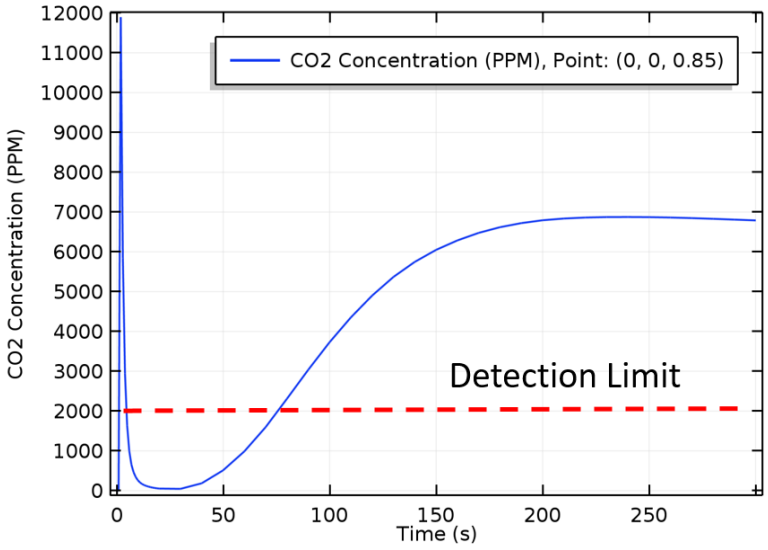

Figure 5.12: CO_2 Gas sensor reading in simulation

5.7 Summary

This chapter addresses the modeling of cell venting and gas detection in a battery storage drum. The cell venting process is modeled through CO_2 gas generation and cell internal pressure. The CO_2 gas evolution model is then used in the simulation of single-cell thermal runaway.

In the scenario of thermal runaway in a battery storage drum, due to close cell placement, a single cell thermal runaway will heat neighboring cells, leading to thermal runaway propagation. The simulation shows that neighboring cells will initiate thermal runaway after 710 seconds of the first thermal runaway event, and this time is defined as the critical time for thermal runaway propagation. Detection before propagation critical time is needed to take immediate emergency responses.

The main focus of this study is on the timing of thermal runaway detection. Two methods for thermal runaway detection have been simulated through COMSOL. By using drum surface temperature measurement, detection of thermal runaway cannot be made before 710 seconds. By switching to gas sensing, detection of thermal runaway can be made at 85 seconds, due to the fast gas flow. While the temperature-based method is too slow for detection, the gas sensing method will enable early detection for thermal runaway.

CHAPTER VI

Fault Detection for Batteries Connected in Parallel

6.1 Introduction

For batteries connected in parallel, voltage-based detection methods will suffer poor signal-to-noise ratio, therefore novel methods are required to achieve immediate and high confidence detection.

For internal short circuit events that evolve without going into thermal runaway, as described in Chapter 2, cell surface temperature increase is limited [52] and the fault is even more difficult to detect by conventional methods using voltage and temperature measurements. If left undetected, the cell might develop into a thermal runaway after continuous use [23]. This type of event features a fast drop and quick recovery of the voltage and is named the "Fusing Phenomenon" in [23]. In this internal short, the high temperature in the ISC region will trigger battery side reactions, which produce a large amount of gas [52]. The generated gas leads to the swelling of the pouch cell that can be measured as a sudden increase in expansion force at the module level. The generated gas will be released in the event of a rupture that elevates the CO_2 concentration level inside the battery module. The CO_2 level can be measured using a gas sensor inside the battery module.

The goal of this chapter's study is to develop a high confidence short circuit detection method based on the measurement of cell expansion force and CO_2 level in a parallel-connected module. To this end, we have developed an observer for the cell expansion in normal operating conditions to detect battery faults from force measurement. Furthermore, a CO_2 gas sensor is used to detect abnormal gas concentration spikes. The results indicate that in the absence of voltage measurements, the proposed algorithm can detect a hard short circuit quickly in a battery module by monitoring force and gas levels.

6.2 Modeling Battery Internal Short in Parallel Circuits without Thermal Runaway

The internal short circuit model follows Chapter 2. Since this chapter focuses on internal short circuit without thermal runaway (as described Test two case in Chapter 2), a simplified model based on Chapter 2 will be presented for a battery module connected in parallel.

6.2.1 Overview of the Parallel-connected Module

For electric vehicle packs, cells are connected with up to 74 cells in parallel, like in the Tesla Model S. Here, we consider a battery module with 50 cells connected in parallel electrically. Each cell in this battery module is a NMC prismatic pouch 4.5 Ah cell. A schematic of the parallel-connected battery module is shown in Fig. 6.1.

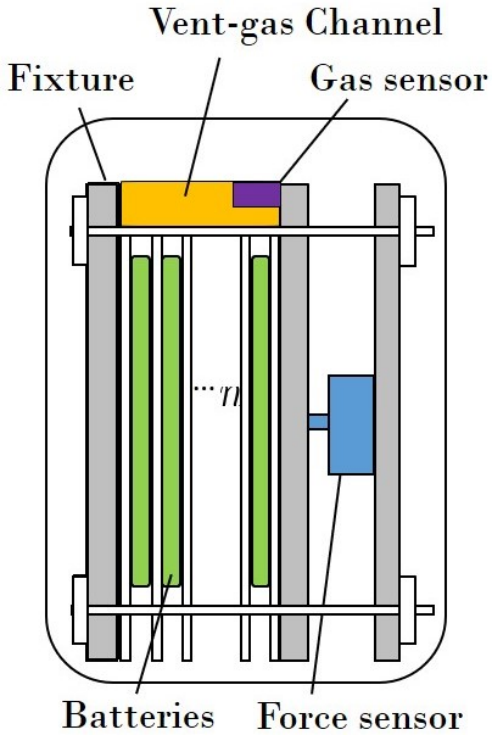

Figure 6.1: The schematic of the battery module with 50 pouch cells connected in parallel. The force sensor is placed at the module end plate and the gas sensor is located in the vent-gas channel.

For automotive battery packs, the cells are typically constrained to a fixed volume as shown in the inset of Fig. 6.1. Therefore swelling of the cell would result in an increase in the cell volume, which would tend to exert a force that is balanced by the

module end plates. This change in force can be measured for multiple cells, which are mechanically connected in series.

A vent-gas channel is located above all cells in the battery module, and vent-gas from any cell will enter the vent-gas channel and leave through the channel outlet. A gas sensor is placed at the vent-gas channel outlet, and can detect possible vent-gas from battery failure.

6.2.2 Terminal Voltage and Thermal Model

For a short circuit in a battery module with n cells in parallel, the equivalent circuit can be represented by Fig. 6.2. Here we assume the capacity for each cell is 4.5 Ah.

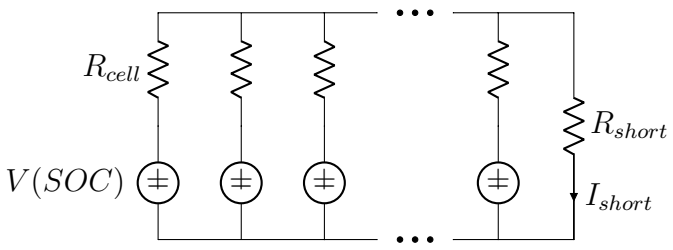

Figure 6.2: Equivalent circuit model representing a battery module with n parallel connected cells and one cell with an internal short circuit.

After triggering an internal short circuit, the major heat source is the ohmic heat from the internal short circuit current. The internal short current for the shorted cell and the terminal voltage can be written as

$$I_{short} = \frac{n \cdot V(SOC)}{R_{cell} + n \cdot R_{short}} \tag{6.1}$$

$$V_T = V(SOC) - I_{short}/n \cdot R_{cell} \tag{6.2}$$

where $V(SOC)$ is the open circuit voltage, which is a function of State of Charge (SOC), V_T is the terminal voltage, I_{short} is the short circuit current, R_{short} is the short circuit resistance, R_{cell} is the cell impedance at 1 kHz, and n is the number of parallel connected cells ($n = 50$ in this case). By substituting Eq. (6.1) into Eq. (6.2), it is clear that for large n, the change in V_T caused by an internal short is reduced.

The localized heating Q_{ohmic} due to the ISC, causes a rapid local temperature increase, while temperature for the rest of the cell remains relatively constant. Above 120 °C the Solid Electrolyte Interface (SEI) decomposition becomes active and starts to generate significant heat [6]. Here, we focus on modeling only the temperature of

the ISC region T_{ISC}, and assume a constant T_{cell} for the rest of the cell. The thermal model from Chapter 2 can be simplified as

$$C_p \frac{dT_{ISC}}{dt} = (Q_{SEI,ISC} + Q_{ohmic,ISC}) + \frac{T_{cell} - T_{ISC}}{R_c} \tag{6.3}$$

$$Q_{ohmic,ISC} = I_{short}^2 R_{short} \tag{6.4}$$

$$Q_{SEI,ISC} = -m_{an,ISC} \cdot h_{SEI} \cdot \frac{dx_{SEI,ISC}}{dt} \tag{6.5}$$

where T_{ISC} and T_{cell} represent the ISC region temperature and the cell temperature respectively. R_c is the thermal resistance between the ISC region and the rest of the cell. C_p is the thermal capacity of the ISC region. $Q_{SEI,ISC}$ is the reaction heat from SEI decomposition. $Q_{ohmic,ISC}$ is the ohmic heat in ISC region, h_{SEI} is the reaction enthalpy of SEI decomposition, and $m_{an,ISC}$ is the mass of anode in the ISC region.

The SEI decomposition reaction rate will increase exponentially with temperature [12], and can be expressed as

$$\frac{dx_{SEI,ISC}}{dt} = -A_{SEI} \cdot x_{SEI,ISC} \cdot \exp\left(-\frac{E_{SEI}}{k_b T_{ISC}}\right) \tag{6.6}$$

where $x_{SEI,ISC}$ is the fraction of Li in the SEI in the ISC region, representing the progress of SEI decomposition. A_{SEI} is the frequency factor for SEI decomposition. E_{SEI} is the activation energy for SEI decomposition, and k_b is Boltzmann's constant.

6.2.3 Expansion Force Model

At normal operating conditions, the cell expansion force can be expressed as a function of temperature and State of Charge (SOC). For a single cell, the change of expansion force is around 156 N or 30% of the total force from a fully discharged to a fully charged state. The peak force due to an internal short circuit event can exceed the sensor capacity (1780 N) and hit the sensor saturation limit of 3560 N [52], which is greater than 10x of the normal expansion force change. Here, we model the expansion force as a separable function of temperature and SOC [55]. Similar to Chapter 3, the expansion force can then be expressed as

$$F = f_1(T) + f_2(SOC) + F_0 + F_{gas} \tag{6.7}$$

where the F_{gas} term is the fault expansion force due to gas generation and F_0 is the preload force. For the SOC dependency of the expansion force, the measurement

experiment uses the same setting as [54]. The cell chemistry is nickel manganese cobalt oxide (NMC), with prismatic structure. Here, an eighth order polynomial fit for the expansion force as a function of SOC is used, similar to Chapter 3.

For the temperature dependence, we assume the expansion force grows linearly with the temperature as

$$f_1(T) = \alpha(T - T_0) \tag{6.8}$$

where T_0 is the initial temperature, and α is the thermal expansion rate. The thermal expansion coefficient α varies with different fixtures and batteries. Here, we calculate it based on the experimental data for the cell during the heating phase. The α in this study is 2.06 $N/^{\circ}C$.

As a result of gas generation, the cell swells and increases the measured expansion force once the gas pressure inside the cell overcomes the preload force. The increased force due to generated gas is modeled using the ideal gas law to convert the number of moles of gas to pressure. We can express the pressure as

$$P = \frac{n_{CO_2} R T_{cell}}{\Delta V} = \frac{F_{gas}}{A_{cell}} \tag{6.9}$$

where ΔV is the change of cell volume occupied by the gas. We assume $\Delta V = A_{cell}\Delta x$, and the deflection of the cell casing is balanced by the increased force from the fixture and compression of adjacent cells $F_{gas} = K_{eq}\Delta x$. An equivalent spring constant of the battery module K_{eq} is used which captures the effects of all other cells in the module. We plug these relationships into Eq. (6.9) to solve for the change in cell thickness Δx in the direction of the applied force.

Hence the fault expansion force F_{gas} can be expressed as

$$F_{gas} = \sqrt{K_{eq} \cdot n_{CO_2} \cdot R T_{cell}} \tag{6.10}$$

Since K_{eq} is the result of a series connection of mechanical springs, it is expected that the value of K_{eq} would decrease as the number of cells in the module increases.

$$K_{eq} \propto \frac{1}{n}$$

$$F_{gas} \propto \sqrt{\frac{1}{n}}$$

The expansion grows rapidly following the gas buildup process. Hard cased cylindrical and prismatic battery cells are designed with a venting structure that will reliably

fail open once the cell exceeds a certain internal pressure to prevent explosive forces due to gas buildup [36]. After the cell ruptures, the fault force drops to zero as a consequence of the release of gas.

6.2.4 Gas Concentration in the Module

As discussed in Chapter 5, during a battery failure event, the SEI decomposition reaction generates gas that can lead to severe cell swelling and venting of gas. The total amount of CO_2 generated can be estimated through SEI decomposition.

After the fault event, the vented gas transport process is fast, and [65] indicated a transport time of 3 seconds for CO_2 sensors. To model the gas sensor response which is located at the vent-gas duct outlet, a 1D mass transport equation is incorporated. The model assumes diffusion and convection processes. Here, we assume the vent-gas velocity prescribes the airflow velocity. The length of the total battery module is assumed 0.5 m. The CO_2 is assumed to be generated at the boundary location ($x = 0$) for the duration of the gas venting event. The mass transport equation is as the following

$$\frac{dc}{dt} = -\frac{\partial}{\partial x}\left(-D\frac{\partial c}{\partial x} + cv\right) + r \tag{6.11}$$

where c is the concentration of CO_2. $D = 14.2\ mm^2/s$ is the diffusion coefficient of CO_2 in the air. $v(x,t)$ is the vent-gas velocity distribution as a function of location (x) and time (t), and follows the equation below

$$v(x,t) = \begin{cases} v_0, & \text{if } x > v_0(t - t_0)\ \&\ x < v_0 t \\ 0, & \text{otherwise.} \end{cases} \tag{6.12}$$

where v_0 is the initial vent velocity, and can be derived using the amount of gas and the duration of the gas venting

$$v_0 = \frac{n_{CO_2} R T_{gas}}{P A_{Rupture} t_0} = 0.12\ m/s \tag{6.13}$$

where $A_{Rupture}$ is assumed to be the area of the rupture, P the atmospheric pressure, R the gas constant, T_{gas} the average gas temperature, and t_0 the duration of the gas venting ($t_0 = 1.5\ s$ from simulation using model of [52]). The source term r for the CO_2 generation follows the equation below

$$r = \frac{n_{CO_2}}{A_{Rupture} h_{ch} t_0} \tag{6.14}$$

where h_{ch} is the vent-gas channel height. The initial concentration is set to 400 ppm. Furthermore there is a Dirichlet boundary condition at outlet, which corresponds to the atmosphere CO_2 concentration, $c(x_{outlet}, t) = 400$ ppm.

6.3 Limitation of Voltage Based Detection in Parallel Circuits

Voltage-based fault detection works well for a single cell and is one of the focus areas in Chapter 3. However, in parallel circuits, voltage-based detection suffers from signal suppression issues. Based on Eq. 6.2, for parallel-connected batteries, the change of terminal voltage after an ISC event can be written as

$$\Delta V_T = -\frac{R_{cell} \cdot V(SOC)}{R_{cell} + n \cdot R_{short}} \tag{6.15}$$

And it can be easily identified that, with the increase of parallel connected cells number n, ΔV_T will decrease.

$$n \uparrow \rightarrow \Delta V_T \downarrow$$

For the single-cell case, the voltage drop is significant after an internal short, and this voltage drop can be easily detected. For the battery module with 50 cells in parallel, after the ISC, the measured terminal voltage drop will be much smaller.

For internal short resistance of $30m\Omega$ and cell resistance of $5m\Omega$, the instantaneous voltage drop for a single cell is around 0.6 V, while the voltage drop for parallel-connected battery module is around 14 mV. With voltage noise standard deviation being set as $\sigma_V = 5\ mV$ [51], the voltage drop for the battery module is at a similar magnitude with voltage sensor noise. This voltage drop can easily be neglected in the voltage detection system.

With the number of cells increasing in the battery module, the changes of expansion force F_{gas} in an ISC event will also decrease. Similarly, a larger vent-gas channel will lead to a smaller gas concentration change measured by the gas sensor. Nevertheless, the decrease of signal-to-noise ratio for detection using expansion force and gas signals is less significant. Expansion force signal and gas signals still have high signal-to-noise ratios for the battery module with 50 cells connected in parallel, and these two detection methods can be extended to battery packs while maintaining a high signal-to-noise ratio.

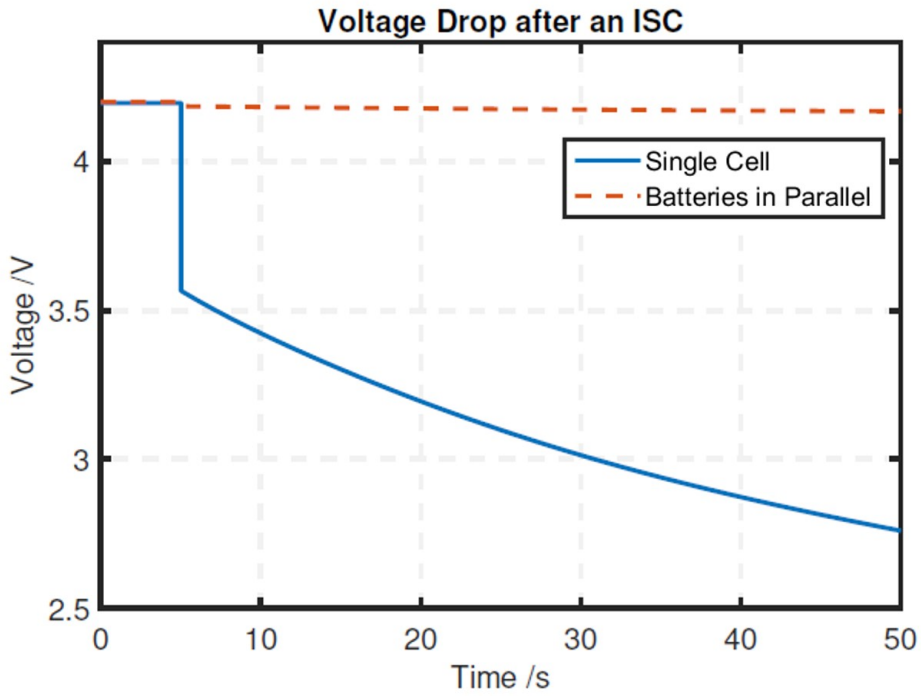

Figure 6.3: Terminal voltage drop after an ISC event for a single cell and batteries in parallel (50 cells in parallel), simulated with OCV-R-RC model [7].

6.4 Fault Detection Methodology

Considering the fast response of the expansion force signal and the gas concentrations signal, we propose an ISC detection methodology for the parallel-connected battery module based on expansion force measurements and gas sensing.

6.4.1 Fault Detection Algorithm Using Expansion Force

From the above discussions, an expansion force model is built during normal operating conditions. Similar to Chapter 3, based on the model, we build an observer for the expansion force

$$\hat{F} = f_1(T) + f_2(\hat{SOC}) + F_0 + \Theta_F \tag{6.16}$$

$$\Theta_F = \bar{F} - \hat{F} \tag{6.17}$$

where $\bar{F}$ is the measured force, and Θ_F is the estimated residual from force signal. Θ_F can be derived from force measurement and the estimated expansion force.

At normal operating conditions, the measurement for expansion force should match the model, and ideally Θ_F should be zero. However, Θ_F will not necessar-

ily be zero due to modeling error and sensor noise. In a short circuit case, after the expansion force surges in a few seconds, Θ_F will increase rapidly and can indicate a fault.

The adaptive threshold is used for fault detection, similar to Chapter 3.

$$R_k = \frac{1}{m}\sum_{i=1}^{m}\Theta_{F,k-i+1} \tag{6.18}$$

$$\sigma_{F,k}^2 = \frac{1}{m-1}\sum_{i=1}^{m}(\Theta_{F,k-i+1} - R_k)^2 \tag{6.19}$$

$$\epsilon_{F+} = R_k + 8\sigma_{F,k} \tag{6.20}$$

$$\epsilon_{F-} = R_k - 8\sigma_{F,k} \tag{6.21}$$

where m is the moving window size, which is set as 500 in this study. R_k is the average value of the estimated residual Θ_F in the moving window, and $\sigma_{F,k}^2$ is the variance between Θ_F and the moving window average value R_k. ϵ_{F+} and ϵ_{F-} are the upper and lower bound of the adaptive threshold.

6.4.2 Higher Confidence Level Detection with Gas Sensor

Here, for higher confidence level, we use expansion force measurement and gas concentration measurement for ISC detection. If only gas signal indicates a fault, then this might be a cell leakage event. If only force signal indicates a fault, then this leads to a overstress warning. If both signals indicate a fault then the cause is most likely an ISC event.

For the CO_2 gas concentration, we define the fault gas concentration value as

$$G_{fault} = \bar{G} - G_{normal} \tag{6.22}$$

where $\bar{G}$ is the measured CO_2 concentrations in ppm, and G_{normal} is the normal CO_2 gas concentrations in atmosphere, which is set as 400 ppm in this study.

If the fault gas concentration value G_{fault} exceeds the pre-defined value, ϵ_G, then the gas detection system will trigger an alarm. In the system with both force and gas sensors, only after receiving alarms from both detection systems in a short time frame, an ISC event is believed to have occurred.

Table 6.1: Detection logic with expansion force and gas

CO_2 Concentrations	Force	Decision
$G_{fault} > \epsilon_G$	$\Theta_F \notin [\epsilon_{F-}, \epsilon_{F+}]$	ISC Alert
$G_{fault} > \epsilon_G$	$\Theta_F \in [\epsilon_{F-}, \epsilon_{F+}]$	Cell Leakage Warning
$G_{fault} < \epsilon_G$	$\Theta_F \notin [\epsilon_{F-}, \epsilon_{F+}]$	Overstress Warning
$G_{fault} < \epsilon_G$	$\Theta_F \in [\epsilon_{F-}, \epsilon_{F+}]$	Normal

6.5 Simulation Result

For this study, we consider a battery module with 50 parallel connected 4.5 Ah NMC pouch cells. The model parameters are adopted from [52].

6.5.1 Simulation Settings

Zero mean white Gaussian noise ($N(0, \sigma^2)$) is added to the measurement to emulate a real system. The covariance of the noise for the voltage measurement is $\sigma_V = 5\ mV$. For the current measurement, $\sigma_I = 5\ mA$ [51]. For the temperature measurement, $\sigma_T = 0.5\ ^\circ C$ (Omega K-type thermal couple). For the force measurement, $\sigma_F = 8.9\ N$ (Omega). For the gas measurement, $\sigma_G = 30\ ppm$ (Amphenol).

The Urban Dynamometer Driving Schedule (UDDS) is used for the current profile. Before triggering the fault, the battery module operates under the UDDS cycle without a fault. Then, an internal short circuit is triggered at $t = 10\ s$, which shuts down the cell and disconnects the ISC current path 0.4 seconds later. The battery module continues to operate under the UDDS cycle after the fault.

In the following simulation, we will use the Coulomb Counting method to estimate SOC, which is purely based on the current measurement. For the detection threshold, considering the sensor measurement error, the gas detection threshold is set to $\epsilon_G = 2000\ ppm$. For the force detection adaptive threshold, for the first 50 seconds initialization period, $R_k = 0$, $\epsilon_{F,0} = 72\ N$, and the threshold will be updated with the moving window.

6.5.2 Simulation at Fault Conditions

In this simulation for the parallel-connected battery module, a hard internal short circuit is triggered in a cell. The cell triggers ISC at $t = 10\ s$ with a short circuit resistance $R_{short} = 25\ m\Omega$. The fast short circuit process is stopped after the ISC current path is burnt down [23]. The voltage quickly returns to normal and there

is no significant surface temperature increase for such an event. The cell swells and ruptures after 1.5 seconds of the ISC initialization. Although this fault will not directly lead to thermal runaway at this time, a second-time ISC might occur soon, so the event needs to be identified early to safely handle the battery module with the faulty cell.

The simulated hard short circuit event is shown in Fig. 6.4 for the current and voltage, and Fig. 6.5 for the force and gas concentrations profile. The first 10 seconds simulation is free of fault, and the short circuit fault triggers at $t = 10\ s$. Note that from Fig. 6.4, it is difficult to identify any abnormal voltage behavior for a battery module with cells connected in parallel.

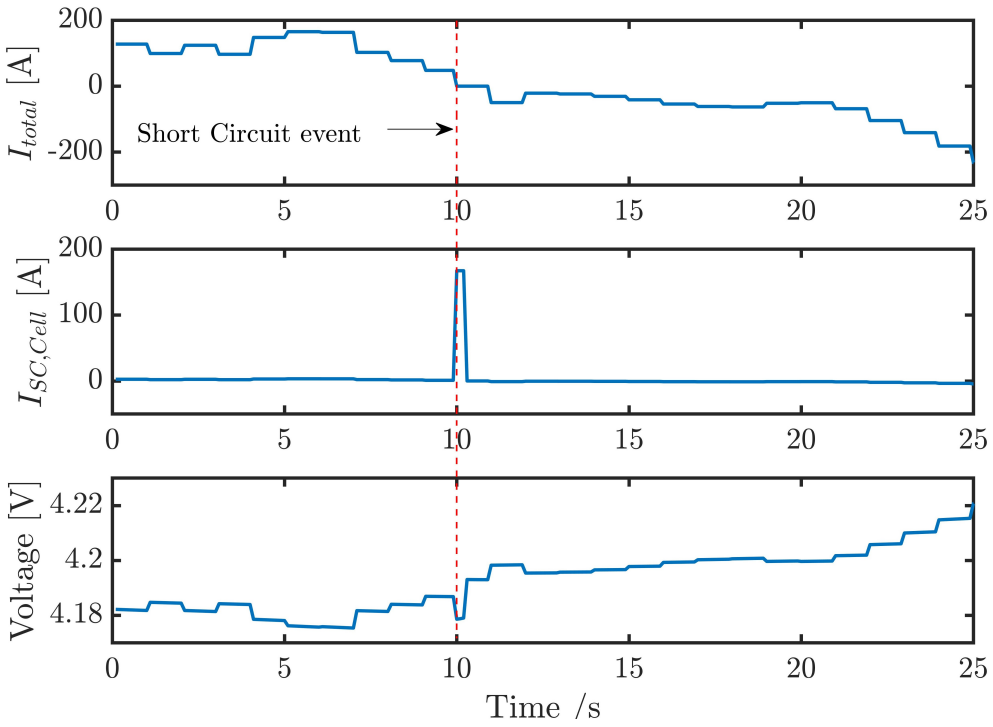

Figure 6.4: Total module current, short circuit cell current, and voltage profile under a fault condition, with a hard short circuit triggered at $t = 10s$. Note that no significant change for total module current and voltage is observed.

6.5.3 Fault Detection Using Existing Methods

Existing fault detection methods using temperature, current, voltage will be applied in the simulation, but they will face different issues for batteries connected in parallel.

(1) Detection based on current: For battery packs or parallel-connected battery modules, only the total pack or module current is measured and the individual

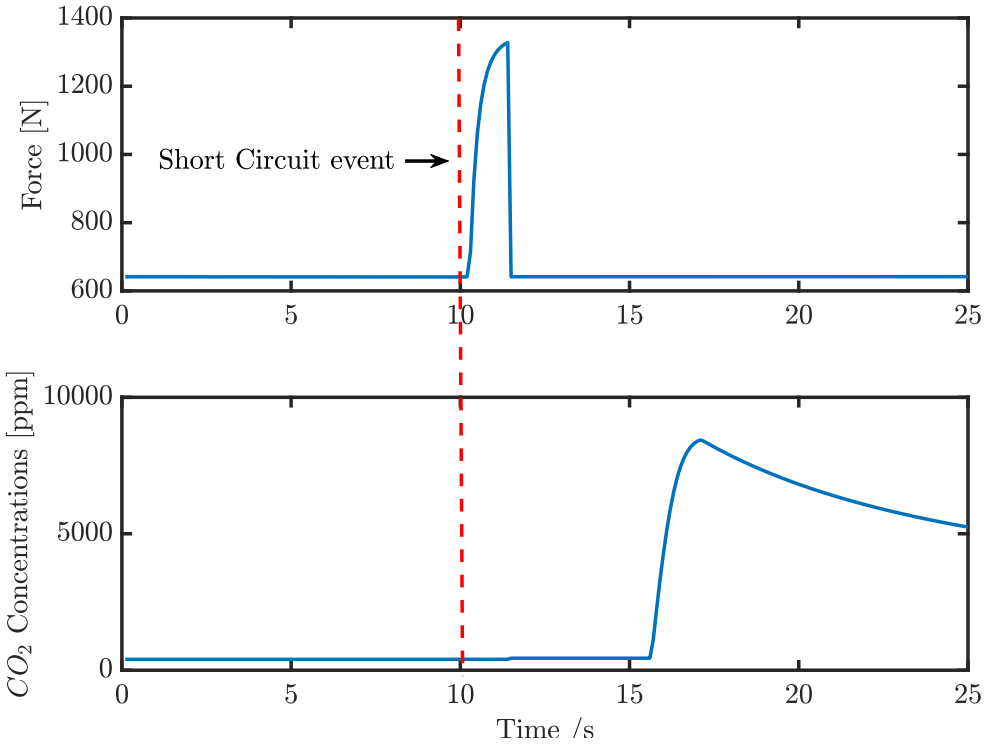

Figure 6.5: Expansion force and gas concentration at the module outlet after a short and cell rupture, with an internal short circuit triggered at $t = 10s$.

cell current is unknown. Although the ISC current is over 100 A for the faulty cell, this individual cell current information is not available. From the total module current in Fig. 6.4, detection cannot be made.

(2) Detection based on temperature: Only limited numbers of temperature sensors are instrumented in battery packs or modules. Therefore, the detection time can vary from minutes to hours based on the locations of the faulty cell and the temperature sensors. For ISC events that shut down a few seconds after the short circuit, the faulty cell surface temperature rise is also limited. In a prior ISC experiment, after 5 seconds of the ISC event, the measured surface temperature increased only 1 °C [52]. If temperature sensors are not close to the faulty cell, then detection cannot be made within seconds.

(3) Detection based on voltage: Voltage-based detection will suffer a low signal-to-noise ratio for batteries connected in parallel. As a comparison, the battery module's voltage profiles with ISC events and model estimated normal voltage (without ISC) are shown in Fig. 6.6. During the internal short event time, the voltage difference between the normal battery module and the battery module with ISC event is only 14 mV.

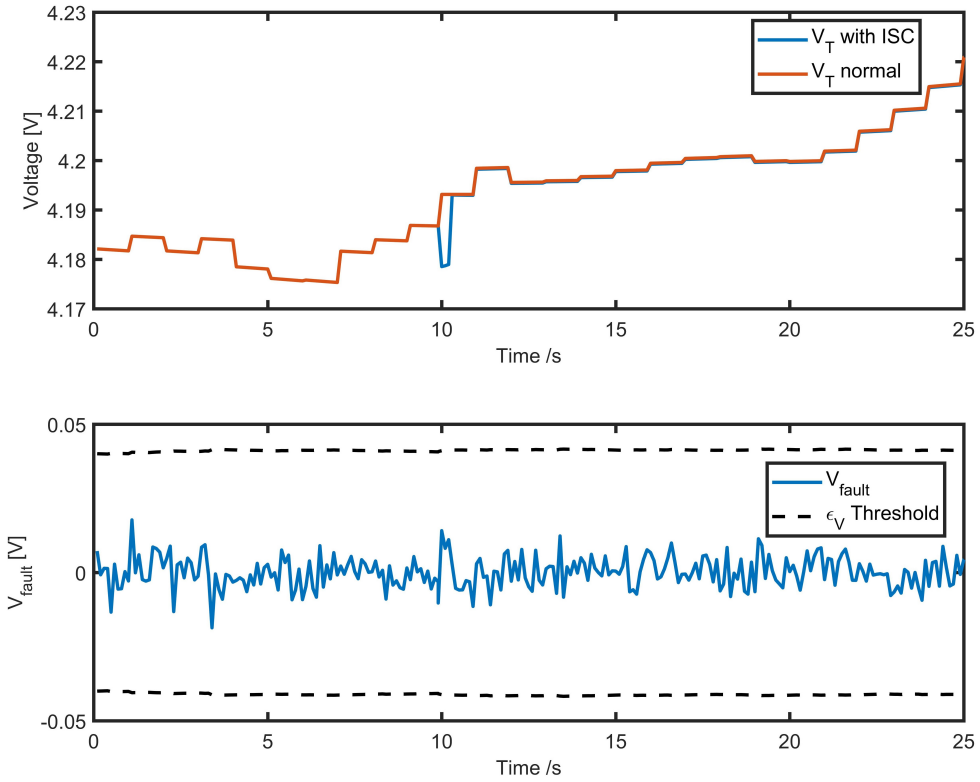

Figure 6.6: The terminal voltage of parallel-connected battery module with ISC event and normal voltage without ISC event, with only 14 mV difference during the ISC event. Voltage based method fails to detect an ISC event due to the low signal-to-noise ratio in parallel circuits.

Here, we apply the voltage detection method with adaptive thresholds in Chapter 3. We define the fault voltage as

$$V_{fault} = \hat{V} - \bar{V} \tag{6.23}$$

where $\bar{V}$ is the measured voltage, and $\hat{V}$ is the estimated battery module voltage at normal operating conditions.

Similar to Chapter 3, the adaptive threshold is used for fault voltage V_{fault}, and the upper and lower bound of the adaptive threshold can be set as

$$r_k = \frac{1}{m}\sum_{i=1}^{m} V_{fault,k-i+1} \tag{6.24}$$

$$\sigma^2_{V,k} = \frac{1}{m-1}\sum_{i=1}^{m}(V_{fault,k-i+1} - r_k)^2 \tag{6.25}$$

$$\epsilon_{V+} = r_k + 8\sigma_{V,k} \tag{6.26}$$

$$\epsilon_{V-} = r_k - 8\sigma_{V,k} \tag{6.27}$$

As seen in Fig. 6.6, after considering sensor measurement noise, the increased V_fault during the internal short cannot be identified with the measurement noise. V_{fault} does not cross the detection threshold and the voltage-based detection method fails to identify the ISC event in parallel circuits. Similarly, other detection methods by checking the voltage similarity between neighboring cells in series [50] or estimating battery internal resistance [14] cannot detect ISC for this parallel-connected battery module, simply because of the low signal-to-noise ratio of the voltage signal shown in Fig. 6.6.

6.5.4 Fault Detection Using Force and Gas

The main advantages of fault detection using expansion force and gas measurements are the high signal-to-noise ratio and fast response. While the existing detection methods using voltage, current, temperature measurements cannot identify the fault for the parallel-connected module, the proposed fault detection using force and gas measurements works well.

The estimated gas fault term G_{fault} and the estimated force fault term Θ_F after a short circuit triggered is shown in Fig. 6.7. At $t = 10.4\ s$, the force detection algorithm identifies the fault, and the gas sensor confirms the event at $t = 15.9\ s$. Even though the confirmation of an ISC event requires threshold crossing from both force and gas signals, it still achieves fast detection for a hard internal short event.

6.6 Summary

In this study, we propose a battery internal short circuit detection method based on battery expansion force measurement and gas sensing. The study primarily focuses on a specific type of ISC event that features a fast voltage drop and recovery, and no significant change in surface temperature.

For a parallel-connected module, this ISC event cannot be identified with the current-based method because of the lack of individual cell current information. Temperature-based methods suffer sparse information of the limited temperature sensors, and cannot make immediate detection. For the voltage-based detection method, due to the low signal-to-noise ratio in parallel circuits, voltage detection fails to identify the fault in the simulation.

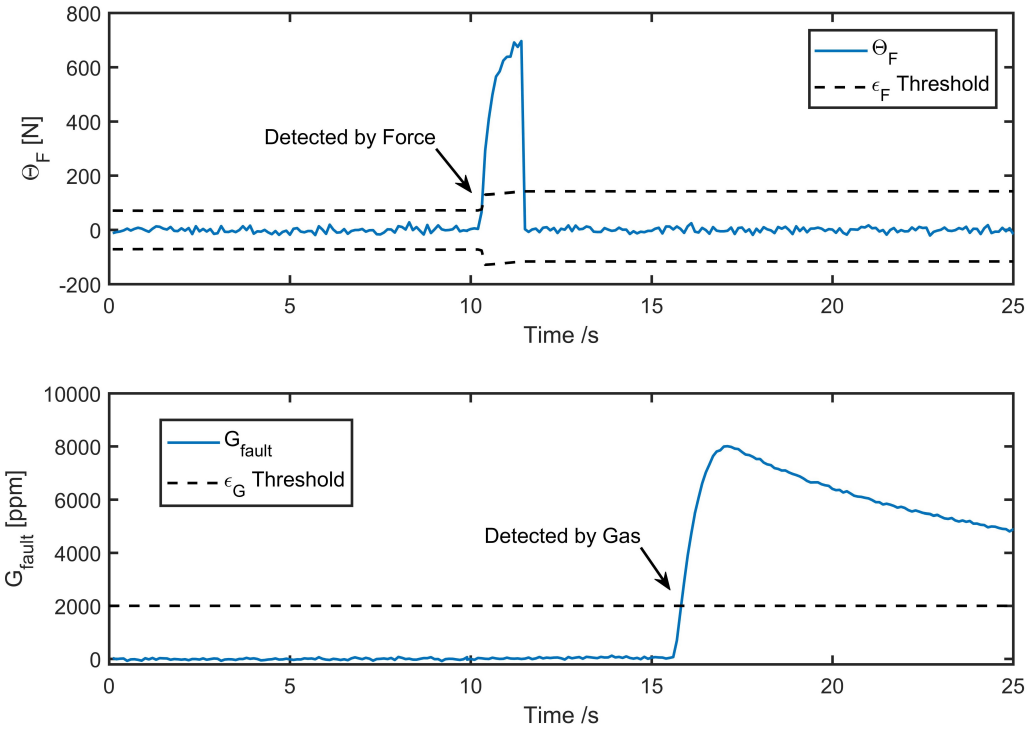

Figure 6.7: At fault conditions, force detection Θ_F identifies a fault at $t = 10.4s$, and gas detection G_{fault} confirms the fault at $t = 15.9s$.

For the proposed detection method using expansion force and gas measurements, a fast and high signal-to-noise ratio response can be achieved in a parallel-connected battery module. This methodology can also be extended to large battery packs used in electric vehicles. Further study is encouraged to validate the fault detection method for parallel circuits experimentally. After the fault being detected, how to safely handle the faulty battery module or battery pack and deactivate or de-energize the battery system will be the focus of future research on battery safety.

CHAPTER VII

Conclusions and Outlook

7.1 Conclusions

Reliable and immediate detection of battery failures and thermal runaway events is critical to electric vehicle safety, so that vehicle occupants can evacuate immediately, and first responders can take appropriate action to safely approach the battery and mitigate the damage. The existing methods of battery fault detection which rely on voltage, current, and temperature measurements either cannot detect faults or are too slow to detect faults in large-scale battery packs. This calls for a need to study battery failure and develop reliable and immediate detection methods.

The battery internal short circuit (ISC) can occur without explicit abuse conditions even when the electric vehicle is parked. ISC events are associated with a large heat release that can trigger thermal runway, which is considered the most dangerous type of battery safety event. In this dissertation, we presented a model which predicts the time to thermal runaway as a function of the ISC resistance. The model uses a spatial discretization with three regions to better model the large temperature difference between the shorted area and the bulk battery layers during an ISC event. The model explains the cell swelling caused by gas evolution in the early stage of ISC and predicts the outward force generated by the swelling when the cells are constrained. The experiments with instrumented cells showed that battery expansion occurs before the surface temperature rise and can serve as an early indication for ISC-induced thermal runaway events.

Next, an ISC detection method was developed and the methodology for setting the fault detection threshold was presented which achieves fast detection while minimizing the risk of false positives. ISC failures are dangerous and immediate detection is critical for the safety of electric vehicle battery packs. Additionally, for battery ISC detection, false positives are undesired, as many battery failure mitigation techniques

such as pyrotechnic fuses will disable the electric vehicle. Existing fault detection methods based on surface temperature measurement suffer poor observability due to the limited number of sensors placed in the pack [29]. To address these challenges, we developed a fault detection method that uses battery expansion force measurements to detect abnormal increases in force from ISC events. For a single cell case, a fault detection scheme was developed by using both expansion force and voltage measurements with adaptive thresholds to achieve high confidence fault detection.

Furthermore, the gas detection method was explored due to its fast response and easy implementation in a pack. From summarizing the past literature on vent-gas compositions under different testing conditions, CO_2 was proposed as the target gas species due to the high concentrations in all vent-gas, presence in first venting event, detectability for cell leakage, and good sensor feasibility with Non-Dispersive Infrared (NDIR) CO_2 sensors. The gas detection response in a battery pack was analyzed and the volume-averaged CO_2 concentration was estimated to help determine the gas detection threshold.

To better understand the battery out-gassing behavior and estimate the gas release amount, the CO_2 generation process, the cell venting process, and the gas flow upon a cell venting event were studied. A cell first venting model was introduced that enables the estimation of CO_2 released in a battery failure or thermal runaway event. The model was then used to analyze sensor placement and feasibility for managing cell thermal events in a battery storage depot. We simulated thermal runway and venting in a storage drum to compare the detection speed using gas sensors and temperature sensors. The results showed that in a storage drum, the gas-based detection method has a much faster response to battery thermal events compared to the temperature-based detection method.

Finally, we combined the methods of expansion force and gas sensing to detect hard ISC events in parallel-connected modules. For battery modules with cells connected in parallel, existing ISC detection methods using voltage, temperature, and current signals cannot achieve fast and high-confidence detection. For example, detecting a battery internal short based on voltage measurements will suffer from a low signal-to-noise ratio. Temperature and current-based methods are not feasible for battery modules as well due to poor observability with a sparse number of sensors or the high cost associated with providing each cell with a temperature and current sensor. In the simulation study, for a battery module with 50 cells connected in parallel, an ISC event was modeled with initial conditions and resistance that did not trigger thermal runaway. By measuring cell expansion force and monitoring CO_2

concentrations in the vent channel, fast and high confidence level fault detection was shown to be achievable for this parallel-connected battery module.

7.2 Practical Considerations and Outlook

The proposed fault detection method requires the use of expansion force sensors and gas sensors in battery packs. The cost and lifetime of force and gas sensors are important factors in the uptake of new technology. The automotive OEMs are sensitive to the cost of any added components, since the automotive industry features high volume and low-profit margin, with average net profit margins of around 7.5 % for major car companies [112]. To apply the proposed battery failure detection method in a real application, the expansion force sensor and gas sensor will be placed inside battery packs. The cost for replacing a failed sensor within a battery pack will be extremely expensive, mainly because of the labor cost to tear down the pack. Therefore, the force and gas sensors must be low in cost and have a long lifetime. For force sensors, the most common types of force sensors include strain gauges, piezoelectric sensors, and force-sensing resistors. Piezoelectric sensors and force-sensing resistors have disadvantages in precision and repeatability over time. For force measurement in EV battery pack, long-term reliable and steady measurement is needed. Therefore the compression load cells using strain gauges are preferred. The price of common strain gauge load cells ranges from $ 10 to $ 25, and strain gauge load cells usually have a cycle life over 10^6 [113], which is sufficient considering the batteries usually last around 3,000 cycles. For the gas sensor cost and lifetime, as discussed in Chapter 4, an NDIR CO_2 sensor's price ranges from $ 8 to $ 20 and can have a lifetime over 15 years. The price range and lifetime of force and gas sensors are considered applicable for use in EV battery packs.

There are also some engineering challenges for the expansion force sensors and CO_2 sensors. The NDIR CO_2 sensor is primarily used in HVAC applications, and to be used in an automotive battery pack, the sensor needs to pass automotive qualification testing, including vibration test, temperature endurance test, etc. For the expansion force signals, we used an adaptive threshold to account for the long-term sensor drift and cell degradation. However, calibration of expansion force sensor over time is still needed to ensure the accuracy of expansion force measurements, and to avoid sensor saturation issues due to irreversible expansion of the cell from cell aging [13].

The proposed battery failure detection method also has its weakness for certain battery failure events. The detection method mainly identifies cell swelling and release

of gas from battery failure. The method will have difficulty identifying the soft ISC event, which can occur without battery swelling and gas release. To identify the soft internal short process, methods using current and voltage measurement are preferred, which usually compare signals from cell to cell or from cell to model. The existing literature on battery short circuit detection using voltage, current, and temperature signals are discussed in the introduction Chapter 1.3 and in Chapter 3.1. Additionally, for battery external short circuit or overcharging, the proposed method can only detect the event after cell swelling and gas venting, while using voltage signals can identify the faults as soon as the voltage drops, which can be minutes earlier than the occurrence of cell swelling and gas venting.

One limitation of the proposed expansion force fault detection methodology is that it only applies to prismatic and pouch cells. This is due to the difficulty of measuring expansion force signals for other cell form factors, like cylindrical cells. For expansion force measurement, past studies have used strain gauges to measure the diameter changes of a cylindrical cell [114]. However, the measurement of expansion force in a battery pack composed of cylindrical cells is very difficult and would require instrumenting each individual cell. Therefore, at this stage, the fault detection method using expansion force only applies to packs with prismatic or pouch cells, where the cells can be stacked together and the expansion force can be measured in the pack. For the gas detection method, most commercial cells, including cylindrical cells, prismatic cells, and pouch cells, are equipped with a venting mechanism, where the pressure burst disk opens or the pouch ruptures when the cell internal pressure is high. In a cell failure event, the vent-gas will be ejected to the outside. The gas sensor can then detect the vent-gas regardless of the cell form factor.

The gas detection methodology can also be extended to stationary Li-ion battery energy storage facilities. Many battery energy storage systems are based on the second use of discarded EV battery packs, mainly due to cost-effectiveness and sustainability [115]. These second-use battery packs in energy storage systems are the same as EV battery packs. The fault detection method developed for EV battery packs then can be directly used in energy storage applications, especially if these packs are already equipped with gas sensors. In other cases, where larger battery packs are built specifically for energy storage applications, the efficacy of CO_2 gas detection system needs to be further evaluated. Due to more air space within these large energy storage battery packs, the vent-gas from a cell failure will be diluted and therefore it is more difficult to detect a cell failure event in large packs. Also, a larger air space in the pack can cause a potential delay in fault detection. The gas detection

time ties closely with the vent-gas flow, which depends on the gas diffusion process and convection process. If the gas sensor is not placed in proper locations, then the gas detection process might take minutes or hours. The vent-channel design and the location of gas sensors in battery packs will be interesting topics for future studies.

This dissertation addresses battery failure detection in different scenarios and the methodology can be used for large-scale EV battery packs. Further work to address the challenges in practical application of the fault detection method is highly encouraged. As for the future work direction, after the potential battery fault being detected, emergency responses are required to slow or prevent the thermal runaway propagation process and mitigate the hazards. Future work should consider the battery deactivation process and other active measures to prevent thermal runaway propagation in battery packs.

APPENDICES

APPENDIX A

University of Michigan Pouch Cell Specification

Table A.1: Pouch cell specification (manufactured at the University of Michigan Battery Lab)

Cell Specification	Value
Anode Thickness (Double Sided with Current Collector)	$125\mu m$
Cathode Thickness (Double Sided with Current Collector)	$135\mu m$
Current Collector Thickness Anode	$13\mu m$
Current Collector Thickness Cathode	$13\mu m$
Separator Material	PE
Separator Porosity	40%
Separator Thickness	$12\mu m$
Anode Active Material Mass Fraction (Graphite:PVDF)	95:5
Cathode Active Material Mass Fraction (NMC111:CB:PVDF)	94:3:3
Number of Double Sided Electrode Sheets Anode	15
Number of Double Sided Electrode Sheets Cathode	14
Electrolyte	1M $LiPF_6$
Organic Solvent in Electrolyte	2% EC:EMC (3:7)

Electrode mass loading (mg/cm^2) for total and active materials

Anode: 8.55 single / 17.1 double

Cathode: 16.5 single / 33 double

Number of double sided electrode sheets of each electrode in a pouch cell

Anode: 15

Cathode: 14

Electrode sheet size (cm)

Anode and cathode: 10.9 × 7.3

Mass of Anode (m_{an})

1. Electrode mass loading (mg/cm^2) for total and active materials: anode, 8.55 mg/cm^2 for single layer

2. Anode sheet size: 10.9 × 7.3 cm

3. Number of double sided electrode sheets of each electrode: anode 15, cathode 14 → 28 single layers of anode that contain active materials

m_{an}= 28 single layers × 8.55 mg/cm^2 anode mass per layer × (10.9 × 7.3) cm^2 anode sheet area = 19.1 g

Mass of Cathode (m_{ca})

1. Electrode mass loading (mg/cm^2) for total and active materials: cathode, 16.5 mg/cm^2 for single layer

2. Cathode sheet size: 10.9 × 7.3 cm

3. Number of double sided electrode sheets of each electrode: anode 15, cathode 14 → 28 single layers of cathode that contain active materials

m_{ca}= 28 single layers × 16.5 mg/cm^2 anode mass per layer × (10.9 × 7.3) cm^2 anode sheet area = 36.8 g

BIBLIOGRAPHY

BIBLIOGRAPHY

[1] Mckinsey & Company, "Lithium and cobalt: A tale of two commodities," https://www.mckinsey.com/industries/metals-and-mining/our-insights/lithium-and-cobalt-a-tale-of-two-commodities.

[2] Roskill, "Nickel sulphate: In high-nickel batteries, safety comes into question," https://roskill.com/news/nickel-sulphate-in-high-nickel-batteries-safety-comes-into-question/.

[3] R. Guo, L. Lu, M. Ouyang, and X. Feng, "Mechanism of the entire overdischarge process and overdischarge-induced internal short circuit in lithium-ion batteries," *Scientific reports*, vol. 6, p. 30248, 2016.

[4] E. Sahraei, J. Meier, and T. Wierzbicki, "Characterizing and modeling mechanical properties and onset of short circuit for three types of lithium-ion pouch cells," *Journal of Power Sources*, vol. 247, pp. 503–516, 2014.

[5] S. Huang, X. Du, M. Richter, J. Ford, G. M. Cavalheiro, Z. Du, R. T. White, and G. Zhang, "Understanding li-ion cell internal short circuit and thermal runaway through small, slow and in situ sensing nail penetration," *Journal of The Electrochemical Society*, vol. 167, no. 9, p. 090526, 2020.

[6] X. Feng, M. Ouyang, X. Liu, L. Lu, Y. Xia, and X. He, "Thermal runaway mechanism of lithium ion battery for electric vehicles: A review," *Energy Storage Materials*, vol. 10, pp. 246–267, 2018.

[7] T. Cai, S. Pannala, A. G. Stefanopoulou, and J. B. Siegel, "Battery internal short detection methodology using cell swelling measurements," in *2020 American Control Conference (ACC)*. IEEE, 2020, pp. 1143–1148.

[8] Mckinsey & Company, "Expanding electric-vehicle adoption despite early growing pains," https://www.mckinsey.com/industries/automotive-and-assembly/our-insights/expanding-electric-vehicle-adoption-despite-early-growing-pains.

[9] P. Sun, R. Bisschop, H. Niu, and X. Huang, "A review of battery fires in electric vehicles," *Fire technology*, pp. 1–50, 2020.

[10] D. Ren, X. Feng, L. Lu, M. Ouyang, S. Zheng, J. Li, and X. He, "An electrochemical-thermal coupled overcharge-to-thermal-runaway model for lithium ion battery," *Journal of power sources*, vol. 364, pp. 328–340, 2017.

[11] H. Maleki and J. N. Howard, "Effects of overdischarge on performance and thermal stability of a li-ion cell," *Journal of power sources*, vol. 160, no. 2, pp. 1395–1402, 2006.

[12] T. Hatchard, D. MacNeil, A. Basu, and J. Dahn, "Thermal model of cylindrical and prismatic lithium-ion cells," *Journal of The Electrochemical Society*, vol. 148, no. 7, p. A755, 2001.

[13] P. Mohtat, S. Lee, J. B. Siegel, and A. G. Stefanopoulou, "Towards better estimability of electrode-specific state of health: Decoding the cell expansion," *Journal of Power Sources*, vol. 427, pp. 101–111, 2019.

[14] X. Feng, Y. Pan, X. He, L. Wang, and M. Ouyang, "Detecting the internal short circuit in large-format lithium-ion battery using model-based fault-diagnosis algorithm," *Journal of Energy Storage*, vol. 18, pp. 26–39, 2018.

[15] M. N. Richard, "Accelerating rate calorimetry study on the thermal stability of lithium intercalated graphite in electrolyte. II. modeling the results and predicting differential scanning calorimeter curves," *Journal of The Electrochemical Society*, vol. 146, no. 6, p. 2078, 1999.

[16] G.-H. Kim, A. Pesaran, and R. Spotnitz, "A three-dimensional thermal abuse model for lithium-ion cells," *Journal of Power Sources*, vol. 170, no. 2, pp. 476–489, 2007.

[17] D. Ren, X. Liu, X. Feng, L. Lu, M. Ouyang, J. Li, and X. He, "Model-based thermal runaway prediction of lithium-ion batteries from kinetics analysis of cell components," *Applied Energy*, vol. 228, pp. 633–644, 2018.

[18] D. H. Doughty, "Vehicle battery safety roadmap guidance," National Renewable Energy Lab.(NREL), Golden, CO (United States), Tech. Rep., 2012.

[19] Global Registry (Global Technical Regulations), United Nations GTR No. 20 - Electric Vehicle Safety (EVS) (ECE/TRANS/180/Add.20), 2018, https://www.unece.org/fileadmin/DAM/trans/main/wp29/wp29wgs/wp29gen/wp29registry/ECE-TRANS-180a20e.pdf.

[20] M. Ouyang, M. Zhang, X. Feng, L. Lu, J. Li, X. He, and Y. Zheng, "Internal short circuit detection for battery pack using equivalent parameter and consistency method," *Journal of Power Sources*, vol. 294, pp. 272–283, 2015.

[21] S. Dey, H. E. Perez, and S. J. Moura, "Model-based battery thermal fault diagnostics: Algorithms, analysis, and experiments," *IEEE Transactions on Control Systems Technology*, vol. 27, no. 2, pp. 576–587, 2017.

[22] X. Feng, C. Weng, M. Ouyang, and J. Sun, "Online internal short circuit detection for a large format lithium ion battery," *Applied Energy*, vol. 161, pp. 168–180, 2016.

[23] M. Zhang, L. Liu, A. Stefanopoulou, J. Siegel, L. Lu, X. He, and M. Ouyang, "Fusing phenomenon of lithium-ion battery internal short circuit," *Journal of The Electrochemical Society*, vol. 164, no. 12, pp. A2738–A2745, 2017.

[24] P. T. Coman, S. Mátéfi-Tempfli, C. T. Veje, and R. E. White, "Modeling vaporization, gas generation and venting in li-ion battery cells with a dimethyl carbonate electrolyte," *Journal of The Electrochemical Society*, vol. 164, no. 9, pp. A1858–A1865, 2017.

[25] M. Zhang, J. Du, L. Liu, A. Stefanopoulou, J. Siegel, L. Lu, X. He, X. Xie, and M. Ouyang, "Internal short circuit trigger method for lithium-ion battery based on shape memory alloy," *Journal of The Electrochemical Society*, vol. 164, no. 13, pp. A3038–A3044, 2017.

[26] X. Feng, M. Fang, X. He, M. Ouyang, L. Lu, H. Wang, and M. Zhang, "Thermal runaway features of large format prismatic lithium ion battery using extended volume accelerating rate calorimetry," *Journal of Power Sources*, vol. 255, pp. 294–301, 2014.

[27] S. Koch, K. Birke, and R. Kuhn, "Fast thermal runaway detection for lithium-ion cells in large scale traction batteries," *Batteries*, vol. 4, no. 2, p. 16, 2018.

[28] Z. Song, F. P. Delgado, J. Hou, H. Hofmann, and J. Sun, "Individual cell fault detection for parallel-connected battery cells based on the statistical model and analysis," *arXiv preprint arXiv:2004.12412*, 2020.

[29] X. Lin, H. Fu, H. E. Perez, J. B. Siege, A. G. Stefanopoulou, Y. Ding, and M. P. Castanier, "Parameterization and observability analysis of scalable battery clusters for onboard thermal management," *Oil & Gas Science and Technology–Revue d'IFP Energies nouvelles*, vol. 68, no. 1, pp. 165–178, 2013.

[30] M. Zhang, J. Du, L. Liu, J. Siegel, L. Lu, X. He, and M. Ouyang, "Internal short circuit detection method for battery pack based on circuit topology," *Science China Technological Sciences*, vol. 61, no. 10, pp. 1502–1511, 2018.

[31] X. Feng, X. He, M. Ouyang, L. Wang, L. Lu, D. Ren, and S. Santhanagopalan, "A coupled electrochemical-thermal failure model for predicting the thermal runaway behavior of lithium-ion batteries," *Journal of The Electrochemical Society*, vol. 165, no. 16, p. A3748, 2018.

[32] P. T. Coman, E. C. Darcy, C. T. Veje, and R. E. White, "Modelling li-ion cell thermal runaway triggered by an internal short circuit device using an efficiency factor and arrhenius formulations," *Journal of The Electrochemical Society*, vol. 164, no. 4, pp. A587–A593, 2017.

[33] C. Zhang, S. Santhanagopalan, M. A. Sprague, and A. A. Pesaran, "Coupled mechanical-electrical-thermal modeling for short-circuit prediction in a lithium-ion cell under mechanical abuse," *Journal of Power Sources*, vol. 290, pp. 102–113, 2015.

[34] G.-H. Kim, K. Smith, J. Ireland, and A. Pesaran, "Fail-safe design for large capacity lithium-ion battery systems," *Journal of Power Sources*, vol. 210, pp. 243–253, 2012.

[35] T. Cai, A. G. Stefanopoulou, and J. B. Siegel, "Modeling li-ion battery thermal runaway using a three section thermal model," in *ASME 2018 Dynamic Systems and Control Conference*. American Society of Mechanical Engineers Digital Collection, 2018.

[36] P. T. Coman, S. Rayman, and R. E. White, "A lumped model of venting during thermal runaway in a cylindrical lithium cobalt oxide lithium-ion cell," *Journal of Power Sources*, vol. 307, pp. 56–62, 2016.

[37] M. Lammer, A. Königseder, and V. Hacker, "Holistic methodology for characterisation of the thermally induced failure of commercially available 18650 lithium ion cells," *RSC Advances*, vol. 7, no. 39, pp. 24 425–24 429, 2017.

[38] D. P. Finegan, E. Darcy, M. Keyser, B. Tjaden, T. M. Heenan, R. Jervis, J. J. Bailey, R. Malik, N. T. Vo, O. V. Magdysyuk *et al.*, "Characterising thermal runaway within lithium-ion cells by inducing and monitoring internal short circuits," *Energy & Environmental Science*, vol. 10, no. 6, pp. 1377–1388, 2017.

[39] A. Rheinfeld, A. Noel, J. Wilhelm, A. Kriston, A. Pfrang, and A. Jossen, "Quasi-isothermal external short circuit tests applied to lithium-ion cells: Part i. measurements," *Journal of The Electrochemical Society*, vol. 165, no. 14, pp. A3427–A3448, 2018.

[40] S. Yang, B. Yan, J. Wu, L. Lu, and K. Zeng, "Temperature-dependent lithium-ion diffusion and activation energy of li1. 2co0. 13ni0. 13mn0. 54o2 thin-film cathode at nanoscale by using electrochemical strain microscopy," *ACS applied materials & interfaces*, vol. 9, no. 16, pp. 13 999–14 005, 2017.

[41] X. Lin, H. E. Perez, J. B. Siegel, A. G. Stefanopoulou, Y. Li, R. D. Anderson, Y. Ding, and M. P. Castanier, "Online parameterization of lumped thermal dynamics in cylindrical lithium ion batteries for core temperature estimation and health monitoring," *IEEE Transactions on Control Systems Technology*, vol. 21, no. 5, pp. 1745–1755, 2013.

[42] T. Dong, P. Peng, and F. Jiang, "Numerical modeling and analysis of the thermal behavior of ncm lithium-ion batteries subjected to very high c-rate discharge/charge operations," *International Journal of Heat and Mass Transfer*, vol. 117, pp. 261–272, 2018.

[43] R. Spotnitz and J. Franklin, "Abuse behavior of high-power, lithium-ion cells," *Journal of Power Sources*, vol. 113, no. 1, pp. 81–100, 2003.

[44] P. Ping, Q. Wang, P. Huang, J. Sun, and C. Chen, "Thermal behaviour analysis of lithium-ion battery at elevated temperature using deconvolution method," *Applied Energy*, vol. 129, pp. 261–273, 2014.

[45] H. Yang, H. Bang, K. Amine, and J. Prakash, "Investigations of the exothermic reactions of natural graphite anode for li-ion batteries during thermal runaway," *Journal of the Electrochemical Society*, vol. 152, no. 1, pp. A73–A79, 2005.

[46] A. Knobloch, C. Kapusta, J. Karp, Y. Plotnikov, J. Siegel, and A. Stefanopoulou, "Fabrication of multi-measurand sensor for monitoring of a li-ion battery," *Journal of Electronic Packaging*, 2018.

[47] S. Pannala, M. Zhang, J. Siegel, G. Less, and A. Stefanopoulou, "Mechanical measurements for early detection of thermal runaway induced by an internal short circuit," in *ECS Meeting Abstracts*, vol. MA2018-01 (3) 2151-2041, 2018, pp. 368–368.

[48] C.-S. Kim, J.-S. Yoo, K.-M. Jeong, K. Kim, and C.-W. Yi, "Investigation on internal short circuits of lithium polymer batteries with a ceramic-coated separator during nail penetration," *Journal of Power Sources*, vol. 289, pp. 41–49, 2015.

[49] B. Xia and C. Mi, "A fault-tolerant voltage measurement method for series connected battery packs," *Journal of Power Sources*, vol. 308, pp. 83–96, 2016.

[50] B. Xia, Y. Shang, T. Nguyen, and C. Mi, "A correlation based fault detection method for short circuits in battery packs," *Journal of Power Sources*, vol. 337, pp. 1–10, 2017.

[51] S. Dey, Y. Shi, K. Smith, and M. Khanra, "Safer batteries via active fault tolerant control," in *2019 American Control Conference (ACC)*. IEEE, 2019, pp. 1561–1566.

[52] T. Cai, A. G. Stefanopoulou, and J. B. Siegel, "Modeling li-ion battery temperature and expansion force during the early stages of thermal runaway triggered by internal shorts," *Journal of The Electrochemical Society*, vol. 166, no. 12, pp. A2431–A2443, 2019.

[53] K. Kumai, H. Miyashiro, Y. Kobayashi, K. Takei, and R. Ishikawa, "Gas generation mechanism due to electrolyte decomposition in commercial lithium-ion cell," *Journal of power sources*, vol. 81, pp. 715–719, 1999.

[54] T. Polóni, M. A. Figueroa-Santos, J. B. Siegel, and A. G. Stefanopoulou, "Integration of non-monotonic cell swelling characteristic for state-of-charge estimation," in *2018 Annual American Control Conference (ACC)*. IEEE, 2018, pp. 2306–2311.

[55] S. Mohan, Y. Kim, J. B. Siegel, N. A. Samad, and A. G. Stefanopoulou, "A phenomenological model of bulk force in a li-ion battery pack and its application to state of charge estimation," *Journal of the Electrochemical Society*, vol. 161, no. 14, pp. A2222–A2231, 2014.

[56] G. L. Plett, "Extended kalman filtering for battery management systems of lipb-based hev battery packs: Part 2. modeling and identification," *Journal of power sources*, vol. 134, no. 2, pp. 262–276, 2004.

[57] X. Hu, K. Zhang, K. Liu, X. Lin, S. Dey, and S. Onori, "Advanced fault diagnosis for lithium-ion battery systems: A review of fault mechanisms, fault features, and diagnosis procedures," *IEEE Industrial Electronics Magazine*, vol. 14, no. 3, pp. 65–91, 2020.

[58] X. Li and Z. Wang, "A novel fault diagnosis method for lithium-ion battery packs of electric vehicles," *Measurement*, vol. 116, pp. 402–411, 2018.

[59] Z. Shi, F. Gu, B. Lennox, and A. Ball, "The development of an adaptive threshold for model-based fault detection of a nonlinear electro-hydraulic system," *Control Engineering Practice*, vol. 13, no. 11, pp. 1357–1367, 2005.

[60] T. Cai, A. G. Stefanopoulou, and J. B. Siegel, "Early detection for li-ion batteries thermal runaway based on gas sensing," *ECS Transactions*, vol. 89, no. 1, pp. 85–97, 2019.

[61] C. Lee, A. O. Said, and S. I. Stoliarov, "Impact of state of charge and cell arrangement on thermal runaway propagation in lithium ion battery cell arrays," *Transportation research record*, vol. 2673, no. 8, pp. 408–417, 2019.

[62] F. Larsson, P. Andersson, P. Blomqvist, and B.-E. Mellander, "Toxic fluoride gas emissions from lithium-ion battery fires," *Scientific reports*, vol. 7, no. 1, pp. 1–13, 2017.

[63] A. W. Golubkov, S. Scheikl, R. Planteu, G. Voitic, H. Wiltsche, C. Stangl, G. Fauler, A. Thaler, and V. Hacker, "Thermal runaway of commercial 18650 li-ion batteries with lfp and nca cathodes–impact of state of charge and overcharge," *Rsc Advances*, vol. 5, no. 70, pp. 57 171–57 186, 2015.

[64] A. W. Golubkov, D. Fuchs, J. Wagner, H. Wiltsche, C. Stangl, G. Fauler, G. Voitic, A. Thaler, and V. Hacker, "Thermal-runaway experiments on consumer li-ion batteries with metal-oxide and olivin-type cathodes," *Rsc Advances*, vol. 4, no. 7, pp. 3633–3642, 2014.

[65] A. O. Said, C. Lee, S. I. Stoliarov, and A. W. Marshall, "Comprehensive analysis of dynamics and hazards associated with cascading failure in 18650 lithium ion cell arrays," *Applied Energy*, vol. 248, pp. 415–428, 2019.

[66] A. O. Said, C. Lee, and S. I. Stoliarov, "Experimental investigation of cascading failure in 18650 lithium ion cell arrays: Impact of cathode chemistry," *Journal of Power Sources*, vol. 446, p. 227347, 2020.

[67] P. Ribière, S. Grugeon, M. Morcrette, S. Boyanov, S. Laruelle, and G. Marlair, "Investigation on the fire-induced hazards of li-ion battery cells by fire

calorimetry," *Energy & Environmental Science*, vol. 5, no. 1, pp. 5271–5280, 2012.

[68] C. Lee, A. O. Said, and S. I. Stoliarov, "Passive mitigation of thermal runaway propagation in dense 18650 lithium ion cell assemblies," *Journal of The Electrochemical Society*, vol. 167, no. 9, p. 090524, 2020.

[69] A. O. M. Said, "Dynamics and hazards of cascading failure in lithium ion cell arrays: Analysis, passive mitigation, and active suppression," Ph.D. dissertation, University of Maryland, 2020.

[70] D. Sturk, L. Rosell, P. Blomqvist, and A. Ahlberg Tidblad, "Analysis of li-ion battery gases vented in an inert atmosphere thermal test chamber," *Batteries*, vol. 5, no. 3, p. 61, 2019.

[71] T. Yamanaka, Y. Takagishi, Y. Tozuka, and T. Yamaue, "Modeling lithium ion battery nail penetration tests and quantitative evaluation of the degree of combustion risk," *Journal of Power Sources*, vol. 416, pp. 132–140, 2019.

[72] A. Nedjalkov, J. Meyer, M. Köhring, A. Doering, M. Angelmahr, S. Dahle, A. Sander, A. Fischer, and W. Schade, "Toxic gas emissions from damaged lithium ion batteries—analysis and safety enhancement solution," *Batteries*, vol. 2, no. 1, p. 5, 2016.

[73] Y. Fernandes, A. Bry, and S. de Persis, "Identification and quantification of gases emitted during abuse tests by overcharge of a commercial li-ion battery," *Journal of Power Sources*, vol. 389, pp. 106–119, 2018.

[74] Q. Yuan, F. Zhao, W. Wang, Y. Zhao, Z. Liang, and D. Yan, "Overcharge failure investigation of lithium-ion batteries," *Electrochimica Acta*, vol. 178, pp. 682–688, 2015.

[75] Y. Zhang, H. Wang, W. Li, and C. Li, "Quantitative identification of emissions from abused prismatic ni-rich lithium-ion batteries," *eTransportation*, vol. 2, p. 100031, 2019.

[76] S. Koch, A. Fill, and K. P. Birke, "Comprehensive gas analysis on large scale automotive lithium-ion cells in thermal runaway," *Journal of Power Sources*, vol. 398, pp. 106–112, 2018.

[77] F. Larsson and B.-E. Mellander, "Abuse by external heating, overcharge and short circuiting of commercial lithium-ion battery cells," *Journal of The Electrochemical Society*, vol. 161, no. 10, p. A1611, 2014.

[78] Z. Chen, R. Xiong, J. Lu, and X. Li, "Temperature rise prediction of lithium-ion battery suffering external short circuit for all-climate electric vehicles application," *Applied energy*, vol. 213, pp. 375–383, 2018.

[79] R. Xiong, R. Yang, Z. Chen, W. Shen, and F. Sun, "Online fault diagnosis of external short circuit for lithium-ion battery pack," *IEEE Transactions on Industrial Electronics*, vol. 67, no. 2, pp. 1081–1091, 2019.

[80] C. Xu, M. Ouyang, L. Lu, X. Liu, S. Wang, and X. Feng, "Preliminary study on the mechanism of lithium ion battery pack under water immersion," *ECS Transactions*, vol. 77, no. 11, p. 209, 2017.

[81] V. Somandepalli, K. Marr, and Q. Horn, "Quantification of combustion hazards of thermal runaway failures in lithium-ion batteries," *SAE International Journal of Alternative Powertrains*, vol. 3, no. 1, pp. 98–104, 2014.

[82] L. Spinelle, M. Gerboles, G. Kok, S. Persijn, and T. Sauerwald, "Review of portable and low-cost sensors for the ambient air monitoring of benzene and other volatile organic compounds," *Sensors*, vol. 17, no. 7, p. 1520, 2017.

[83] SGXsensortech, "Design of electronics for electrochemical gas sensors," https://www.sgxsensortech.com/content/uploads/2014/08/A1A-EC_SENSORS_AN2-Design-of-Electronics-for-EC-Sensors-V4.pdf.

[84] Z. Liao, S. Zhang, K. Li, G. Zhang, and T. G. Habetler, "A survey of methods for monitoring and detecting thermal runaway of lithium-ion batteries," *Journal of Power Sources*, vol. 436, p. 226879, 2019.

[85] J. Watson, K. Ihokura, and G. S. Coles, "The tin dioxide gas sensor," *Measurement Science and Technology*, vol. 4, no. 7, p. 711, 1993.

[86] DigiKey, "Sensirion ag sgp40-d-r4 sensor," https://www.digikey.com/en/products/detail/sensirion-ag/SGP40-D-R4/12820418.

[87] ——, "Amphenol sgx sensortech mics-vz-89te," https://www.digikey.com/en/products/detail/amphenol-sgx-sensortech/MICS-VZ-89TE/7102285.

[88] R. Hasanaj and A. Abuhemidan, "Air-quality sensor with 10-years lifespan," 2019.

[89] R. Zhou, S. Vaihinger, K. Geckeler, and W. Göpel, "Reliable co2 sensors with silicon-based polymers on quartz microbalance transducers," *Sensors and Actuators B: Chemical*, vol. 19, no. 1-3, pp. 415–420, 1994.

[90] D. Gibson and C. MacGregor, "A novel solid state non-dispersive infrared co2 gas sensor compatible with wireless and portable deployment," *Sensors*, vol. 13, no. 6, pp. 7079–7103, 2013.

[91] S. S. Shrestha, "Performance evaluation of carbon-dioxide sensors used in building hvac applications," Ph.D. dissertation, Iowa State University, 2009.

[92] Amphenol, "Amphenol advanced sensors telaire t6700 series," https://www.amphenol-sensors.com/en/telaire/co2/525-co2-sensor-modules/3215-t6700.

[93] D. B. Henderson, D. J. Gongloff, and A. I. Kouznetsov, "Optical gas sensor," Jun. 21 2016, uS Patent App. 29/472,322.

[94] N. A. Samad, B. Wang, J. B. Siegel, and A. G. Stefanopoulou, "Parameterization of battery electrothermal models coupled with finite element flow models for cooling," *Journal of Dynamic Systems, Measurement, and Control*, vol. 139, no. 7, 2017.

[95] H. Chen, J. E. Buston, J. Gill, D. Howard, R. C. Williams, C. M. R. Vendra, A. Shelke, and J. X. Wen, "An experimental study on thermal runaway characteristics of lithium-ion batteries with high specific energy and prediction of heat release rate," *Journal of Power Sources*, vol. 472, p. 228585, 2020.

[96] D. Juarez-Robles, A. Vyas, C. Fear, J. Jeevarajan, and P. P. Mukherjee, "Overcharge and aging analytics of li-ion cells," *Journal of the Electrochemical Society*, 2020.

[97] J. D. Kelly, "High voltage hybrid systems - 2013-2016 ford fusion hybrid li-ion battery," 28 October 2017, https://www.youtube.com/watch?v=kmDpNr1PdMk.

[98] ——, "2017 prius prime - 8.79kwh battery deep dive," 9 July 2018, https://www.youtube.com/watch?v=yGMcQ6JWlBs.

[99] T. Higashino, K. Saito, and T. Motohashi, "Battery pack with covering member and vehicle with the battery pack," Feb. 4 2014, US Patent 8,642,204.

[100] T. E. World, "Fiat 500e - teardown - episode 7 - battery pack," 26 December 2019, https://www.youtube.com/watch?v=ROu8T_ehdLA&t=935s.

[101] E. S. E. Vehicle and T. Forums, "Fiat 500e battery modules," 29 February 2016, https://endless-sphere.com/forums/viewtopic.php?t=78553.

[102] D. C. Inc, "Protecting battery enclosures with dual-stage venting," October 2019, https://www.donaldson.com/en-us/venting/technical-articles/protecting-battery-enclosures-dual-stage-venting/.

[103] V. Mateev, I. Marinova, and Z. Kartunov, "Gas leakage source detection for li-ion batteries by distributed sensor array," *Sensors*, vol. 19, no. 13, p. 2900, 2019.

[104] R. Srinivasan, M. Thomas, M. Airola, B. Carkhuff, L. Frizzell-Makowski, H. Alkandry, J. Reuster, H. Oguz, P. Green, J. La Favors *et al.*, "Preventing cell-to-cell propagation of thermal runaway in lithium-ion batteries," *Journal of The Electrochemical Society*, vol. 167, no. 2, p. 020559, 2020.

[105] "Two-stage venting provides protection, available online at," https://www.designnews.com/content/two-stage-venting-provides-protection/76842761358820.

[106] S. Arora, W. Shen, and A. Kapoor, "Review of mechanical design and strategic placement technique of a robust battery pack for electric vehicles," *Renewable and Sustainable Energy Reviews*, vol. 60, pp. 1319–1331, 2016.

[107] D. B. Kittelson, W. J. Watts, and J. P. Johnson, "Fine particle (nanoparticle) emissions on minnesota highways," Minnesota Department of Transportation, Tech. Rep., 2001.

[108] G.-H. Kim, A. A. Pesaran, and K. Smith, *Thermal abuse modeling of Li-ion cells and propagation in modules*. National Renewable Energy Laboratory, 2008.

[109] Y.-J. Fang and J.-M. Qian, "Isobaric vapor- liquid equilibria of binary mixtures containing the carbonate group- ocoo-," *Journal of Chemical & Engineering Data*, vol. 50, no. 2, pp. 340–343, 2005.

[110] W. Ai, L. Kraft, J. Sturm, A. Jossen, and B. Wu, "Electrochemical thermal-mechanical modelling of stress inhomogeneity in lithium-ion pouch cells," *Journal of The Electrochemical Society*, vol. 167, no. 1, p. 013512, 2019.

[111] T. Cai, P. Valecha, V. Tran, B. Engle, A. Stefanopoulou, and J. Siegel, "Detection of li-ion battery failure and venting with carbon dioxide sensors," *eTransportation*, p. 100100, 2020.

[112] Statista, "Major car companies' five-year average net profit margin as of june 30, 2020," https://www.statista.com/statistics/1186661/car-company-profit-margin/.

[113] Digikey, "Te connectivity measurement specialties fx292x-040a-0200-l," https://www.digikey.com/en/products/detail/te-connectivity-measurement-specialties/FX292X-040A-0200-L/13692560.

[114] L. K. Willenberg, P. Dechent, G. Fuchs, D. U. Sauer, and E. Figgemeier, "High-precision monitoring of volume change of commercial lithium-ion batteries by using strain gauges," *Sustainability*, vol. 12, no. 2, p. 557, 2020.

[115] B. Faessler, "Stationary, second use battery energy storage systems and their applications: A research review," *Energies*, vol. 14, no. 8, p. 2335, 2021.